

ABSTRACT

SCHOCH, PHILLIP KETCHAM. Studying the Role of Surface Topography in Marine Anti-Fouling Coatings. (Under the direction of Dr. Jan Genzer)

This Ph.D. Thesis focuses on understanding the effects of topography in surface coatings to reduce or inhibit marine biofouling. We benefited from prior work in the Genzer group that revealed the robustness of hierarchical periodic surface topographies at reducing marine fouling. We aimed to break these hierarchical structures down into individual periodicities to attain fundamental understanding of their interplay with fouling organisms. To accomplish this, we utilize both computer simulations and experiments. We employ computer simulation to build our theoretical understanding of the interplay between size and shape of periodic surface features with fouling particles of spherical shape. We first developed a model for single particle adhesion, in which we demonstrated that the feature width (λ) had a large effect on the adhesion energy and position of the adsorbing particle. The minimum adsorption regime was $\lambda/D \sim 0.5$ where D is the diameter of the adsorbing particle. We expanded this model to examine multiple particles adsorbing on the same substrate to discover substrates with minimum number of adsorbing particles and minimum total adhesion. The minimum adhesion energy was found again at $\lambda/D \sim 0.5$; furthermore, this was also the region of fewest adsorbed particles. In the next stage of simulations, we further expanded the model to examine settlement of spherical particles with predefined size-polydispersity and studied their settlement on flat and periodically-corrugated substrates. We used normal distributions of varying standard deviation to generate assemblies of polydisperse particles. We found $\lambda/D_{\text{mean}} \sim 0.5$ as the minimum adhesion condition for the periodic substrates, where D_{mean} is the average value of the normal distribution. Additionally, at $\lambda/D_{\text{mean}} \sim 0.5$ these surfaces managed to reduce adhesion energy by $> 10\%$

when compared to flat substrates even at large polydispersity ($D_{\text{mean}} = 20$ $\text{STD} = 8$). In experiments we utilized photolithography of negative photoresists to build periodic surface structures of varying feature width (10 – 200 μm) and feature height (10 – 400 μm). We combined soft lithography and hot embossing to create the dozens of surfaces needed to test our surfaces against the barnacle species *Balanus Amphitrite* in their cyprid form. Settlement testing, by collaborators in the UK, revealed dramatic effects of surface topography on these barnacle cyprids. At 200 μm , feature width, our surface prevented any cyprids from attaching. Beyond this we developed low-fouling/foul-release chemical coatings based on polymer network gels, which allowed only ~15% of barnacle cyprids to settle and released ~45% of adsorbed juvenile barnacles. Finally, we developed a spraycoating method to conformally coat our microstructures with these low-fouling/foul-release polymers to improve our microtextures further. The contribution of this body of work contributes significantly in furthering our understanding on the role of surface topographies to reduce marine fouling.

© Copyright 2015 by Phillip Ketcham Schoch

All Rights Reserved

Studying the Role of Surface Topography in Marine Anti-Fouling Coatings

by
Phillip K. Schoch

A dissertation submitted to the Graduate Faculty of
North Carolina State University
in partial fulfillment of the
requirements for the degree of
Doctor of Philosophy

Chemical Engineering

Raleigh, North Carolina

2015

APPROVED BY:

Dr. Jan Genzer
Committee Chair

Dr. Michael Dickey

Dr. Kirill Efimenko

Dr. Orlando Rojas

DEDICATION

This dissertation is dedicated to my family. To my dad, Jonathan Schoch, for teaching me to be inquisitive in life and to set big goals. To my mom, Debra Schoch, for showing me how to persevere and laugh through all life has to offer. To my brother, Andrew Schoch, you have been such an amazing role model throughout my life and inspired me to pursue a PhD in the first place. To my brother, Robert Schoch, you have always been there when I needed you and you were the best brother to grow up with. Finally, to my soon-to-be wife, Kelly, you have shown me the true meaning of kindness and love. I look forward to every day I get to spend with you.

BIOGRAPHY

Phillip Schoch was born in Rochester, New York to his parents Jonathan and Debra Schoch. He has two older brothers, Andrew and Robert Schoch. Phillip was raised in Webster, New York and lived there all the way through graduating high school from R.L. Thomas High School, class of 2005. Upon graduation, Phillip decided to attend Purdue University in West Lafayette, Indiana to pursue an engineering degree. He chose to follow in Jonathan and Andrew's footsteps by pursuing a Bachelor's of Science in Chemical Engineering. During his undergraduate years, he worked internships at Chevron Phillips and Armstrong World Industries as well as worked as an undergraduate researcher for Dr. Stephen Beaudoin. After completion of his degree, Phillip chose to attend North Carolina State University in Raleigh, NC and study for his Ph.D. in Chemical Engineering under Dr. Jan Genzer. After completion of his graduate studies in May of 2015, Phillip will join ExxonMobil in Clinton, New Jersey to work as a Research Associate on novel process scale-up.

ACKNOWLEDGMENTS

Dr. Jan Genzer, what can I say that would even come close to expressing how much I have enjoyed working with you, how much I admire you and how thankful I have been to study under your tutelage? You have been the best advisor a Ph.D. student could ask for. I have learned so much in my time here and that is in large part your doing. I want to specifically thank you for always showing me there is room for my crazy ideas and that you can never take fundamentals for granted. I am also grateful to my committee members. Dr. Michael Dickey, for allowing me to work so extensively in his laboratory space and give me many ideas on how to create microstructures. Dr. Kirill Efimenko, for the years of jokes and good chats as well as teaching me many laboratory practices and techniques. Dr. Orlando Rojas and Dr. Julie Willoughby for their guidance and insight throughout my time at NC State. I also want to thank Dr. Erik Santiso for useful discussions on simulations techniques. I would also like to thank the U.S. Office of Naval Research (ONR) for providing financial support.

I would like to thank past and present members of the Genzer Interfacial Research Laboratories (GIRLs). Of special mention: Casey Galvin, Erich Bain, Evren Ozcam, Preeta Datta, Edwin Walker, Matt Mellilo, Pandi Kannan, and Julie Albert. I have to thank my NC State friends. Will, Dave, Jose, Josh, Alina, Christina and Steph you all made my years at NC State loads of fun. Finally, thank you to my family and my fiancée for their love and support.

TABLE OF CONTENTS

LIST OF FIGURES	vii
CHAPTER 1 Motivation and Overview	1
1.1 Motivation	1
1.2 Overview	4
1.2.1 Adsorption of “Soft” Spherical Particles onto Sinusoidally-Corrugated Substrates	5
1.2.2 Adsorption of Multiple Spherical Particles onto Sinusoidally-Corrugated Substrates	6
1.2.3 Adsorption of Size-Polydisperse Particles on Sinusoidally-Corrugated Surfaces	7
1.2.4 Marine Fouling on Model Microtextured Surfaces with Tailored Surface Chemistries	8
1.2.5 Future Work	9
1.3 Publications	10
1.4 References	11
CHAPTER 2 Adsorption of “Soft” Spherical Particles onto Sinusoidally-Corrugated Substrates	14
2.1 Introduction	17
2.2 Computer model and analysis of data	19
2.3 Results and Discussion	23
2.4 Conclusion	30
2.5 Acknowledgement	31
2.6 References	32
CHAPTER 3 Adsorption of Multiple Spherical Particles onto Sinusoidally-Corrugated Substrates	40
3.1 Introduction	43
3.2 Computer Model and Data Analysis	45
3.3 Results and Discussion	50
3.3.1 Hard Sphere Particles	50
3.3.2 "Soft" Sphere Particles	63
3.4 Conclusions	69
3.5 Acknowledgements	70
3.6 References	71
CHAPTER 4 Adsorption of Size-Polydisperse Particles on Sinusoidally-Corrugated Surfaces	75
4.1 Introduction	78
4.2 Computer Model	80

4.3 Results and Discussion	85
4.3.1 Polydisperse vs. Monodisperse Particle Distributions on Sinusoidal Substrates	85
4.3.2 Polydisperse and Monodisperse Particle Behavior Relative to Flat Substrates	92
4.3.3 Behavior of Bimodal Distributions on Sinusoidal Substrates	98
4.4 Conclusions	103
4.5 Acknowledgements	105
4.6 References	106
CHAPTER 5 Marine Fouling on Model Microtextured Surfaces with Tailored Surface Chemistries	110
5.1 Introduction	113
5.2 Experimental Methods	116
5.2.1 Creation of Microtextured Master Molds	116
5.2.2 Molding and Replication of Masters	118
5.2.3 Hot Embossing and Reflow of Thermoplastic Molds	118
5.2.4 Chemical Modification of Polystyrene and Polyvinyl Pyridines	119
5.2.5 Spraycoating of Microtextured Molds	120
5.2.6 Stabilization of Hydrophilic Coatings	121
5.2.7 Barnacle Cyprid Settlement and Removal Testing	121
5.3 Results and Discussion	122
5.3.1 Creating High Quality Microtextures	122
5.3.2 Effect of Molding with Thermoplastic Materials and Reflowing Polystyrene	127
5.3.4 Modification of Microtexture Surface Chemistry via Polystyrene and Polyvinyl Pyridine Derivatives	135
5.4 Conclusions	141
5.5 Acknowledgements	142
5.6 References	143
CHAPTER 6 Outlook	147
6.1 Outlook	147
6.1.1 Asymmetrical Particle Simulations	148
6.1.2 Optimization of Surface Topographies via Genetic Algorithm	149
6.1.3 Optimization of Spraycoating Technology and On-Demand Surface Chemistries	153
6.2 References	154

LIST OF FIGURES

- Figure 1.1.** Size scales of several relevant marine biofoulers. Bacteria typically exist in the 100s nm; Algal Zoospores on the order of 1s-10s μm ; Diatoms on the order of 10s μm ; Clam larvae on the order of 10s μm ; Barnacle cyprids on the order of 100s μm ; Oyster larvae on the order of 100s μm2
- Figure 1.2.** Approaches to designing low- and non-fouling surfaces. Chemical coatings typically target the conditioning film, disrupting the adsorption of proteins, small molecules and small marine foulers. Topographical coatings target the biggest problem marine foulers by disrupting the microenvironment they use to settle.4
- Figure 2.1.** a) Simulation setup depicting adhesion of particles with coarse grained polymer hairs on sinusoidally-corrugated substrates. b) Relative penetration depth (RPD), a ratio of particle depth inside of substrate feature to height of given surface feature. c) Topography match parameter (TMP), a factor of particle localization relative to valley and peak locations on periodic substrates.23
- Figure 2.2.** Positions of the center of mass (COM) for particles having $D=20$, $N=3$, $\sigma=0.04$ and $\epsilon=1$ kT adsorbing on substrates featuring sinusoidal corrugations featuring five different amplitudes and three different feature widths. The amplitudes are equal to (from the top to the bottom panel): 5 (green), 10 (magenta), 20 (blue), 40 (red), and 80 (black). The feature widths displayed are equal to: 5 (left column), 20 (middle column), and 80 (right column). Plotted circles represent core diameter of settled particles, polymer arms not shown.25
- Figure 2.3.** Relative penetration depth (RPD), topography match parameter (TMP), and adhesion energy (E_{adh}) as a function of the feature width for particles whose parameters are depicted in Figure 2 adsorbing onto substrates with a sinusoidal topographies having amplitudes equal to: 5 (green diamonds),

10 (magenta down-triangles), 20 (blue up-triangles), 40 (red circles), and 80 (black squares).	26
Figure 2.4. Relative penetration depth (RPD, top row), topography match parameter (TMP, middle row), and adhesion energy (E_{adh} , bottom row) as a function of the feature width for particles adsorbing onto substrates with a sinusoidal topographies having amplitudes equal to 5 (open symbols) and 80 (closed symbols). The black and red symbols represent two cases in which one system parameter was varied, <i>i.e.</i> , particle diameter (D , left column), length of polymer hair (N , second column from left), grafting density of hair (σ , second column from right), and adhesion energy (ϵ , right column).....	28
Figure 2.S1. Log(aspect ratio) versus Log(feature width) for adhesion energy of $D=20$, $N=3$, $\sigma=0.04$ and $\epsilon=1$ kT among RPD, TMP and adhesion energy measurements. Colored shades of green where lightest represents minimal values and darkest indicates maximal values of the respective measurement. In the regions where both RPD and TMP are light green (minimized) we see lowest adhesion energies.	36
Figure 3.1. Simulation setups and particle parameters including particle size (D), grafting density of hairs (σ), length of hairs (N) and the hair/substrate interaction parameter (ϵ)	49
Figure 3.2. Positions of hard sphere particles ($D=20$) on sinusoidally corrugated substrates with variable amplitude (A) and variable feature width (λ). Amplitude decreases moving down while feature width decreases moving right. Core of particles shown in blue-green, higher substrate features are lighter and lower surface features are darker.....	51
Figure 3.3. Adhesion energy per particle for hard sphere particles adsorbing onto sinusoidally-corrugated substrates. The adhesion energy has been normalized relative to adsorption of the same particles on flat substrates.	

The data are plotted for surfaces with various values of substrate feature width (λ) and feature height (A). The particle diameter is $D=20$53

Figure 3.4. a) Total adhesion energy and b) adhesion energy per particle for hard sphere particles adsorbing onto sinusoidally-corrugated substrates as a function of feature width (λ) normalized by the particle diameter (D) for substrates featuring different amplitudes (A) and 2 different particle sized. The color scale represents the number of particles adhering to the given substrate (blue=highest, red=lowest). The particle diameter is $D=20$ and 40 (see legend).55

Figure 3.5. Positions of hard sphere particles ($D=20$) on sinusoidally-corrugated surfaces with constant amplitude ($A=80$) and variable feature width (λ). Inter-particle interactions increase from top to bottom. Core of particles are shown in blue, higher surface features are lighter and lower surface features are darker.58

Figure 3.6. Order of arrival (red=soonest, blue=latest) of hard sphere particles ($D=20$) onto sinusoidally-corrugated surfaces with constant amplitude ($A=80$) and variable feature width (λ). Note that $\lambda=\infty$ corresponds to the flat substrate. The left, middle and right column denote data corresponding to different energy of particle/particle interactions (E_{PP}) relative to that of particle/substrate interaction (E_{PS}).60

Figure 3.7. Particle/particle contacts (red=lowest, blue=highest) for hard sphere particles ($D=20$) onto sinusoidally-corrugated surfaces with constant amplitude ($A=80$) and variable feature width (λ). Note that $\lambda=\infty$ corresponds to the flat substrate. The left, middle and right column denote data corresponding to different energy of particle/particle interactions (E_{PP}) relative to that of particle/substrate interaction (E_{PS}).61

Figure 3.8. Particle/surface adhesion energy (red=lowest, blue=highest) for hard sphere particles ($D=20$) onto sinusoidally-corrugated surfaces with constant amplitude ($A=80$) and variable feature width (λ). Note that $\lambda=\infty$

corresponds to the flat substrate. The left, middle and right column denote data corresponding to different energy of particle/particle interactions (E_{PP}) relative to that of particle/substrate interaction (E_{PS}).62

Figure 3.9. Particles covered with polymeric hair ($N=3$, $\sigma=0.04$) adsorbing onto sinusoidally-corrugated substrates with various wavelengths, *i.e.*, substrate feature widths. Substrate features decrease in amplitude going from top to bottom; the feature width (*i.e.*, wavelength) decreases going from left to right. Core of particles shown in blue, polymer "arms" shown in red, higher substrate features are depicted lighter while lower substrate features are marked darker.64

Figure 3.10. Adhesion energy per particle for particles covered with polymeric hair ($N=3$, $\sigma=0.04$) adsorbing onto sinusoidally-corrugated substrates. The adhesion energy has been normalized relative to adsorption of the same particles on flat substrates. The data are plotted for substrates with various values of feature width (λ) and feature height (A). The particle diameter is $D=20$66

Figure 3.11. a) Total adhesion energy and b) adhesion energy per particle for particles covered with polymeric hair ($N=3$, $\sigma=0.04$) adsorbing onto sinusoidally-corrugated substrates as a function of feature width (λ) normalized by the particle diameter (D) for substrates featuring different amplitudes (A) and 2 different particle sized. The color scale represents the number of particles adhering to the given substrate (blue=highest, red= lowest). The particle diameter is $D=20$68

Figure 4.1. Simulation schematic detailing the basics of the simulation setup. The substrate in gray, is defined by $F(x)=A*\sin(\lambda\pi x/x_{max})$ where A varies from 0 to 80 and λ varies from 5 to 80. The particles (green) are defined by their diameter (D) and interact with the substrate adhesively via an interactive shell (light red).83

- Figure 4.2.** (Top) Probability Density Functions for normal distributions with $D_{\text{core mean}} = 20$ and standard deviations (2, 4, 8). The distributions are binned by diameter and colored according to the legend on the right. (Bottom) Construction of a bimodal distribution $D_{\text{core meanA}} = 10$ (STD 1) and $D_{\text{core meanB}} = 40$ (STD 4) is plotted according to their probability density functions. $D_{\text{core meanA}}$ is colored blue while $D_{\text{core meanB}}$ is colored red. Their respective means are shown by the dashed vertical lines.84
- Figure 4.3.** Settlement of monodisperse (top) and polydisperse (bottom) particles on a variety sinusoidal surfaces with feature heights $FH = 5 - 80$ and feature widths (λ) relative to $\lambda/D = 0.25 - 4$. Wavelength increases from left to right; feature height increases from top to bottom; the particles are colored according to the legend by particle diameter.86
- Figure 4.4.** Varying the width of the normal distribution by modulating the standard deviation of the distribution function results showing settled particle counts as a function of feature width (λ). The distributions are composed of stacked columns colored by diameter of particles contribution. Increasing the standard deviation of the adsorbing particles leads to increased total particles adsorbed.88
- Figure 4.5.** Varying the width of the normal distribution by modulating the standard deviation of the distribution function results showing settled particle adhesion energy as a function of feature width (λ). The distributions are composed of stacked columns colored by diameter of particles contribution. Increasing the standard deviation of the adsorbing particles leads to increased total adhesion energy in some cases.89
- Figure 4.6.** Adsorbed particle counts (left column) and adhesion energy (right column) relative to the monodisperse case for normal distributions of standard deviations 4 (black squares), 2 (red circles) and 1 (blue triangles). Monodisperse plotted as horizontal green dashed line. More particles adsorbed for all distributions vs monodisperse. In some conditions, the

polydisperse conditions have lower energy than monodisperse and in other cases have higher energy.	91
Figure 4.7. Adsorbed particle counts (left column) and adhesion energy (right column) relative to their flat analogues for normal distributions of standard deviations 4 (black squares), 2 (red circles), 1 (blue triangles) and 0 (green downward triangles). Flat substrates plotted as horizontal black dashed line. Textured substrates outperform flat substrates below feature width of 20 in adhesion energy. At and above feature width 20, the textured substrates perform worse as excess surface area is readily available as more particles adsorb.	93
Figure 4.8. Adhesion energies of particle diameters (colored by bin) relative to that for flat substrates. Columns color corresponds to legend for diameter of particles. High amplitude substrates perform best at creating sub-optimal adhesion for particles greater than or equal to the feature width. Large particles sense the substrates as flat for very high and very low feature width.	95
Figure 4.9. (Top) Particle probability distributions of our normal random number generator (RNG) compared to the adsorbed particles on flat substrate. (Bottom) Fractional deviation from the flat substrates relative to the random number generator for particle sizes. Diameters colored as per legend.	97
Figure 4.10. Side views of adsorbed particle locations for two bimodal distributions, (Top) bimodal of 20 and 40 diameter, (Bottom) bimodal of 10 and 40 diameter. Evident that the further apart the particle mean diameters are, the greater the penetration into the substrate by the smaller particles.	99
Figure 4.11. Adhesion energy colored by contribution by particle diameter for two different bimodal distributions. Bimodal 5-20 has significantly higher adhesion energies as many more particles adsorb for most feature widths.	

	At large feature width, the second mode at diameter 40 is able to penetrate the surface and increase the adhesion energy.	101
Figure 4.12.	Adhesion energies relative to that for flat substrates by particle size (diameter). Column colors correspond to legend for diameter of particles. High amplitude substrates perform best at creating sub-optimal adhesion for particles greater than or equal to the feature width. Large particles sense the substrates as flat for very high and very low feature width. Bimodal 10-20 is more effective at most particle diameters.	102
Figure 4.13.	Adsorbed particle counts (left column) and adhesion energy (right column) on textured surfaces relative to flat substrates for various feature heights (black 80, blue 20 and green 5). Flat substrate marked by dashed black line at 1. Bimodal 5-20 causes significant problems for textured surfaces above $\lambda = 5$. For $\lambda \leq 20$ bimodal 10-20 is less adhesive to textured surfaces than flat substrates.	103
Figure 5.1.	Approaches to designing low- and non-fouling surfaces. Chemical coatings typically target the conditioning film, disrupting the adsorption of proteins, small molecules and small marine foulers. Topographical coatings target the biggest problem marine foulers by disrupting the microenvironment they use to settle.	115
Figure 5.2.	Size scale of nano- and micro-structure manufacturing technologies and a selection of marine fouling organisms. Sizes: Electron beam lithography (E-beam) 1s nm – 100s nm; Photolithography 100s nm – 10s μ m; Laser ablation 10s μ m – 10s mm; Machining/milling 100s μ m – 100s mm.	124
Figure 5.3.	Order of operations in developing master molds using negative photoresist photolithography. Negative photoresist (SU-8) is applied to silicon wafer and spincoated to a desired thickness. The resist is then baked to remove solvent and prepare for UV exposure. A photomask is applied followed by exposure to UV light (254 nm) causing cross-linking of the exposed areas of photoresist. After cross-linking the uncured photoresist is removed in a	

developer solution and dried. Red material indicates un-cross-linked photoresist, Blue indicates cross-linked photoresist.126

Figure 5.4. Selection of microtopographies created using negative photoresist (SU-8).

Images of PDMS (negative) replicas provided. (Top row) Aspect ratio 1 replicas; (Middle row) Aspect ratio 2 replicas; (Bottom row) overhead view of replicas. Columns correspond to feature sizes of 10, 40 and 200 μm respectively.....127

Figure 5.5. Hot embossing procedure to quickly create high quality replicas of master molds. Using a previously made master mold (flexible, low-surface energy material is best), and a sheet of desired thermoplastic a replica is formed.

Using downward force on the master and pressing it into the heated ($T > T_g$) thermoplastic (for polystyrene 150°C was used), the thermoplastic fills the master mold. After sufficient time (~ 10 min), the thermoplastic is cooled then released from the mold revealing the newly created replica part. This process was utilized using Sylgard-184 masters and Polystyrene (thermoplastic) sheet.128

Figure 5.6. Behavior of rectangular column surface features before and after thermal reflow. (Top row) Profile of surface features, (bottom row) overhead view of surface features. Thermal reflow using short time heating (5 min) of surface features above T_g of thermoplastic to transition rectangular surface features into sinusoid-shaped features.129

Figure 5.7. Settlement behavior of barnacle cyprids on rectangular columns versus reflowed sinusoids of same dimensions plotted versus width of surface features. Note the y-axis starts below zero to show y-values of zero. Behavior is similar at small dimensions but at $80 \mu\text{m}$ the sinusoid prevents any cyprids from settling while the columns allow some but show significant improvement over flat substrates. Above the dashed line indicates higher settlement, worse performance, relative to flat substrates.

Below the dashed line indicates lower settlement, better performance, relative to flat substrates.	131
Figure 5.8. Behavior of barnacle cyprid settlement on identical surface structures with differing surface chemistries. (Top) Sylgard-184 surface features show strong dependence of settlement on surface feature dimensions, specifically higher aspect ratio surfaces perform much better across all sizes, including zero settlement at 200 μm . (Bottom) PS-P4VP coated surfaces show similar settlement below 100 μm but a significant drop-off is observed above 100 μm , including zero settlement at 200 μm for both aspect ratios.....	133
Figure 5.9. Results of extensive testing of topographically-corrugated samples with barnacle cyprid settlement assays. Relative settlement behavior, independent of surface chemistry, of various sized topographies is plotted as a function of the surface feature sizes. Improvement over flat surface analogues is seen for most surfaces around 70 μm for both aspect ratios and for all samples greater than 100 μm . Above the dashed line indicates higher settlement, worse performance, relative to flat substrates. Below the dashed line indicates lower settlement, better performance, relative to flat substrates.....	134
Figure 5.10. Topographically-corrugated sample surface chemistry modified via spraycoating with a variety of modified polymers forming conformal coatings. A polymer solution prepared in (relatively) volatile solvent is sprayed directly onto substrates yielding modified surface chemistries of the topographies.	137
Figure 5.11. Utilizing modified polymers the surface chemistry including surface energy and contact angle can be changed dramatically. (Left) Procedure to stabilize hydrophilic polymers to variety of substrate materials (PDMS, UVO-PDMS, PS sheet, PS melt). (Right) Substrate materials shown with application of BP4VP after 2 weeks submersion in artificial seawater.	138

Figure 5.12. (Top) Settlement % (blue columns) of 3-day old <i>B. Amphitrite</i> cyprids larvae on the test surfaces after 24 h. (Bottom) Removal % (red columns) of 6-day old juvenile barnacles (<i>B. Amphitrite</i>) from the test surfaces using a water jet with a calibrated impact pressure of 62 kPa.....	140
Figure 5.S1. IR spectra for quaternization and betainization of P2VP and P4VP. IR spectra for sulfonation of PS.....	146
Figure 6.1. Concept of an algal zoospore, asymmetric particle to be used in the adhesion model. Depicted is the potential method of settlement and interaction with the substrate. This particle might use long flagella to sense the surface and drag itself in for settlement.	149
Figure 6.2. Schematic of genetic algorithm steps in optimizing a sinusoidal surface for minimal adhesion with a spherical particle of diameter ($D=20$). This algorithm undergoes several generations to reach convergence upon local or global minima.	151
Figure 6.3. Genetic algorithm results from minimizing the adhesion energy of a diameter, $D=20$, particle on a bi-directional sinusoidal surface. (Top left) Shown is the distribution of adhesion energies for each generation of candidate surfaces. (Bottom left) Displays the highlighted minima of each generation of surfaces, showing how quickly the algorithm converges towards a set of desirable candidates. (Right) Angled (large) and overhead (small) views of the $D=20$ particle at its maximum energy location of high (blue) and low (orange) energy surfaces.....	152

CHAPTER 1

Motivation and Overview

1.1 Motivation

Marine biofouling is a robust and complex problem facing the world's navies and shipping industries. We define biofouling broadly as non-specific adhesion and build-up of biomolecules and microorganisms on man-made surfaces and that this build-up decreases the performance of the surface. Biofouling is especially troublesome in marine environments as ship hulls are continuously exposed to a wide variety of potential foulants. Upon mere minutes of immersion in seawater, man-made surfaces can begin to build-up a layer of biomolecules and bacteria known as a biofilm [1]. Once the biofilm is established, larger microorganisms are recruited to the surface, typically in their larval stages. A variety of known marine biofoulers and their sizes are depicted in **Figure 1.1**. The larval biofoulers settle onto surfaces and begin the rest of their life cycles entering adulthood where they grow much larger in size. This growth in size leads to severe degradation of surface performance for ship hulls due to the increased surface roughness created. This buildup of biofouling increases fuel costs for shipping and increases frequency of dry-docking [1].

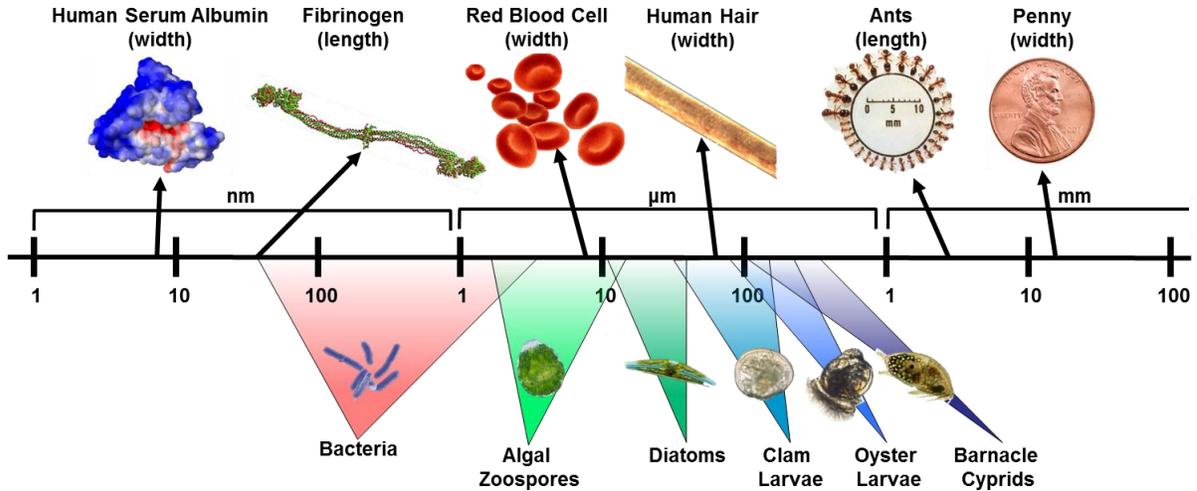


Figure 1.1. Size scales of several relevant marine biofoulers. Bacteria typically exist in the 100s nm; Algal Zoospores on the order of 1s-10s μm ; Diatoms on the order of 10s μm ; Clam larvae on the order of 10s μm ; Barnacle cyprids on the order of 100s μm ; Oyster larvae on the order of 100s μm .

Over the past few decades, several important paint-based technologies were developed to combat the growth of biofilms and microorganisms on ship hulls. These technologies used primarily transition metal complexes, copper and tin being the most prominent transition metals of choice. These transition metal complexes were used for their biocidal properties. However, in the last two decades significant environmental concerns have been raised about the use of such materials leading to their ban in many harbors around the world [1]. In the wake of such bans a technology gap existed where new non-toxic coatings were needed. Research into new coatings can be thought to target two essential elements of the biofouling process; coatings to prevent or inhibit the formation of biofilms and coatings to prevent or inhibit the settlement of the larval microorganisms. **Figure 1.2**

displays this concept briefly and outlines how one might design coatings capable of preventing (or at least minimizing) biofouling. In general, research efforts have continued in developing effective chemical coatings aimed at preventing the formation of biofilms, on the one hand, and conceiving and fabricating topographical coatings aimed at inhibiting the settlement of microorganisms, on the other hand. Significant progress has been made in the area of chemical coatings typically based on low-fouling polymers [1-10]. For example, ethylene glycol [2,6,10], fluorinated polymers [10] or some charge-bearing surfaces [7-9] are capable of minimizing (at least temporarily) bioadsorption. In the area of topographical coatings, progress has been sparser and fewer contributions have been made towards understanding the fundamentals of their effectiveness. Examples include the Sharklet patterns [11,12], hierarchical wrinkles with multiple dimensions [13,14] and corrugated periodic structured substrates [15-20]. Some studies have alluded to attachment point theory [15-18] and investigated sinusoidal topographies with promising results; yet those studies did not develop a substantial theoretical basis for predicting fouling behavior.

This is the juncture, at which this Ph.D. Dissertation takes off. We aim to create better fundamental understanding of topographical coatings. We endeavor to accomplish this goal by using a combination of computer simulations and experiment. In addition, we plan to combine the topographical coatings with chemical coatings experimentally using the same type of paint-spraying (spraycoating) technology that industry currently utilizes.

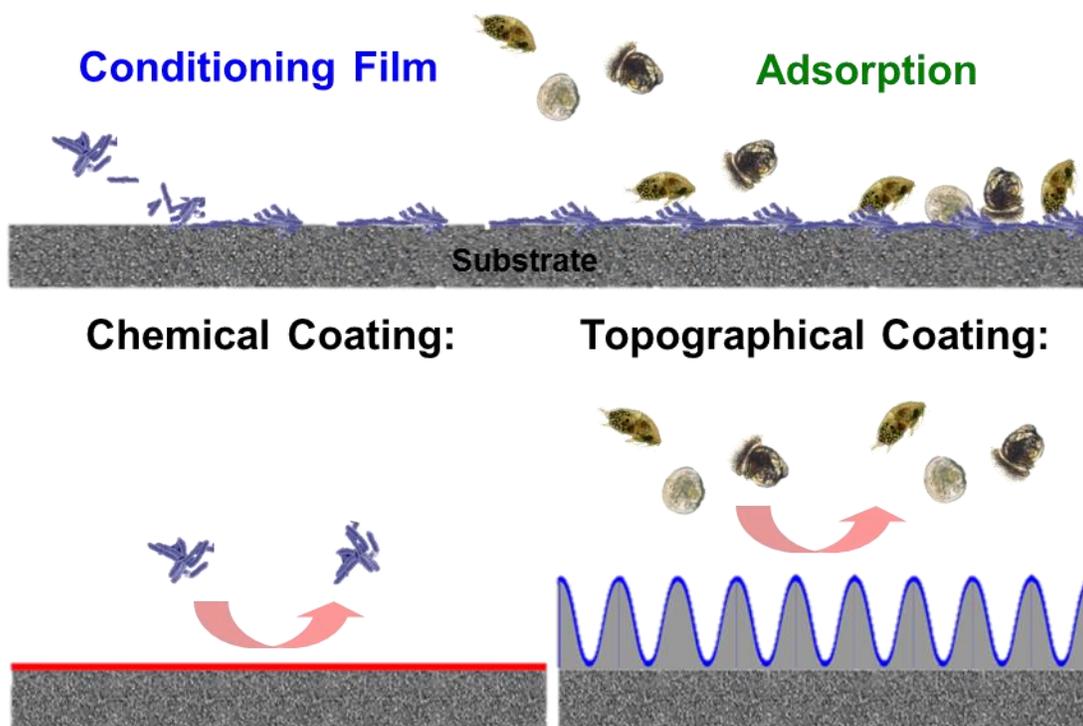


Figure 1.2. Approaches to designing low- and non-fouling surfaces. Chemical coatings typically target the conditioning film, disrupting the adsorption of proteins, small molecules and small marine foulers. Topographical coatings target the biggest problem marine foulers by disrupting the microenvironment they use to settle.

1.2 Overview

This section provides a summary of the rest of the Ph.D. Dissertation. All chapters offer their own literature review and references.

1.2.1 Adsorption of “Soft” Spherical Particles onto Sinusoidally-Corrugated Substrates

In Chapter 2, we built a Monte Carlo adhesion computation model to simulate a system of sinusoidally textured substrates interacting with a variety of so-called “soft” particles. These particles consist of a hard core of diameter (D) and a corona of coarse-grained polymer chains of length (N) grafted to the core at grafting density (σ). The polymer chains interact with the substrate lattice elements via pairwise non-specific interactions (ϵ). Substrate parameters include wavelength or feature width (λ) and amplitude or feature height (A). This simulation scheme takes aim at comprehending single particle adsorption behavior to identify the highest adhesion energy locations for given test surfaces and elucidate test surfaces that reduce adhesion energy and reduce the number of high adhesion locations. We define an effective surface as one that reduces either number of adsorbed particles or total adhesion energy of adsorbed particles relative to flat substrates. Our results show that the wavelength of substrate features plays a pivotal role in governing the settlement of single particle systems. At $\lambda = D/2$ we observe a minimum in the adhesion energy and at $\lambda = D$ we observe a uniform settlement location of the particles. Increasing N leads to a reduction in the effectiveness of substrate topography to direct the settlement of individual particles into specific sites on the substrate. This work was published in 2014 in *Soft Matter* [21].

1.2.2 Adsorption of Multiple Spherical Particles onto Sinusoidally-Corrugated Substrates

In Chapter 3, we built upon our previous Monte Carlo adhesion computer simulation model to study a system of sinusoidally-corrugated substrates interacting with a variety of so-called “soft” particles as well as hard-core particles. The major change from the model in Chapter 2 is the use of multiple particles adsorbing to observe their collective behavior on such sinusoidal substrates. In this model, once a single particle adheres to the substrate a new particle is introduced into the lattice to begin settlement. Through this multi-particle settlement mode, we explore the interplay among the characteristics of the particles (*i.e.*, size, interaction shell) and the substrates (*i.e.*, wavelength and periodicity) as well as inter-particle interactions. We report that the adhesion of particles with an effective interaction shell to the substrates is reduced dramatically when the particle size (D) is larger than the feature width (λ) of the periodic substrate ($D > \lambda$) similar to our results in Chapter 2. The settlement of particles with flexible hair on the sinusoidally corrugated substrates is more complex. Specifically, the presence of flexible polymeric hairs makes the particle settlement more likely to occur on nearly all substrates studied irrespective of the characteristics of the substrate. As before, we define effectiveness of our sinusoidal substrates based on their ability to reduce total adhesion energy or total number of adsorbed particles when compared to flat substrates. This work was published in 2014 in Langmuir [22].

1.2.3 Adsorption of Size-Polydisperse Particles on Sinusoidally-Corrugated Surfaces

In Chapter 4, we expand on our model of core-shell particles to analyze the effectiveness of single feature widths (*i.e.*, wavelength, λ) against distributions of particle sizes settling at once. We do this by generating various particle distributions using a normally distributed random number generator, creating the diameters (D_{core}) of the adsorbing particles. We vary the standard deviation (STD) of this normal distribution from 0 (monodisperse) to 8 (highly polydisperse) with a mean diameter ($D_{\text{core mean}}$) of 20. We continue to define the effectiveness of our sinusoidal substrates as reducing the adsorbed particle count or total adsorbed adhesion energy when compared to flat substrates. We find that our sinusoidal substrates continue to be effective at reducing these quantities, particularly adhesion energy, when $\lambda/D_{\text{core mean}} \sim 0.5$. However, closer examination reveals that the smaller particles in the distribution $D_{\text{core}} \leq 10$ adhere more strongly to corrugated substrates than to flat substrates. As a result, these small particles would be more difficult to remove from the substrate. We conclude this work by changing the particle distribution from a single normal distribution to a bimodal distribution composed of two normal distributions of differing mean values ($D_{\text{core meanA}}$ and $D_{\text{core meanB}}$). We find that beyond a size ratio of 2 (size ratio = $D_{\text{core meanB}}/D_{\text{core meanA}}$), the sinusoidal surfaces are no longer effective in minimizing particle adsorption as there are too many small particles adsorbing strongly on the surfaces, making them ineffective. We conclude that in order to combat adsorption of particles with bimodal (or multimodal) distribution, we would need to employ surfaces featuring nested topographies with different feature widths and heights or add chemical

coatings to reduce fouling of the smaller particles. This chapter is a manuscript currently in preparation.

1.2.4 Marine Fouling on Model Microtextured Surfaces with Tailored Surface Chemistries

In Chapter 5, we discuss our experimental efforts aimed at gaining fundamental understanding of the role of surface topography in reducing marine biofouling, testing and validating our model predictions, and combining chemical coatings with topographical coatings. We begin by selecting a microstructure manufacturing technique, photolithography, which allows us to access the size range of the microorganisms that cause much of the marine biofouling. In this case we primarily desire to study barnacle cyprids, which are ~100s μm in size. We create a set of master molds, using a negative photoresist (SU-8), in two aspect ratios (1 and 2) and five feature widths (10, 20, 40, 100, and 200 μm). We then replicate these molds using soft lithography via a commercial silicone elastomer (Sylgard-184) and replicate again the silicone molds into positive replicas by hot embossing them into thermoplastics (polystyrene). We develop a technique termed “thermal reflow” to turn the rectangular profiles created by the photolithography masters into sinusoidal-like profiles as had been tested in our modeling work. Samples of rectangular and sinusoidal profiles are tested against barnacle cyprids in settlement assays revealing significant reduction in adsorption when the feature width (λ) of our periodic features is just smaller than the cyprids themselves ($\lambda/D_{\text{cyprid}} \sim 0.25\text{-}1.0$). Specifically for aspect ratio 2 surfaces at 100 and 200 μm feature width, we observe little to no settlement of barnacle cyprids. We also report that in

the Sylgard-184 replicas, the sinusoidal profile outperforms the rectangular profiles. This observation coincides with many of our model predictions from Chapters 2-4. Continuing this work, we developed low-fouling polymers in conjunction with a spraycoating delivery method to coat microtextured surfaces. These polymers cross-link to form polymer network gels, creating stable coatings. In barnacle cyprid settlement testing, one polymer (betainized poly(4-vinyl pyridine)) only allowed 15% of cyprids to attach. When juvenile cyprids were grown on this same polymer, over 45% were released upon exposure to a 62 kPa impact pressure water jet. This work is a manuscript in preparation.

1.2.5 Future Work

In Chapter 6, we outline ongoing opportunities and avenues for new research that could augment the work outlined in this Ph.D. Dissertation. First, we discuss opportunities of introducing asymmetrical particles that resemble specific marine microorganisms into the models shown in Chapters 2-4. Second, we outlined avenues of extending our computer modeling capabilities to move beyond predefined sinusoidal profiles by means of a genetic algorithm that finds an optimal combination of a feature width and feature height to minimize particle adhesion. This method could create an entire new set of surface textures, uniquely built for specific shapes of particles or particle distributions. Finally, we comment on new opportunities in the area of functional chemical coatings based on commodity plastics. There is indeed significant room to expand our work in on-demand surface chemistries for coatings microstructures. The spraycoating procedure needs refinement since the simple glass sprayer we used may be insufficient to spray thin (~100 nm) coatings. In addition, the cross-linking

of the low-fouling polymers into polymer network gels should be further examined to improve both the reduction of marine microorganism settlement and the release of those microorganisms that do attach.

1.3 Publications

Chapters 2-5 are based on the following publications:

Chapter 2: Adsorption of “Soft” Spherical Particles onto Sinusoidally-Corrugated Substrates

Chapter 3: Adsorption of Multiple Spherical Particles onto Sinusoidally-Corrugated Substrates

Chapter 4: Adsorption of Size-Polydisperse Particles on Sinusoidally-Corrugated Surfaces

Chapter 5: Marine Fouling on Model Microtextured Surfaces with Tailored Surface Chemistries

1.4 References

1. Grozea, C.M.; Walker, G.C. Approaches in designing non-toxic polymer surfaces to deter marine biofouling. *Soft Matter* **2009**, *5*, 4088-4100.
2. Krishnan, S.; Weinman, C.J.; Ober, C.K. Advances in polymers for anti-biofouling surfaces. *Journal of Materials Chemistry* **2008**, *18*, 3405-3413.
3. Chapman, R.; Ostuni, E.; Liang, M.; Meluleni, G.; Kim, E.; Yan, L., Pier, G.; Warren, H.S.; Whitesides, G.M. Polymeric thin films that resist the adsorption of proteins and the adhesion of bacteria. *Langmuir* **2001**, *17*, 1225-1233.
4. Therien-Aubin, H.; Chen, L.; Ober, C K. Fouling-resistant polymer brush coatings. *Polymer* **2011**, *52*, 5419-5425.
5. Gunkel, G.; Weinhart, M.; Becherer, T.; Haag, R.; Huck, W.T.S. Effect of polymer brush architecture on antibiofouling properties. *Biomacromolecules* **2011**, *12*, 4169-4172.
6. Dimitriou, M.D.; Zhou, Z.; Yoo, H.; Killops, K.L.; Finlay, J.A.; Cone, G.; Sundaram, H.S.; Lynd, N.A.; Barteau, K.P.; Campos, L.M.; Fischer, D.A.; Callow, M.E.; Callow, J.A.; Ober, C.K.; Hawker, C.J.; Kramer, E.J.. A general approach to controlling the surface composition of poly(ethylene oxide)-based block copolymers for antifouling coatings. *Langmuir* **2011**, *27*, 13762-13772.
7. Zhang, Z.; Chao, T.; Chen, S.; Jiang, S. Superlow fouling sulfobetaine and carboxybetaine polymers on glass slides. *Langmuir* **2006**, *22*, 10072-10077.
8. Zhang, Z.; Finlay, J.A.; Wang, L.; Gao, Y.; Callow, J.A.; Callow, M.E.; Jiang, S. Polysulfobetaine-grafted surfaces as environmentally benign ultralow fouling marine coatings. *Langmuir* **2009**, *25*, 13516-13521.
9. Li, G.; Xue, H.; Gao, C.; Zhang, F.; Jiang, S. Nonfouling polyampholytes from an ion-pair comonomer with biomimetic adhesive groups. *Macromolecules* **2010**, *43*, 14-16.
10. Krishnan, S.; Wang, N.; Ober, C. K.; Finlay, J. A.; Callow, M. E.; Callow, J. A.; Hexemer, A.; Sohn, K. E.; Kramer, E. J.; Fischer, D. A. Comparison of the fouling release properties of hydrophobic fluorinated and hydrophilic PEGylated block copolymer surfaces: Attachment strength of the diatom *Navicula* and the green alga *Ulva*. *Biomacromolecules* **2006**, *7*, 1449-1462.

11. Carman, M.; Estes, T.; Feinberg, A.; Schumacher, J.; Wilkerson, W.; Wilson, L.; Callow, M.; Callow, J.; Brennan, A. Engineered antifouling microtopographies - correlating wettability with cell attachment. *Biofouling* **2006**, *22*, 11-21.
12. Schumacher, J. F.; Carman, M. L.; Estes, T. G.; Feinberg, A. W.; Wilson, L. H.; Callow, M. E.; Callow, J. A.; Finlay, J. A.; Brennan, A. B. Engineered antifouling microtopographies - effect of feature size, geometry, and roughness on settlement of zoospores of the green alga *Ulva*. *Biofouling* **2007**, *23*, 55-62.
13. Efimenko, K.; Rackaitis, M.; Manias, E.; Vaziri, A.; Mahadevan, L.; Genzer, J. Nested self-similar wrinkling patterns in skins. *Nature Materials* **2005**, *4*, 293-297.
14. Efimenko, K.; Finlay, J.; Callow, M.E.; Callow, J.A.; Genzer, J. Development and testing of hierarchically wrinkled coatings for marine antifouling. *ACS Applied Materials & Interfaces* **2009**, *1*, 1031-1040.
15. Berntsson, K.; Andreasson, H.; Jonsson, P.; Larsson, L.; Ring, K.; Petronis, S.; Gatenholm, P.. Reduction of barnacle recruitment on micro-textured surfaces: Analysis of effective topographic characteristics and evaluation of skin friction. *Biofouling* **2000**, *16*, 245-261.
16. Aldred, N.; Scardino, A.; Cavaco, A.; de Nys, R.; & Clare, A.S. Attachment strength is a key factor in the selection of surfaces by barnacle cyprids (*balanus amphitrite*) during settlement. *Biofouling* **2010**, *26*, 287-299.
17. Scardino, A.; Harvey, E.; De Nys, R. Testing attachment point theory: Diatom attachment on microtextured polyimide biomimics. *Biofouling* **2006**, *22*, 55-60.
18. Vasudevan, R.; Kennedy, A.J.; Merritt, M.; Crocker, F H.; Baney, R.H. Microscale patterned surfaces reduce bacterial fouling-microscopic and theoretical analysis. *Colloids and Surfaces B: Biointerfaces* **2014**, *117*, 225-232.
19. Perera-Costa, D.; Bruque, J M.; Gonzalez-Martin, M.; Gomez-Garcia, A.C.; Vadillo-Rodriguez, V. Studying the influence of surface topography on bacterial adhesion using spatially organized microtopographic surface patterns. *Langmuir* **2014**, *30*, 4633-4641.
20. Grinthal, A.; Aizenberg, J. Mobile interfaces: Liquids as a perfect structural material for multifunctional, antifouling surfaces. *Chemistry of Materials* **2014**, *26*, 698-708.
21. Schoch, P. K.; Genzer, J. Adsorption of "soft" spherical particles onto sinusoidally-corrugated substrates. *Soft Matter* **2014**, *10*, 7452-7458.

22. Schoch, P. K.; Genzer, J. Adsorption of Multiple Spherical Particles onto Sinusoidally Corrugated Substrates. *Langmuir* **2014**, 30, 9407-9417.

CHAPTER 2

Adsorption of “Soft” Spherical Particles onto Sinusoidally-Corrugated Substrates

Published peer-reviewed article:

Schoch, P. K.; Genzer, J. Adsorption of "Soft" Spherical Particles onto Sinusoidally-Corrugated Substrates. *Soft Matter* **2014**, 10, 7452-7458.

Adsorption of “Soft” Spherical Particles onto Sinusoidally-Corrugated Substrates

Phillip K. Schoch, and Jan Genzer*

Department of Chemical and Biomolecular Engineering, North Carolina State University,
911 Partners Way, Raleigh, North Carolina 27695, United States

Abstract

We utilize a Monte Carlo simulation scheme based on the bond fluctuation model to simulate settlement of "soft" adhesive particles onto sinusoidally-corrugated substrates. Particles are composed of a hard inner core with a "soft" adhesive shell made of surface-grafted polymer chains. These chains adhere to surface lattice sites via pair wise non-specific interactions acting between the substrate and the last two segments of the polymer grafts on the particle. This simulation scheme is aimed at comprehending single particle adsorption behavior to find the highest adhesion energy locations for given test surfaces and elucidate test surfaces that reduce adhesion energy. Parameters in this study are set by the particle, the substrate and an interaction parameter between the two. Particle parameters include core diameter (D), grafting density of polymer (σ) and length of grafted polymer (N). Substrate parameters include wavelength (λ) and amplitude (A). Our results show that the wavelength of substrate features plays a significant role in the settlement of single particle systems. At $\lambda = D/2$ we observe a minimum in the adhesion energy and at $\lambda = D$ we observe a uniform settlement location of the particles. Increasing N leads to a reduction in the

effectiveness of substrate topography to direct the settlement of individual particles into specific sites on the substrate.

2.1 Introduction

The adhesion and organization of particles on materials surfaces is an area of great interest for many technologies ranging from anti-fouling coatings to sensors to sorting polydisperse particles [1-16]. Here we focus on interaction of particles decorated with long-chain flexible hairs whose “sticky” ends govern particle interactions with topographically-corrugated substrates. Examples that resemble systems with similar design include many biological materials, including, microorganisms (*i.e.*, cyprids, zoospores), bacteria, and proteins that interact with substrates. While in some situations adhesion of such particles is favored (*i.e.*, cell growth matrices, particle sorting), in others, (*i.e.*, anti-biofouling coatings), one seeks to avoid the attachment of these particles to or at least reduce their population on the materials surfaces. Many diverse approaches have been proposed to accomplish these goals. Those involve typically either varying the chemical composition or some physical property of the substrate, *i.e.*, modulus, topography. In recent years, most efforts aiming at reducing the adsorption of biofoulers at surfaces have concentrated on utilizing chemistry by generating ethylene-glycol [17,18,22] and charge-containing surfaces [23,24,25]. A less studied, yet equally important, area involves the utilization of engineered substrate topologies in combating the settlement of foulants on surfaces. While a few studies have demonstrated the promise in reducing fouling by utilizing topographically-corrugated surfaces featuring periodic Sharklet patterns [29], hierarchical wrinkles with multiple dimensions [1,30], corrugated periodic structured surfaces [18,25,29,31-35] or even substrates with random topographical protrusions, very little is understood about the mechanisms by which these

surfaces work or which morphologies are best suited towards reducing biofouling. Some work has also suggested an attachment point theory used in association with testing sinusoidal surfaces [29,31,32,36,37]. However, this attachment point theory has not been developed into a working model.

In an effort to better understand the role of surface topography in reducing biofouling and to create a predictive tool to design candidate surfaces, we have developed a Monte Carlo computer simulation scheme that aims to replicate the behavior of fouling particles interacting with periodic topographically corrugated substrates. Foulants include a wide set of organisms ranging from bacteria to micro- and macro-foulers, which encompass a size range from hundreds of nanometers to hundreds to (hundreds of) thousands of microns [30]. The interaction energies of these species in terms of energy per contact point on the substrate are not known. Foulants are simulated as hard-core spherical particles covered with coarse-grained polymeric “hairs” protruding from their surface. In this work we explore systematically the adsorption of a single “hairy” particle on sinusoidally-corrugated substrates as a function of the properties of the particle, *i.e.*, the particle diameter, grafting density of adhesive hairs, length of hairs, number of adhesive elements per hair, and energy per polymer coarse grained element-to-surface contact, and the characteristics of the underlying substrate, *i.e.*, the frequency and amplitude of the topographical features. In doing so we seek to identify conditions under which the use of *periodic* substrate structures can effectively reduce particle adhesion. Hence, the scenario studied here represents effectively the adhesion of a single organism, *i.e.*, adsorption in low concentration regime. Simultaneous adsorption of multiple particles onto topographically corrugated substrates,

including the effect of particle crowding and inter-particle interaction, will be addressed elsewhere [39].

2.2 Computer model and analysis of data

We employ a Monte Carlo (MC) computer simulation scheme to model the behavior of particles interacting with topographically corrugated surfaces. These particles adhere via polymeric “hairs” anchored to their surface; the movements of particles and the flexible “hairs” are governed by the bond fluctuation model (BFM) [38]. The substrates, particles and their “hairs” exist in a cubic lattice comprising $500 \times 500 \times 500$ lattice cells. BFM dictates a set of 108 possible bond vectors allowed in a cubic lattice as shown by the set of moves: $P(2,0,0) \cup P(2,1,0) \cup P(2,1,1) \cup P(2,2,1) \cup P(3,0,0) \cup P(3,1,0)$ and their permutations and sign inversions of such [38]. All moves in the BFM are selected randomly and attempted with favorable moves tending towards an increase in adhesion energy. To strike a balance between the entire particle moving and each segment of the surface-grafted polymer moving in the lattice, we operate each on different time scales. In this case, within a MC simulation the Monte Carlo steps act as a time parameter. The set of possible moves in this system consist of coarse-grained polymer chain moves and movement of the entire particle. Polymer chains move on a faster time scale than moves of the overall particle thus the move probabilities are balanced as such. While this scenario creates a pseudo-realistic movement, system testing was performed at high number of MC steps to ensure particles were able to reach multiple maxima in their allotted settlement time. There is no preferential

direction imposed on the movement of the particles, *i.e.*, no gravitational or other external force effects, as the particles move spontaneously in three-dimensional space. In the results presented, all particles begin from the same spot located above the center of the test substrate. However, we note that the initial position of the particle in the simulation box does not affect the final outcome, as verified by independent runs, in which particles were allowed to start from randomly chosen initial positions above the substrate. Changes to adhesion energy of the system are handled by the Metropolis decision algorithm where any move that increases the interaction energy between the substrate and the adhesion points on the polymeric grafts is accepted, but any move that causes a decrease in interaction energy is allowed at a probability proportional to $e^{\Delta E/kT}$, where ΔE is $E_{\text{adhesion},i} - E_{\text{adhesion},i-1}$ (Note the difference in sign convention as this deals with energy of adhesion which we treat as a positive quantity thus the algorithm seeks to maximize energy of the system). This simulation scheme maintains randomness in the system thus allowing the particle to escape local energy minima. These MC simulations are given an arbitrary amount of time (we use 1,000 steps per polymer coarse grained element) to first equilibrate the surface anchored arms before the particle itself is allowed to move as a whole. Once released the particle moves freely in any direction within the lattice and the simulation ends after a predetermined set of MC steps. The number of MC steps is adjusted to give each segment of the anchored polymer chains and the particle enough time to sample the surfaces many times, on the order of 10,000 per chain segment. It should also be noted that the use of a lattice may result in non-monotonous behavior in our data analysis due to discretization.

Figure 2.1a provides the layout of the simulation set up and defines the parameters of the substrates and the particles employed in the simulation. Specifically, the sinusoidal topographies with adjustable amplitude and wavelength, referred to later as feature height and feature width, respectively. Data discussed in this letter include a set of five feature heights and five feature widths, which combined create 25 unique surfaces for each set of particle conditions tested. The particles are defined by their core diameter (D), number of repeat segments in the anchor arms (N), grafting density of arms on the particle surface (σ), and the interaction potential acting between the adhesive arms points (last two segments of the flexible “hair”) and the surface (ϵ). During the MC simulation we track positional data of all particle-anchored arms and the center of mass of the particle as well as the current adhesion energy of the system. Each set of data discussed here represents the compilation and average of 1,000 identical runs for a single particle for each set at a given combination of the simulation parameters.

In addition to evaluating the aforementioned parameters from the MC simulation, we define two new quantities, *i.e.*, relative penetration depth (RPD) and topography match parameter (TMP), which help track the locus of the particles on the topographical surfaces and determine the fidelity with which the particles “replicate” the surface features, respectively. The RPD of the adsorbing particle inside the periodic structures of surface is defined as:

$$\text{RPD} = \frac{Z_{\text{lowest particle}} - Z_{\text{peak}}}{Z_{\text{peak}} - Z_{\text{valley}}} \quad (1)$$

In Equation (1) $z_{\text{lowest particle}}$ and z_{peak} represent the z position of the bottom of the particle and the top of the substrate feature, respectively, as shown in **Figure 2.1b**. Negative values of “penetration” denote particles that have penetrated the valleys of the substrate. In contrast positive “penetration” values represent particles that lay above the substrate. Penetration = 0 denotes a situation, where the lowest point of the solid portion of the particle (*i.e.*, excluding hairs) is in line with the dashed horizontal line marked in **Figure 2.1b**. As will be apparent from the subsequent discussion, the “penetration” parameter is helpful in analyzing the relative performance of surfaces in preventing particles from settling in lower substrate locations. While “penetration” characterizes the position of the particle in the z -direction of the substrate, we define a parameter unique to periodic surfaces, *i.e.*, TMP (*cf.* **Figure 2.1c**), which characterizes the position of the particle along the horizontal axis:

$$\text{TMP} = \frac{\sum_i^{\text{\# of trials}} x_{\text{COM},i} - x_{\text{valley}}}{\text{\# of trials}} \quad (2)$$

In Equation (2) x_{COM} and x_{valley} represent the coordinates of the center of mass (COM) and the valley of the sinusoidal profile (*i.e.*, the point of the particle where $z = z_{\text{valley}}$), respectively. Values of TMP approaching 1 represent cases where the particle COM coincides with the peak in the sinusoidal substrate. In contrast, TMP values that converge towards 0 denote situations where the COM of the particle moves towards the valley in the sinusoidal substrate. A low TMP value with a corresponding low standard deviation implies highly ordered settlement in the valley position. As will be demonstrated later, the TMP

parameter determines how well the substrate drives the particles to adopt discrete and well-defined settlement locations on the surface.

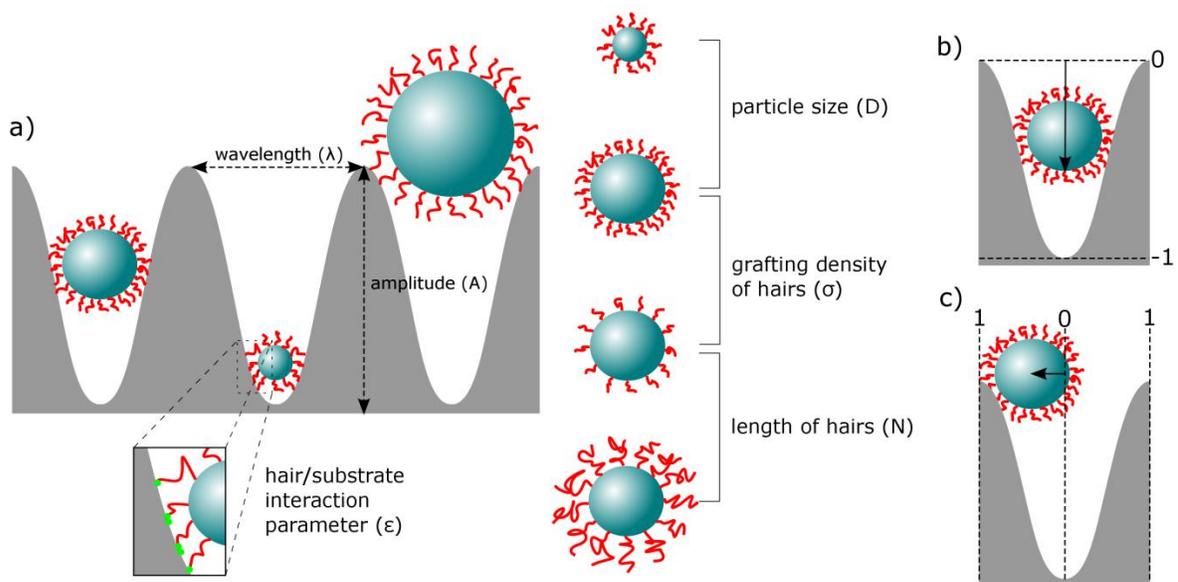


Figure 2.1. a) Simulation setup depicting adhesion of particles with coarse grained polymer hairs on sinusoidally-corrugated substrates. b) Relative penetration depth (RPD), a ratio of particle depth inside of substrate feature to height of given surface feature. c) Topography match parameter (TMP), a factor of particle localization relative to valley and peak locations on periodic substrates.

2.3 Results and Discussion

In **Figure 2.2** we plot the positions of the center of mass of the largest particles ($D=20$) having the shortest length of the polymeric hair ($N=3$) and grafting density ($\sigma=0.04$) at the intermediate adhesion energy studied ($\epsilon=1$ kT). The data in **Figure 2.2** demonstrate visually the dramatic differences in particle settlement as a function of the periodicity (*i.e.*, feature width) and the amplitude (*i.e.*, feature height) of the substrate. In in **Figure 2.3** we

plot the values of the RPD, TMP and adhesion energy (along with the standard deviation for the latter two quantities) as a function of the feature width for various values of the feature amplitude. For substrates that possess the largest feature width, the particles settle on lower portions of the substrate (*i.e.*, valleys) and are somewhat spread out, particularly at substrates with lower feature heights. In the small wavelength case, the particles settle relatively uniformly across the substrate. Substrates, whose feature width matches the diameter of the particles, perform glaringly differently. Specifically, the particles settling on such substrates are allowed to reside only in discrete locations defined by the valleys of the topography. Thus the total number of particles settled would be the lowest when the feature width of substrates with periodic topographies featuring sinusoidal profile matches the size of the adsorbing particles because the particles are allowed to reside only in very specific places on the substrate (relative to situations where the particle size and the substrate features do not match). Having established the essential attributes of the system set up and the effect of the substrate periodicity and amplitude on particle population on the substrate, we provide below more detailed account of the effect of the various system parameters that govern the observed phenomenon.

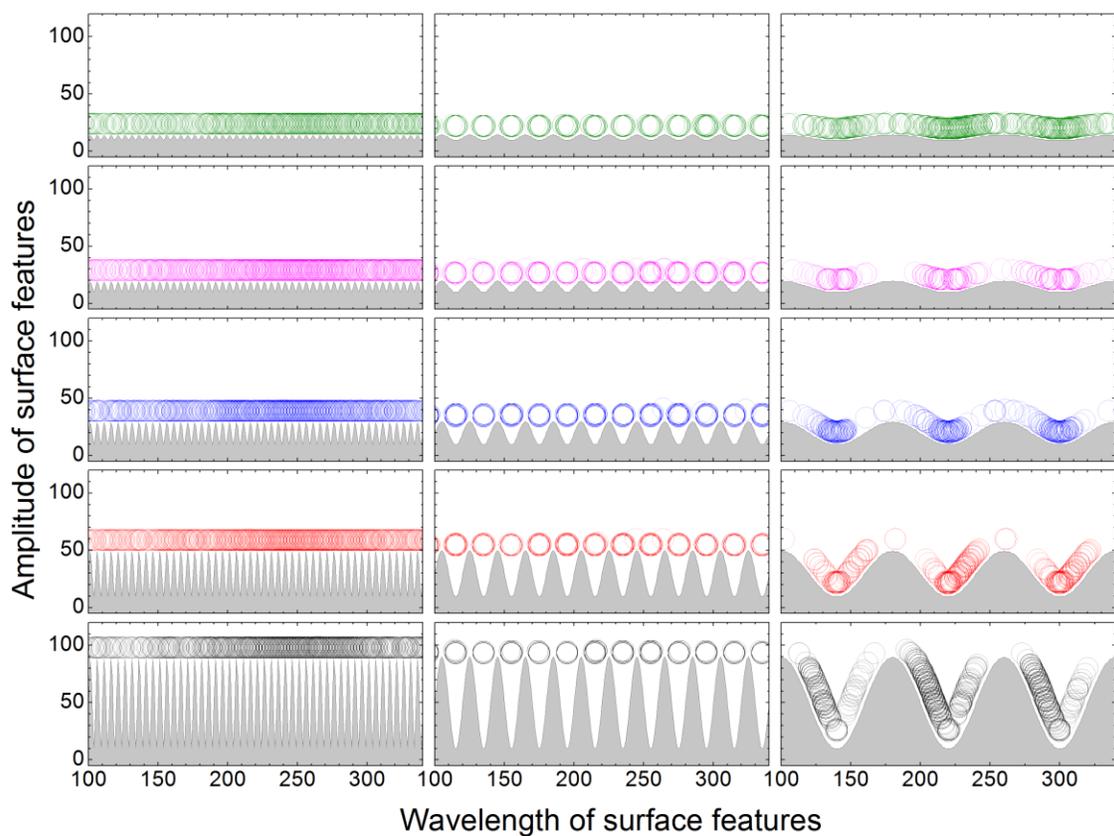


Figure 2.2. Positions of the center of mass (COM) for particles having $D=20$, $N=3$, $\sigma=0.04$ and $\epsilon=1$ kT adsorbing on substrates featuring sinusoidal corrugations featuring five different amplitudes and three different feature widths. The amplitudes are equal to (from the top to the bottom panel): 5 (green), 10 (magenta), 20 (blue), 40 (red), and 80 (black). The feature widths displayed are equal to: 5 (left column), 20 (middle column), and 80 (right column). Plotted circles represent core diameter of settled particles, polymer arms not shown.

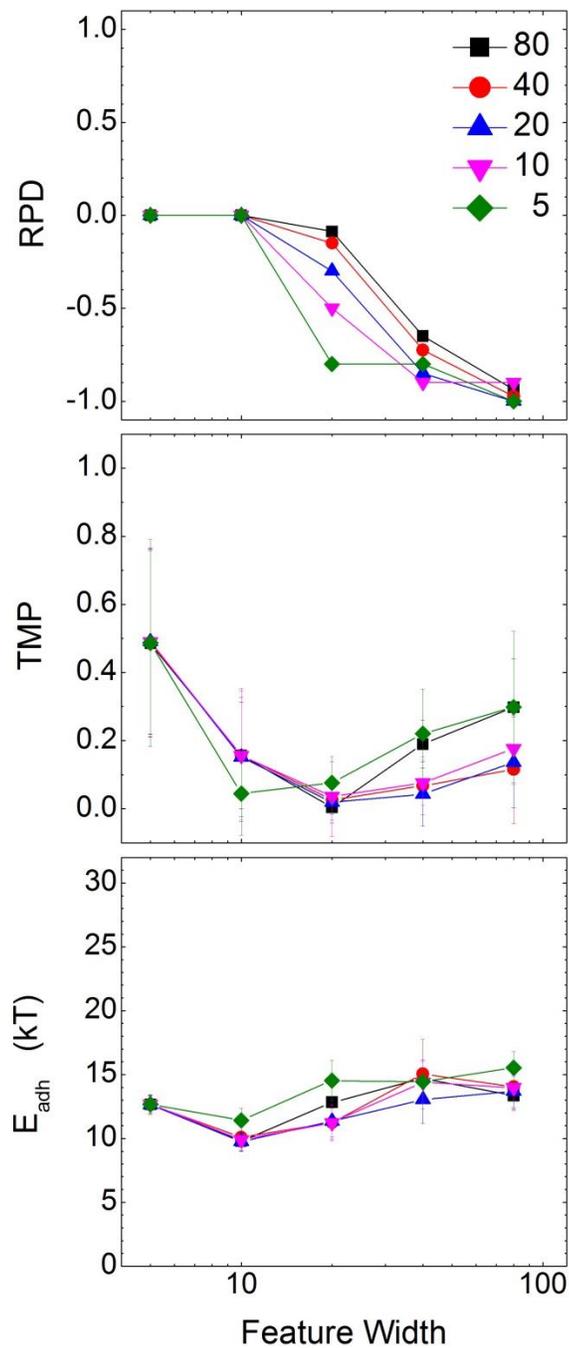


Figure 2.3. Relative penetration depth (RPD), topography match parameter (TMP), and adhesion energy (E_{adh}) as a function of the feature width for particles whose parameters are depicted in Figure 2 adsorbing onto substrates with a sinusoidal topographies having amplitudes equal to: 5 (green diamonds), 10 (magenta down-triangles), 20 (blue up-triangles), 40 (red circles), and 80 (black squares).

In **Figure 2.4** we plot the values of the RPD, TMP, and adhesion energy as a function of the feature width for various combinations of D , N , σ , and ε . For clarity we only present data pertaining to the adsorption on surfaces that possess low (10, open symbols) and high (80, closed symbols) amplitude. The left column in **Figure 2.4** denotes situations where $N=3$, $\sigma=0.04$, and $\varepsilon=1$ kT and D varies between 10 (black circles) and 40 (red squares). As expected, larger particles are excluded from penetrating deeper until the feature width of the substrate becomes very large. Also noticeable is the point where the particles first begin to penetrate the substrate features. This occurs when the substrate feature width matches approximately the diameter of the particles, implying that the penetration is highly dependent on the spatial relationship of the size of the particle *vs.* the size of the spacing between the substrate features. The critical role of the substrate feature width appears again in the TMP dependence on the substrate “wavelength”. Here the value of the TMP and its standard deviation reach a minimum at feature widths corresponding to the diameter of the particle. The values of the TMP also indicate that under these conditions the particles are both valley-centered and highly ordered in their settlement, although they are still too large to penetrate deep into the substrate.

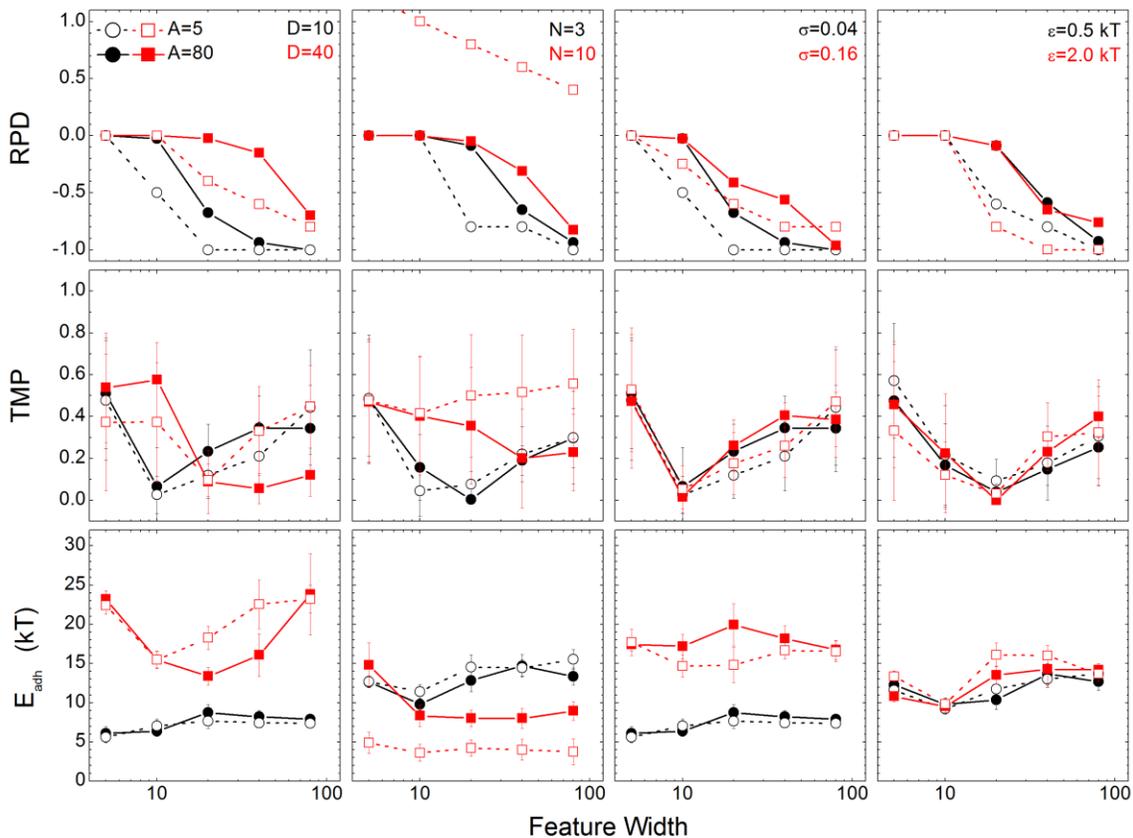


Figure 2.4. Relative penetration depth (RPD, top row), topography match parameter (TMP, middle row), and adhesion energy (E_{adh} , bottom row) as a function of the feature width for particles adsorbing onto substrates with a sinusoidal topographies having amplitudes equal to 5 (open symbols) and 80 (closed symbols). The black and red symbols represent two cases in which one system parameter was varied, *i.e.*, particle diameter (D , left column), length of polymer hair (N , second column from left), grafting density of hair (σ , second column from right), and adhesion energy (ϵ , right column).

Having discussed the effect of the particle size, we now turn to exploring the role of the length of the flexible hair on particle adsorption. In the second column from the left in **Figure 2.4** we plot RPD, TMP, and adhesion energy as a function of the feature width for

$D=20$, $\sigma=0.04$, and $\epsilon=1$ kT and N equal to 3 (black circles) and 10 (red squares). The RPD data for the short arms reveal that the particles enter the surface structure just above the diameter of the particle whereas the particles with the longer arms are sterically hindered in their penetration due to their bulky arms. The short-armed particles settle discretely on the surface based on the TMP data with high level of ordering. However, the long-armed particles “ignore” the substrate topography to a large degree and settle equally everywhere on the surface. This result implies that the substrate topography is effective in controlling particle settlement only in situations where the particles possess flexible elements whose size is much smaller than their radii; *i.e.*, substrate topographies are ineffective in controlling particle settlement in situations involving particles whose flexible arms are on the order of or longer than the radii of the settling particles.

The grafting density of the flexible arms of the particles’ surfaces also affects particle settlement on the topographically-corrugated substrates. In the second column from the right in **Figure 2.4** we present RPD, TMP, and adhesion energy as a function of the feature width for $D=10$, $N=3$, and $\epsilon=1$ kT and σ equal to 0.04 (black circles) and 0.16 (red squares). The RPD data characterize the effect of the density of flexible arms on increasing the chain stiffness as the effective radius of the particle increases causing the particles to penetrate the substrate much more gradually at high grafting density. As expected, relative to the low σ case, particles with high grafting density hairs exhibit much higher adhesion energies due to more adhesive points acting between the particle and the substrate. The TMP varies only slightly in behavior for the two cases. Also of note is the peak in the adhesion energy plot

and its standard deviation; it occurs at roughly two times the particle diameter and may be a case of the particle fitting well into the base of the valley and finding a maximal contact area.

Finally, we discuss the role of the adhesion energy on particle adsorption. In the right column in **Figure 2.4** we present RPD, TMP, and adhesion energy as a function of the feature width for $D=20$, $N=3$, and $\sigma=0.04$ and ϵ equal to 0.5 (black circles) and 2 kT (red squares). This situation is akin to changing the chemistry of the substrate or that of the adhesive ends of the flexible “hairs” attached to the particle surface. Predictably, varying ϵ does not affect the penetration data appreciably as those depend primarily on spatial factors discussed earlier. The TMP, however, is affected much more noticeably as it not only depends on spatial factors, but energetic as well. The case of $\epsilon=2$ kT exhibits tight binding of the particle to the substrate at the most favorable positions leading to lower minima in both the TMP and its standard deviation. In addition, as expected, the $\epsilon=2$ kT case leads to higher overall adhesion energies (and greater variations) relative to $\epsilon=0.5$ kT situations. This data point out that more organized settlement of particles on corrugated substrates can be achieved by increasing the attraction of the particle to the substrate surface. This finding can be beneficial in a variety of fields including particle sorting using controlled adsorption to substrates.

2.4 Conclusion

We have discussed the settlement of single particles with anchored flexible arms on substrates with periodically-corrugated topologies featuring sinusoidal shapes. We have

demonstrated that the adsorption in these situations is governed by the complex interplay between the characteristics of the substrate (*i.e.*, periodicity and amplitude) and the properties of the particles (*i.e.*, particle size, length and grafting density of the flexible spacers, and the affinity of the adsorptive end-segments of the flexible arms towards the surface). The major conclusion is that substrates featuring *periodic topographical corrugations* whose dimensions are commensurate with the sizes of the adsorbing particles may offer an avenue to *effective passive means of particle adsorption reduction*. We believe this model provides further insight to using periodic surface structures to reduce adsorption as de Nys et al. suggested with a attachment point theory [31,32]. Beyond this, we have expanded this model in a different direction towards multiple particle adsorption in another publication [39].

2.5 Acknowledgement

This work was supported by the Office of Naval Research under Grant No. N000141210642.

2.6 References

1. Efimenko, K.; Rackaitis, M.; Manias, E.; Vaziri, A.; Mahadevan, L.; Genzer, J. Nested self-similar wrinkling patterns in skins. *Nature Materials* **2005**, *4*, 293-297.
2. Wohl, C. J.; Belcher, M.A.; Chen, L.; Connell, J.W. Laser ablative patterning of copoly(imide siloxane)s generating superhydrophobic surfaces. *Langmuir* **2010**, *26*, 11469-11478.
3. Di Mundo, R.; Nardulli, M.; Milella, A.; Favia, P.; d'Agostino, R.; Gristina, R. Cell adhesion on nanotextured slippery superhydrophobic substrates. *Langmuir* **2011**, *27*, 4914-4921.
4. Zhang, Z.; Chen, S.; Jiang, S. Dual-functional biomimetic materials: Nonfouling poly(carboxybetaine) with active functional groups for protein immobilization. *Biomacromolecules*, **2006**, *7*, 3311-3315.
5. Mrksich, M. A surface chemistry approach to studying cell adhesion. *Chemical Society Reviews* **2000**, *29*, 267-273.
6. Shao, Y.; Fu, J. Integrated Micro/Nanoengineered functional biomaterials for cell mechanics and mechanobiology: A materials perspective. *Advanced Materials* **2014**, *26*, 1494-1533.
7. Tseng, P.; Di Carlo, D. Substrates with patterned extracellular matrix and subcellular stiffness gradients reveal local biomechanical responses. *Advanced Materials* **2014**, *26*, 1242-1247.
8. Yao, X.; Peng, R.; Ding, J. Cell-material interactions revealed via material techniques of surface patterning. *Advanced Materials* **2013**, *25*, 5257-5286.
9. Marino, A.; Ciofani, G.; Filippeschi, C.; Pellegrino, M.; Pellegrini, M.; Orsini, P., Pasqualleti, M.; Mattoli, V.; Mazzolai, B. Two-photon polymerization of sub-micrometric patterned surfaces: Investigation of cell-substrate interactions and improved differentiation of neuron-like cells. *ACS Applied Materials & Interfaces* **2013**, *5*, 13012-13021.
10. Sangeetha, N.M.; Blanck, C.; Nguyen T.T.T., Contal, C.; Mesini, P.J. Size-selective 2D ordering of gold nanoparticles using surface topography of self-assembled diamide template. *ACS Nano* **2012**, *6*, 8498-8507.

11. Bae, W.; Kim, H.N.; Kim, D.; Park, S.; Jeong, H.E.; Suh, K. 25th anniversary article: Scalable multiscale patterned structures inspired by nature: The role of hierarchy. *Advanced Materials* **2014**, *26*, 675-700.
12. Kolewe, M.E.; Park, H.; Gray, C.; Ye, X.; Langer, R.; Freed, L.E. 3D structural patterns in scalable, elastomeric scaffolds guide engineered tissue architecture. *Advanced Materials* **2013**, *25*, 4459-4465.
13. Agarwal, A.; Farouz, Y.; Nesmith, A.P.; Deravi, L.F.; McCain, M.L.; Parker, K.K. Micropatterning alginate substrates for in vitro cardiovascular muscle on a chip. *Advanced Functional Materials* **2013**, *23*, 3738-3746.
14. Hanske, C.; Mueller, M.B.; Bieber, V.; Tebbe, M.; Jessl, S.; Wittemann, A., Fery, A. The role of substrate wettability in nanoparticle transfer from wrinkled elastomers: Fundamentals and application toward hierarchical patterning. *Langmuir* **2012**, *28*, 16745-16750.
15. Snell, K.E.; Stephant, N.; Pansu, R.B.; Audibert, J.; Lagugne-Labarthe, F.; Ishow, E. Nanoparticle organization through photoinduced bulk mass transfer. *Langmuir* **2014**, *i*, 2926-2935.
16. Driscoll, M.K.; Sun, X.; Guven, C.; Fourkas, J.T.; Losert, W. Cellular contact guidance through dynamic sensing of nanotopography. *ACS Nano* **2014**, *8*, 3546-3555.
17. Krishnan, S.; Weinman, C.J.; Ober, C.K. Advances in polymers for anti-biofouling surfaces. *Journal of Materials Chemistry* **2008**, *18*, 3405-3413.
18. Grozea, C.M.; Walker, G.C. Approaches in designing non-toxic polymer surfaces to deter marine biofouling. *Soft Matter* **2009**, *5*, 4088-4100.
19. Chapman, R.; Ostuni, E.; Liang, M.; Meluleni, G.; Kim, E.; Yan, L., Pier, G.; Warren, H.S.; Whitesides, G.M. Polymeric thin films that resist the adsorption of proteins and the adhesion of bacteria. *Langmuir* **2001**, *17*, 1225-1233.
20. Therien-Aubin, H.; Chen, L.; Ober, C K. Fouling-resistant polymer brush coatings. *Polymer* **2011**, *52*, 5419-5425.
21. Gunkel, G.; Weinhart, M.; Becherer, T.; Haag, R.; Huck, W.T.S. Effect of polymer brush architecture on antibiofouling properties. *Biomacromolecules* **2011**, *12*, 4169-4172.
22. Dimitriou, M.D.; Zhou, Z.; Yoo, H.; Killups, K.L.; Finlay, J.A.; Cone, G.; Sundaram, H.S.; Lynd, N.A.; Barteau, K.P.; Campos, L.M.; Fischer, D.A.; Callow, M.E.; Callow, J.A.; Ober, C.K.; Hawker, C.J.; Kramer, E.J.. A general approach to controlling the

- surface composition of poly(ethylene oxide)-based block copolymers for antifouling coatings. *Langmuir* **2011**, *27*, 13762-13772.
23. Zhang, Z.; Chao, T.; Chen, S.; Jiang, S. Superlow fouling sulfobetaine and carboxybetaine polymers on glass slides. *Langmuir* **2006**, *22*, 10072-10077.
 24. Zhang, Z.; Finlay, J.A.; Wang, L.; Gao, Y.; Callow, J.A.; Callow, M.E.; Jiang, S. Polysulfobetaine-grafted surfaces as environmentally benign ultralow fouling marine coatings. *Langmuir* **2009**, *25*, 13516-13521.
 25. Li, G.; Xue, H.; Gao, C.; Zhang, F.; Jiang, S. Nonfouling polyampholytes from an ion-pair comonomer with biomimetic adhesive groups. *Macromolecules* **2010**, *43*, 14-16.
 26. Koch, K.; Bhushan, B.; Jung, Y.C.; Barthlott, W. Fabrication of artificial lotus leaves and significance of hierarchical structure for superhydrophobicity and low adhesion. *Soft Matter* **2009**, *5*, 1386-1393.
 27. Feng, L.; Li, S.; Li, Y.; Li, H.; Zhang, L.; Zhai, J., Song, Y.; Liu, B.; Kiang, L.; Zhu, D. Super-hydrophobic surfaces: From natural to artificial. *Advanced Materials* **2002**, *14*, 1857-1860.
 28. Sun, M.; Luo, C.; Xu, L.; Ji, H.; Ouyang, Q.; Yu, D., Chen, Y.. Artificial lotus leaf by nanocasting. *Langmuir* **2005**, *21*, 8978-8981.
 29. Berntsson, K.; Andreasson, H.; Jonsson, P.; Larsson, L.; Ring, K.; Petronis, S.; Gatenholm, P.. Reduction of barnacle recruitment on micro-textured surfaces: Analysis of effective topographic characteristics and evaluation of skin friction. *Biofouling* **2000**, *16*, 245-261.
 30. Efimenko, K.; Finlay, J.; Callow, M.E.; Callow, J.A.; Genzer, J. Development and testing of hierarchically wrinkled coatings for marine antifouling. *ACS Applied Materials & Interfaces* **2009**, *1*, 1031-1040.
 31. Aldred, N.; Scardino, A.; Cavaco, A.; de Nys, R.; & Clare, A.S. Attachment strength is a key factor in the selection of surfaces by barnacle cyprids (balanus amphitrite) during settlement. *Biofouling* **2010**, *26*, 287-299.
 32. Scardino, A.; Harvey, E.; De Nys, R. Testing attachment point theory: Diatom attachment on microtextured polyimide biomimics. *Biofouling* **2006**, *22*, 55-60.
 33. Vasudevan, R.; Kennedy, A.J.; Merritt, M.; Crocker, F H.; Baney, R.H. Microscale patterned surfaces reduce bacterial fouling-microscopic and theoretical analysis. *Colloids and Surfaces B: Biointerfaces* **2014**, *117*, 225-232.

34. Perera-Costa, D.; Bruque, J M.; Gonzalez-Martin, M.; Gomez-Garcia, A.C.; Vadillo-Rodriguez, V. Studying the influence of surface topography on bacterial adhesion using spatially organized microtopographic surface patterns. *Langmuir* **2014**, *30*, 4633-4641.
35. Grinthal, A.; Aizenberg, J. Mobile interfaces: Liquids as a perfect structural material for multifunctional, antifouling surfaces. *Chemistry of Materials* **2014**, *26*, 698-708.
36. Guegan, C.; Garderes, J.; Le Pennec, G.; Gaillard, F.; Fay, F.; Linossier, I., Henry, J.M.; Bellon Fontaine, M.N.; Vallee Rehal, K. Alteration of bacterial adhesion induced by the substrate stiffness. *Colloids and Surfaces B: Biointerfaces* **2014**, *114*, 193-200.
37. Decker, J.T.; Kirschner, C.M.; Long, C.J.; Finlay, J.A.; Callow, M.E.; Callow, J.A., Brennan, A.B. Engineered antifouling microtopographies: An energetic model that predicts cell attachment. *Langmuir* **2013**, *29*, 13023-13030.
38. Carmesin, I.; Kremer, K. The bond fluctuation method - a new effective algorithm for the dynamics of polymers in all spatial dimensions. *Macromolecules* **1988**, *21*, 2819-2823.
39. Schoch, P. K.; Genzer, J. Adsorption of Multiple Spherical Particles onto Sinusoidally Corrugated Substrates. *Langmuir* **2014**, *30*, 9407-9417.

Supplemental Information

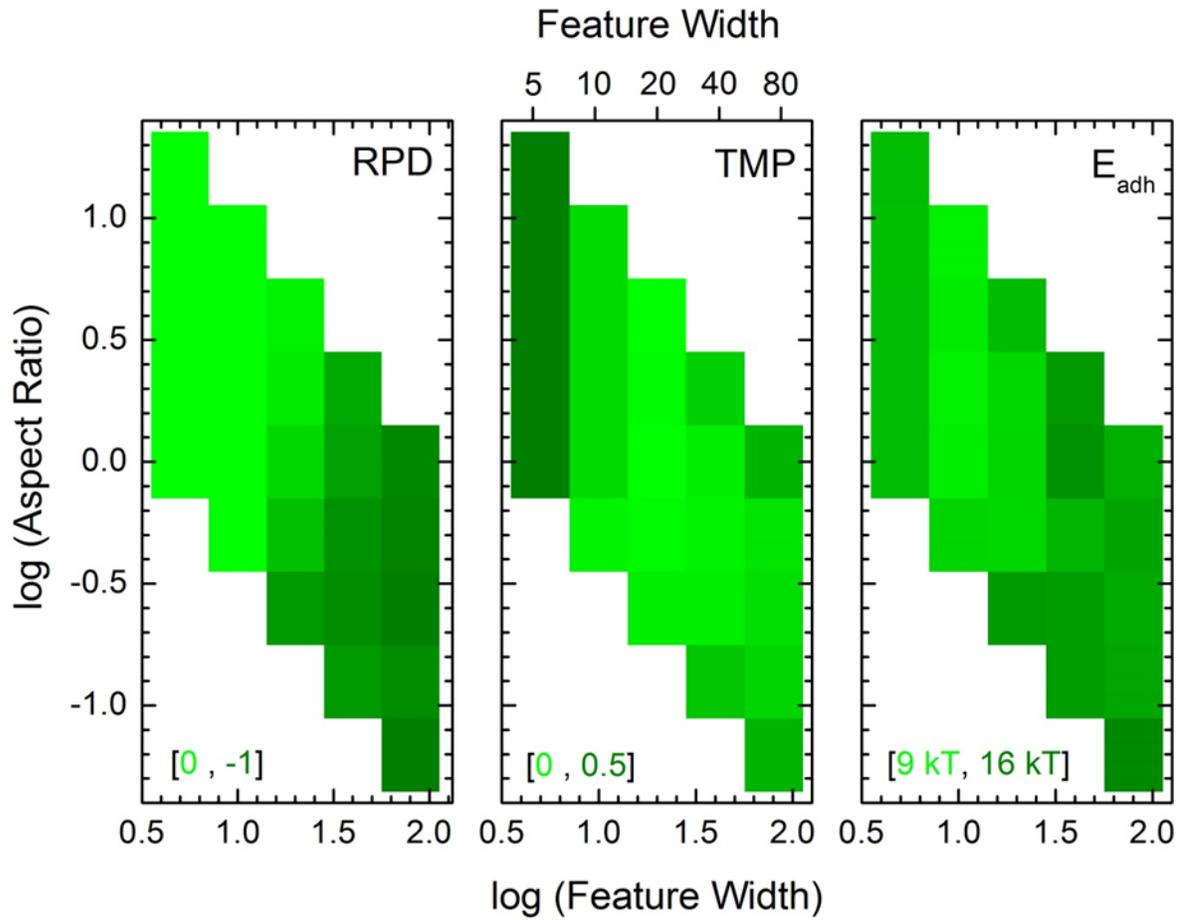


Figure 2.S1. Log(aspect ratio) versus Log(feature width) for adhesion energy of $D=20$, $N=3$, $\sigma=0.04$ and $\varepsilon=1$ kT among RPD, TMP and adhesion energy measurements. Colored shades of green where lightest represents minimal values and darkest indicates maximal values of the respective measurement. In the regions where both RPD and TMP are light green (minimized) we see lowest adhesion energies.

Appendix

We provide details pertaining to the computer simulation setup, initialization, operation and optimization. We chose a 3D lattice Monte Carlo simulation scheme following the bond fluctuation model (BFM) for our system of polymer-coated spheres adhesively interacting with sinusoidally-corrugated substrates. The BFM dictates a set of possible bond vectors and prevents overlap of polymer coarse-grained elements in a 2D or 3D lattice. Initializing the system involves first the generation of a solid, inelastic substrate defined by $y=A*\sin(B*x)$ such that A determines the amplitude of the substrate while B determines the periodicity. A sphere is generated at a set, identical location (X, Y) with fixed height (Z) above the substrate. The sphere is modified with surface bound polymer chains, which have optimized equidistant spacing, based on the surface grafting density parameter (σ), length defined by chain element parameter (N). The polymer chains are generated orthogonal to the surface; it thus needs time to equilibrate and are given $1000*N$ Monte Carlo steps to equilibrate in the lattice. Once completed the polymer coated sphere is ready to move in the simulation box. Polymer, particle core and substrate are not allowed to overlap at any lattice site. There is a balance between movement of the entire particle (sphere and polymer together) and independent movement of the coarse-grained polymer chain elements. This balance is struck in optimization by achieving effective maximization of adhesion energy in long Monte Carlo step simulations wherein the particles are able to achieve adhesion energy maxima but maintain ability to release from local energy maxima. The move set probabilities are such that there is $N/N+1$ chance of attempted polymer chain move and a $1/N+1$ chance of

attempted entire sphere move. Moves are accepted based on periodic boundary conditions in x and y as well as rules of the BFM. This particle moves around in 3D space until it contacts the surface. Contact occurs when a substrate lattice site is adjacent to an adhesive polymer lattice site. Each attractive interaction is pair-wise and is a square-well potential with a value of ϵkT and is calculated directly based on the distance between surface lattice sites (X, Y, Z) and polymer lattice sites (x, y, z). Such that:

$$r = \sqrt{(X_{substrate} - x_{polymer})^2 + (Y_{substrate} - y_{polymer})^2 + (Z_{substrate} - z_{polymer})^2}$$

$$\begin{cases} r \leq \sqrt{10} \rightarrow \epsilon_{adhesion} = \epsilon kT \\ r > \sqrt{10} \rightarrow \epsilon_{adhesion} = 0 kT \end{cases}$$

At this point moves become restricted to acceptance based on increasing adhesion energy of the system or on passing the Metropolis algorithm where the probability of acceptance of the move is proportional to $e^{\Delta E/kT}$, where ΔE is defined as $E_{system,i} - E_{system,i-1}$. This makes large changes to adhesion energy unlikely yet still allows particles to gradually probe the substrate for optimal adhesion locations. An additional move is introduced to the algorithm when the particle is in contact with the substrate. We call this a "stuck" move in which the hard core of the particle attempts to move but some of the surface-bound polymer is adhered to the surface. This move checks the possibility of the core of the particle to move while the adhered polymer remains in contact with the surface. Particles continue to probe the surface for a predefined number of Monte Carlo steps with their X,Y,Z positions, adhesion energy

and highest adhesion energy location tracked. The simulation ends after the desired number of trials (typically 1000 trials) have occurred.

CHAPTER 3

Adsorption of Multiple Spherical Particles onto Sinusoidally-Corrugated Substrates

Published peer-reviewed article:

Schoch, P. K.; Genzer, J. Adsorption of Multiple Spherical Particles onto Sinusoidally Corrugated Substrates. *Langmuir* **2014**, 30, 9407-9417.

Adsorption of Multiple Spherical Particles onto Sinusoidally-Corrugated Substrates

Phillip K. Schoch and Jan Genzer*

Department of Chemical and Biomolecular Engineering, North Carolina State University,
Raleigh, North Carolina

Abstract

We utilize a Monte Carlo simulation scheme based on the bond fluctuation model to simulate settlement of adhesive particles onto sinusoidally corrugated substrates. The particles are composed of a hard inner core with either an effective potential shell or a “soft” adhesive shell made of flexible arms attached to the particle surface. These chains adhere via either the effective potential shell or the sticky chain ends to surface via pair wise non-specific interactions. This simulation model allows for multiple particles to settle onto each tested substrate to elucidate the behavior of the collective adhesive layer featuring multi-particle assembly. Particles move within a 3D lattice space and settle on the substrate due to attractive particle/substrate interactions. Once a single particle adheres to the substrate, a new particle is introduced into the lattice to begin a new settlement. Through this multi-particle settlement mode, we explore the interplay among the characteristics of the particles (*i.e.*, size, interaction shell) and the substrates (*i.e.*, wavelength and periodicity) as well as inter-particle interactions. We report that the adhesion of particles with an effective interaction shell to the substrates is reduced dramatically when the particle size is larger than

the feature width of the periodic substrate. The settlement of particles with flexible hair on the sinusoidally corrugated substrates is more complex. Specifically, the presence of flexible polymeric hairs makes the particle settlement more likely to occur on nearly all substrates studied irrespective of the characteristics of the substrate.

3.1 Introduction

The settlement and organization of particles with adhesive surface groups onto material substrates is important to many fields of science and technology ranging from biofouling to particle sorting [1-16]. In this work, we focus on comprehending the adsorption of multiple spherical particles onto topographically-corrugated substrates featuring sinusoidal patterns. The particles studied here interact with the substrate via either an effective field or surface-grafted polymer arms featuring “sticky” end-groups. For the case of effective interaction field, we also address the interplay between the particle/substrate vs. particle/particle interactions. Such systems are particularly relevant to the adsorption of bacteria and other small biological organisms (*i.e.*, cyprids or zoospores) that interact not only with the substrate but also with one another when settled on surfaces (*i.e.*, they may form biofilm layers). This work aims to understand the role periodic substrate topography plays in governing the adhesion of fouling particles. While there are areas that seek to promote adhesion of particle-like adsorbates (*i.e.*, cell adsorption or particle sorters), in many fields, specifically in biofouling, most efforts have aimed at reducing the adsorption of foulers via chemical methods [17-21]. For example, ethylene glycol [17,18,22] or some charge-bearing surfaces [23,24,25] are capable to minimizing (at least temporarily) bioadsorption on material substrates. Utilizing substrates with engineered surface topographies provides an alternative means towards enhancing the resistance of materials surfaces for fouling by controlling the number of interaction points between the “foulant” and the adsorbing surface. Nature provides ample inspiration for controlling the extent and

strength of adsorption on nano- and micro-structured substrates. One of the most notoriously known examples is the Lotus leaf that creates a superhydrophobic surface by minimizing the number of contacts between the adsorbing hydrophilic liquid, such as water, and the substrate through the combination of waxy hydrophobic residues on nanostructured substrate features and their spatial arrangement on the substrate [26,27,28]. The symbiosis between the chemical and topographical properties of the Lotus leaf endows it low adhesiveness and self-cleaning characteristics [26]. Several studies have explored experimentally the application of textured surfaces in preventing biological adhesion. Examples include the Sharklet patterns [29], hierarchical wrinkles with multiple dimensions [1,30], corrugated periodic structured substrates [18,25,29,31-35] or substrates with random topographical features. In spite of these efforts, very little is understood about the types of topographical morphologies and their dimensions that are best suited to reduce biofouling. Some studies have alluded to contact point theory [29,31,32,36-38] and investigated sinusoidal topographies with promising results; yet those studies did not develop a substantial theoretical basis for predicting fouling behavior.

Given the large set of system parameters governing the adsorption of particles on topographically-corrugated surfaces, comprehending the role of each individual parameter as well as their mutual interplay is not straightforward. One way to gain more insight into this phenomenon is to develop a predictive computational model that would facilitate systematic variation of the individual parameters and narrow down the vast parameter set that would eventually be studied in experiment. We have developed a Monte Carlo computer simulation scheme to model the adsorption of particles interacting with surfaces featuring sinusoidally-

corrugated topographies. In our model, the fouling particles are simulated as hard core species that exhibit either an implicit interaction field or an explicit set of "sticky" surface-grafted polymer arms that interact with the underling substrate. We modify the frequency and amplitude of the substrates and study their effects on the adsorption of particles with variable particle diameter. In the implicit particle model, we also vary the particle adhesion to the substrate as well as inter-particle interactions. In the explicit adsorption particle model, we explore the effects of the grafting density of adhesive hairs, length of hairs, number of adhesive hairs per unit area, and energy per polymer coarse-grained element-to-surface contact.

3.2 Computer Model and Data Analysis

Hard Sphere Particles (Implicit Interaction Shell)

First, we employ a Monte Carlo simulation scheme to model the behavior of adhesive hard sphere particles on substrates featuring sinusoidal profiles defined by their amplitude and frequency/wavelength. In this work, we refer to the frequency and wavelength as surface feature width and amplitude as feature height, respectively. The spherical particles interact with the corrugated substrates via non-specific interactions in an effective interaction shell around the particle. Adhesion energies are counted by summing the number of surface lattice points within the effective interaction shell. These particles are allowed to perform one move per MC step (MCS) in one principle direction (*i.e.*, $\pm x$; $\pm y$; and $\pm z$) within a lattice. After each MCS the adhesion energy is calculated and recorded as well as the spatial location of said particle. System testing was performed at high number of MC steps to ensure particles

were able to reach multiple maxima in their allotted settlement time. After this time, the location, where the particle achieves its highest adhesion energy, is considered as its settled location on the substrate. Particles are inserted onto the lattice sequentially, meaning only one particle moves at any time and all settled particles remain stationary. The simulation is complete once all available substrate area is taken by the settled particles and no new particles can settle on the surface.

“Soft” Sphere Particles (Explicit Polymer Layer)

In addition, we employ a MC simulation scheme to model the behavior of adhesive hard sphere particles covered with explicit polymeric “hairs” interacting with the substrates through their sticky ends. The particle movements are regulated by the bond fluctuation model (BFM) [39]. The system features a cubic lattice comprising 160 x 160 x 200 lattice cells versus the 500 x 500 x 200 lattice cells used in our other work [40]. Larger lattices with more particles were tested but did not show significant deviation in results, thus for the sake of computational time smaller lattices were used. BFM dictates a set of 108 possible bond vectors allowed in a cubic lattice as shown by the set of moves: P(2,0,0) U P(2,1,0) U P(2,1,1) U P(2,2,1) U P(3,0,0) U P(3,1,0) and their permutations and sign inversions of such [39]. All moves in the BFM are selected randomly and attempted with favorable moves tending towards an increase in adhesion energy. To strike a balance between the entire particle moving and each element of the surface-grafted polymer elements moving on the lattice, we operate each on different time scales. In this simulation, we use MCS as “time”. The set of possible moves in this system consist of coarse-grained polymer chain moves and

movement of the entire particle. Polymer chains move on a faster time scale than that of the moves of the overall particle thus the move probabilities are balanced as such. There is no preferential direction imposed on the movement of the particles, *i.e.*, no gravitational or other external forces affect the motion of particles as they move within the lattice. Changes to adhesion energy of the system are handled by the Metropolis MC decision algorithm where any move that increases the interaction energy is accepted and any move that causes a decrease in interaction energy is allowed to take place with the probability proportional to $e^{\Delta E/kT}$, where ΔE is $E_{\text{system},i} - E_{\text{system},i-1}$ (Note the difference in sign convention as this deals with energy of adhesion which we treat as a positive quantity thus the algorithm seeks to maximize energy of the system). This simulation scheme maintains randomness in the system and allows each particle to escape local energy minima. Each particle trial is given an arbitrary amount of time to first equilibrate the flexible arms anchored to the particle surface before the particle itself is allowed to move as a whole; we use 1,000 MCS per polymer coarse-grained element. After being inserted into the lattice, each particle moves freely in any direction and the simulation ends after a predetermined set of MCSs. The number of MCS is adjusted based on long time energy equilibrations such that each particle reaches several energy maxima; this results in $\approx 10,000$ MCS per chain element in these simulations. The particle is considered settled at whichever location on the substrate when it achieves its highest adhesion energy throughout its entire simulation time. The particles settled on the substrate remain stationary. The only moving particle is the newest particle searching for a location on the substrate to settle on. We do not increase the allotted MCS for new particles because the total number of MCS was equilibrated such that a single

particle has plenty of time to explore a large area and reach several maxima thus given reasonable time that all particles must adhere to. The simulation ends once ten consecutive particle trials have failed to attach to the surface. We note that in our model, a particle is considered to be adhered to the substrate if it is in a direct contact with the substrate. Thus, in determining the strength of particle adhesion, we do not account for particles in multilayer assemblies that are not attached directly to the substrate. In simulating multiparticle settlement through adsorption of individual particles, we maximize the adhesion energy between each particle and the substrate and thus the overall adhesion. As will be evident from the results, the particles tend to close pack on the substrate, which supports further the approach. It would be interesting to revisit the problem and compare the results of this model to a scheme, which considers concurrent motion of all particles. This, however, is outside the scope of the current work.

Figure 3.1 provides the layout of the simulation set up and defines the parameters of the corrugated substrate and the particles employed in the simulation. Specifically, the substrates comprise sinusoidal topographies with adjustable amplitude and wavelength, referred to later as feature height and feature width, respectively. Data discussed in this paper include a set of three feature heights and six feature widths, which combined create 18 unique surfaces for each set of particle conditions tested. The explicit particles are defined by their core diameter (D), number of repeat segments in the anchor arms (N), grafting density of arms, *i.e.*, the number of arms per unit area, on the particle surface (σ), and the interaction potential acting between the last two adhesive segments of the flexible “hair” and the surface (ϵ). In the implicit particle simulation, we vary the particle/particle interaction

energies. During the MC simulation, we track positional data of all anchored arms and the center of mass of the particle as well as the current adhesion energy of the system. Each data point presented is the result of three identical simulation sets.

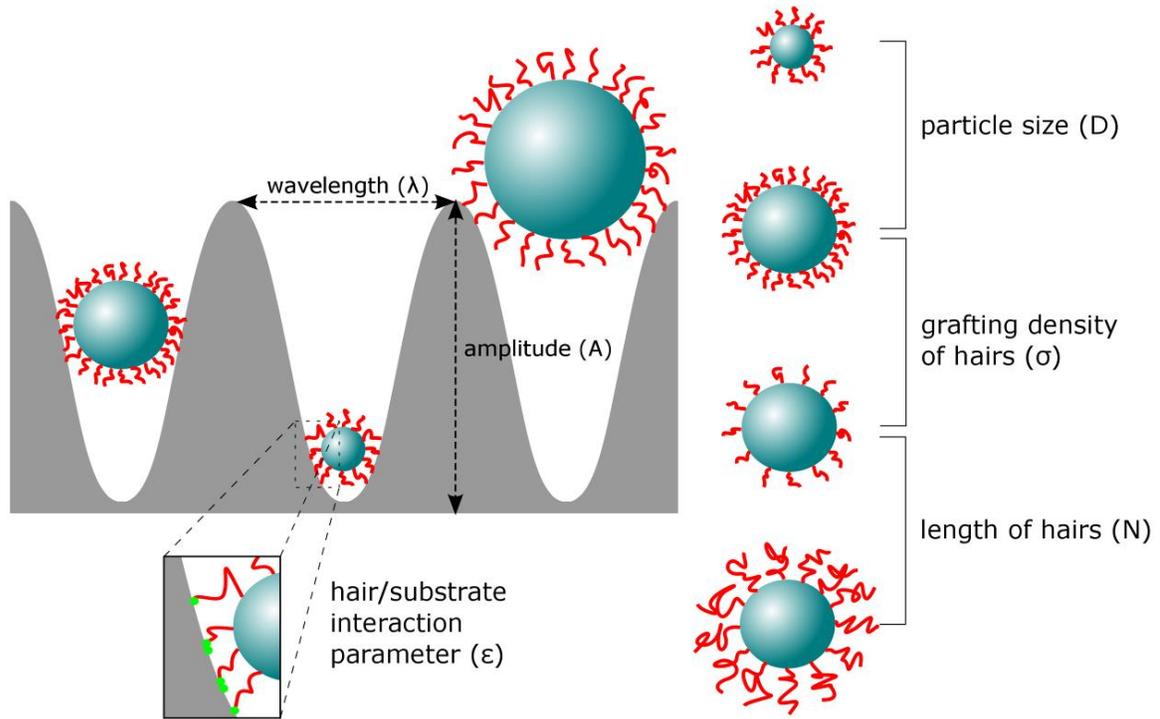


Figure 3.1. Simulation setups and particle parameters including particle size (D), grafting density of hairs (σ), length of hairs (N) and the hair/substrate interaction parameter (ϵ)

3.3 Results and Discussion

3.3.1 Hard Sphere Particles

Figure 3.2 depicts examples of hard-core particles ($D=20$) settling on substrates comprising four different feature heights (A) and six different feature widths (λ). The particles experience an effective interaction shell potential with the substrate but no particle/particle interactions. Particles settling on substrates with large feature widths cover the entire available substrate relatively uniformly. Decreasing λ lowers the available surface area on the substrate onto which the particle can settle. In particular, for $\lambda=40$ and 20 the particles are blocked completely from entering the valleys of the substrates; this effect gets even more exaggerated with increasing A . At $\lambda=20$, the feature width matches the particle size; the particles assume well-defined positions on the substrate that are dictated by the substrate features (*i.e.*, A and λ). This trend continues also for substrates with $\lambda < D$. For $\lambda \ll D$, a case not studied here in detail because of finite lattice size effects, one would expect that the particles would lose completely the memory of the substrate features and would settle relatively randomly on the substrate.

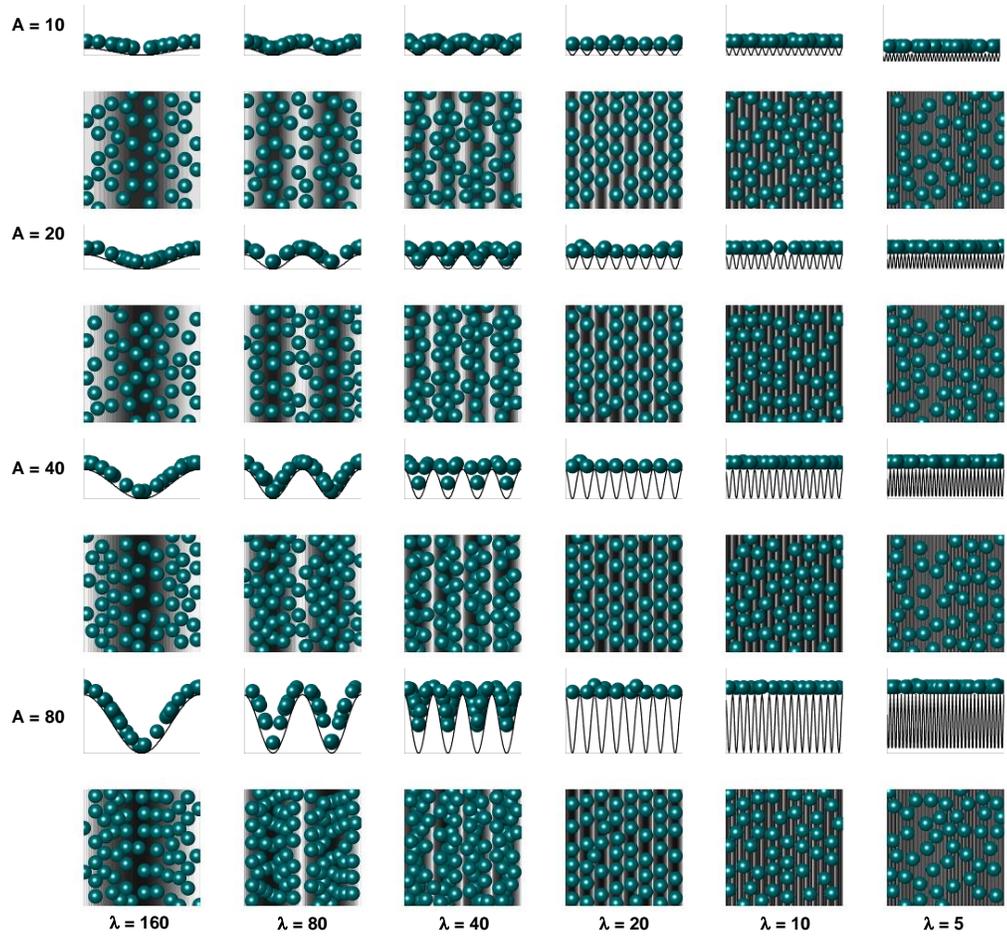


Figure 3.2. Positions of hard sphere particles ($D=20$) on sinusoidally corrugated substrates with variable amplitude (A) and variable feature width (λ). Amplitude decreases moving down while feature width decreases moving right. Core of particles shown in blue-green, higher substrate features are lighter and lower surface features are darker.

In **Figure 3.3** we plot the adhesion energy of particles with $D=20$ with the effective interaction shell settling on surfaces featuring four different values of A and six different values of λ . The adhesion energy per particle relative to that for a flat substrate is plotted for each data set as a function of the average particle counter, *i.e.*, the number of particles

settling on each substrate. Regardless of the substrate feature width and feature height, we detect that particles arriving to the substrate in early stages of the adsorption process experience higher adsorption energy relative to particles that arrive to the substrate at later times. For $\lambda \gg D$ the adhesion energy decreases continuously until a certain particle number threshold indicating the point at which the particles saturate the substrate and can no longer find a site to which they can adsorb. For $\lambda \sim D$ and $\lambda \ll D$, the adhesion energy is relatively constant in the initial stages and reaches the same threshold mentioned above. In addition, we notice that while for $\lambda \gg D$ the adsorption is governed primarily by λ (in the latter stages of adsorption), the adsorption of particles whose diameter is comparable to λ is governed by A (in the initial stages of adsorption). Adsorption in the $\lambda \ll D$ regime is independent of A and λ . The data in **Figure 3.3** confirm the trends we discussed earlier with regard to **Figure 3.2**.

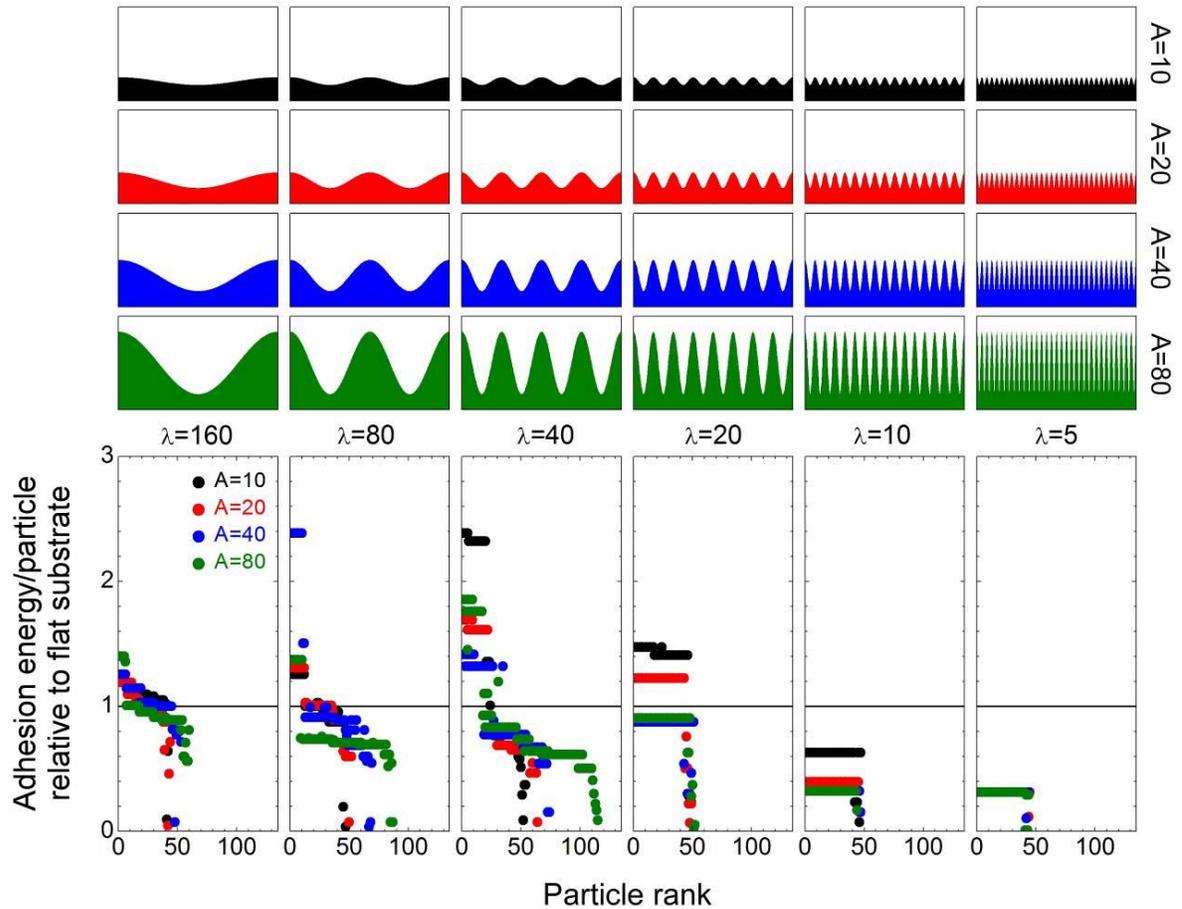


Figure 3.3. Adhesion energy per particle for hard sphere particles adsorbing onto sinusoidally-corrugated substrates. The adhesion energy has been normalized relative to adsorption of the same particles on flat substrates. The data are plotted for surfaces with various values of substrate feature width (λ) and feature height (A). The particle diameter is $D=20$.

The total adsorption energy of particles on substrates can be obtained by integrating the respective curves in **Figure 3.3**. In **Figure 3.4a**, we plot the total adhesion energy on corrugated substrate relative to adhesion on a flat substrate as a function of the feature width scaled in terms of the particle diameter for substrates with a variable A and λ . For $\lambda/D \gg 1$

the adhesion is comparable to that on flat substrates, as expected. Decreasing λ leads to higher adsorption energies of the particles because of increased surface area on the substrate, which results ultimately in higher particle accumulation on the substrate and higher total adhesion energy. When λ approaches the particle size, the particles are excluded from penetrating the substrate topography, which results in smaller particle settlement and ultimately lower overall adhesion energy. For $\lambda < D$ the particles are not able to penetrate efficiently the valleys of the substrate features; yet, the memory of the substrate is not lost completely because even a very small particle penetration into the substrate is capable of ordering the particles on the substrate by following the underlying topographical pattern. We mentioned earlier that for $\lambda \ll D$ one would expect the particles adsorb in a manner that is similar to that on flat substrates. Finite lattice size effects, however, preclude us from probing this regime effectively. In fact, lattice effects may play a role, in general, in these simulations. In order to check for consistency, we have therefore explored the settlement of a larger particle ($D=40$) on substrate with appropriately scaled feature sizes and heights. **Figure 3.4** presents results collected from two particle sizes in terms of a scaled parameter λ/D ; all data fall onto the same curve, as expected, excluding the effect of the lattice size. More insight into particle adhesion in relation to the properties of the substrate can be inferred by normalizing the adhesion energy (*cf.* **Figure 3.4a**) by the total number of particles settled on the substrate. The data in **Figure 3.4b** depict such a situation. We see that, generally, the adhesion per particle decreases with decreasing the λ/D ratio irrespective of A . For $\lambda/D \sim 1$ the adhesion energy per particle is relatively high for substrates featuring small A ; however, for $\lambda/D \ll 1$ the adhesion of particles on the surfaces decreases dramatically for all

substrate regardless of the feature height. This result suggests that adhesion of particle in systems featuring $\lambda/D \ll 1$ is lower than that on flat substrates and reveals that utilizing topographies featuring sinusoidally-corrugated substrate topographies with feature widths smaller than the particle diameter is efficient in decreasing the settlement of particles that interact with the substrate with an effective shell interactions.

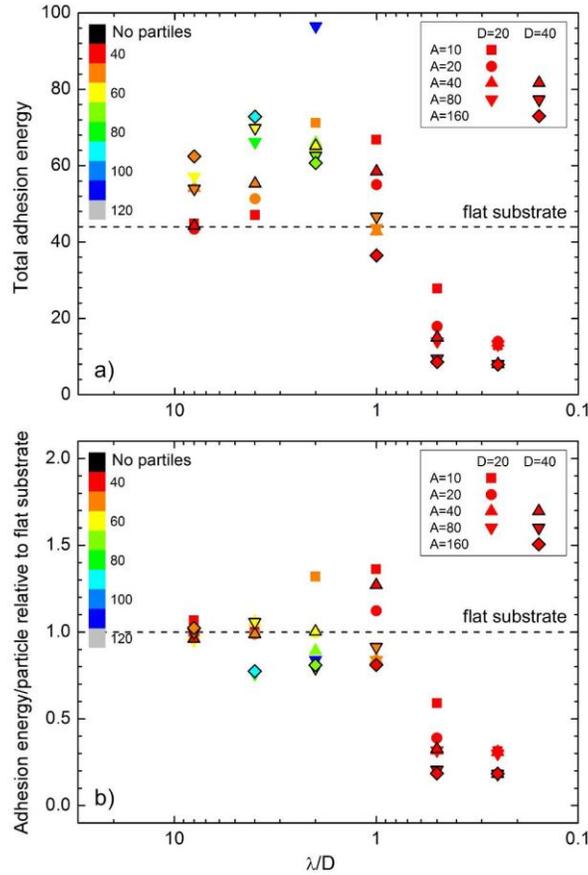


Figure 3.4. a) Total adhesion energy and b) adhesion energy per particle for hard sphere particles adsorbing onto sinusoidally-corrugated substrates as a function of feature width (λ) normalized by the particle diameter (D) for substrates featuring different amplitudes (A) and 2 different particle sized. The color scale represents the number of particles adhering to the given substrate (blue=highest, red=lowest). The particle diameter is $D=20$ and 40 (see legend).

During the MC simulations, we monitor the spatial distribution of the adsorbed particles on the various substrates for all combinations of feature widths, feature heights, and inter-particle interactions. **Figure 3.5** denotes a map of the positions of particles settling on substrates with the same A and variable λ for three strengths of particle/particle interactions. The particle/particle interactions (E_{PP}) are expressed as a fraction of the particle adhesion strength to the substrate (E_{PS}). Using such location maps, we gain information about how the spatial organization of particles on substrates is influenced by the underlying substrate topography and particle/particle interactions. The data in **Figure 3.5** demonstrate visually that the particles settle predominantly inside the valleys of the substrate topographical features that offer the largest available substrate area through which the particles can interact with the substrate. This behavior is pronounced on substrates featuring large λ . Decreasing λ of the substrate decreases the area of the substrate available for adhesion of the settling particles and, in turn, leads to lower particle settlement. When λ of the substrate protrusions becomes comparable to or smaller than D the number of particles decreases dramatically; this process is associated with dramatic reduction of the adhesion energy (*cf.* **Figure 3.4** for $E_{PP}=0$). For $E_{PP}=0$ the particles still reside above the valleys of the substrate but are more separated. Increasing the strength of the particle/particle interactions does not alter the general trend for particle location observed for $E_{PP}=0$, *i.e.*, the particles settle predominantly inside the valleys of the substrate. However, unlike the situation of for “athermal” particle/particle interactions (*i.e.*, $E_{PP}=0$), increasing E_{PP} results in additional ordering of the particles in the plane of the substrate. Specifically, increasing E_{PP} causes the particles to close-pack locally. Depending on λ , this close packing either takes place inside the surface

valleys ($\lambda \gg D$) or across the entire substrate ($\lambda \ll D$). The latter organization, which often features hexagonal close-packing, demonstrates clearly the intimate interplay between the particle organization driven solely by the substrate topography and that originating from the particle/particle interactions. Specifically, increasing the strength of the particle/particle interaction causes an increase in the tightness of packing, which enables more particles to settle on the substrate. Interestingly, the substrate least affected by this has feature spacing equal to the diameter of the particle.

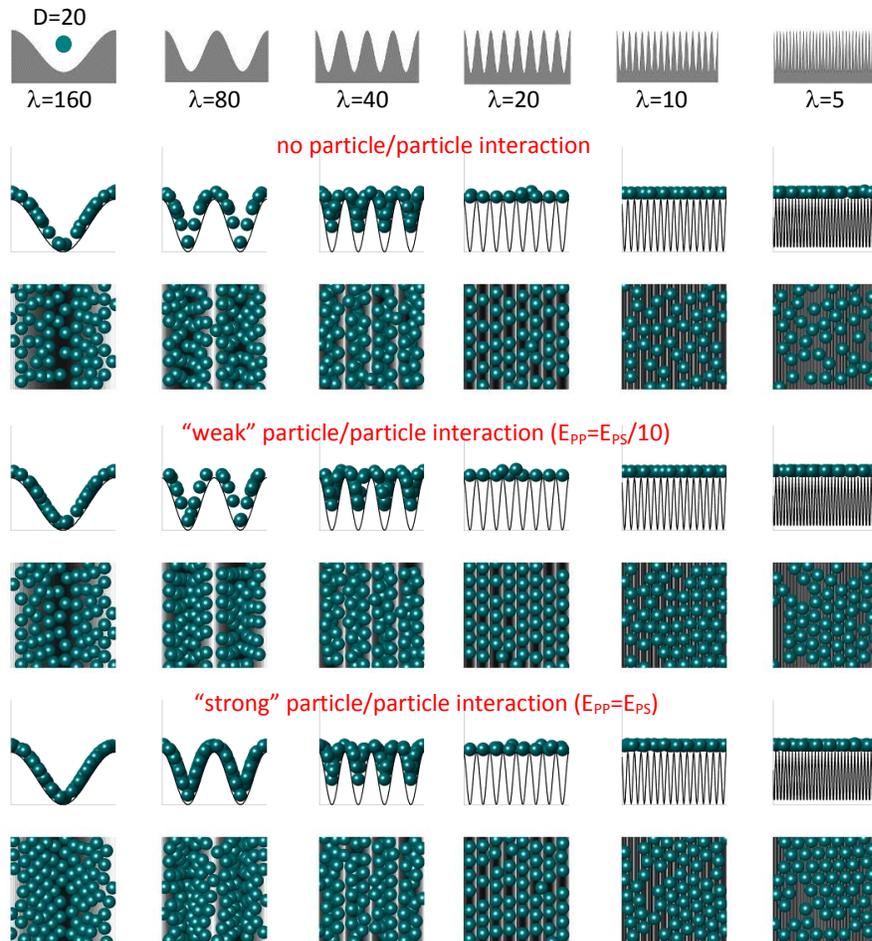


Figure 3.5. Positions of hard sphere particles ($D=20$) on sinusoidally-corrugated surfaces with constant amplitude ($A=80$) and variable feature width (λ). Inter-particle interactions increase from top to bottom. Core of particles are shown in blue, higher surface features are lighter and lower surface features are darker.

More insight into particle settlement on sinusoidally-corrugated substrates can be obtained by examining the sequence of arrival of individual particles to the substrate and the role of the particle/particle and particle/substrate adhesion on particle settlement on the surfaces. In **Figure 3.6**, we plot the order in which the particles adsorb on the substrates.

The data is depicted by color, *i.e.*, first group of particles arriving to the substrate is depicted in red, the last group of particles settling is marked in blue. The order of particle settlement depends on both the nature of the substrate and the particle/particle interactions. We start by discussing the case of $\epsilon_{pp}=0$ first (left column in **Figure 3.6**). On flat substrates, the particles settle in random fashion, as expected. On corrugated substrates, particle settlement first occurs in the valleys of the substrates, where the adhesion between the particles and the substrate is the strongest. This behavior is more pronounced for substrates with larger feature widths. Decreasing the feature width “randomizes” the particle arrival time more. In situations involving strong particle/particle interactions (right column in **Figure 3.6**), the particle settlement, even on flat substrates, depends on the strength of particle/particle interactions. Particles settle in clusters of relatively closed-packed (large ϵ) to very closed-packed (small ϵ) arrays, indicating that increasing the strength of particle/particle interactions forces the settled particles to assume positions close to the already adsorbed neighbors.

Figure 3.7 and **Figure 3.8** provide further evidence of the importance of particle/particle and particle/substrate interactions, respectively, on particle settlement. From the data in **Figure 3.7** we see the effect of increasing particle/particle interactions. The number of inter-particle contacts increases with increasing particle/particle interaction energy. For the strongest inter-particle interactions and substrates that are either flat ($\epsilon=\epsilon$) or tend to make the particles reside in a single plane ($\lambda=5$) the particles tend to adopt closed hexagonal packing (*i.e.*, 6 nearest neighbor contacts). **Figure 3.8** depicts the effect of particle/substrate interaction on particle adhesion on various substrates. There are no major trends among the various ϵ_{pp} values and various substrate features.

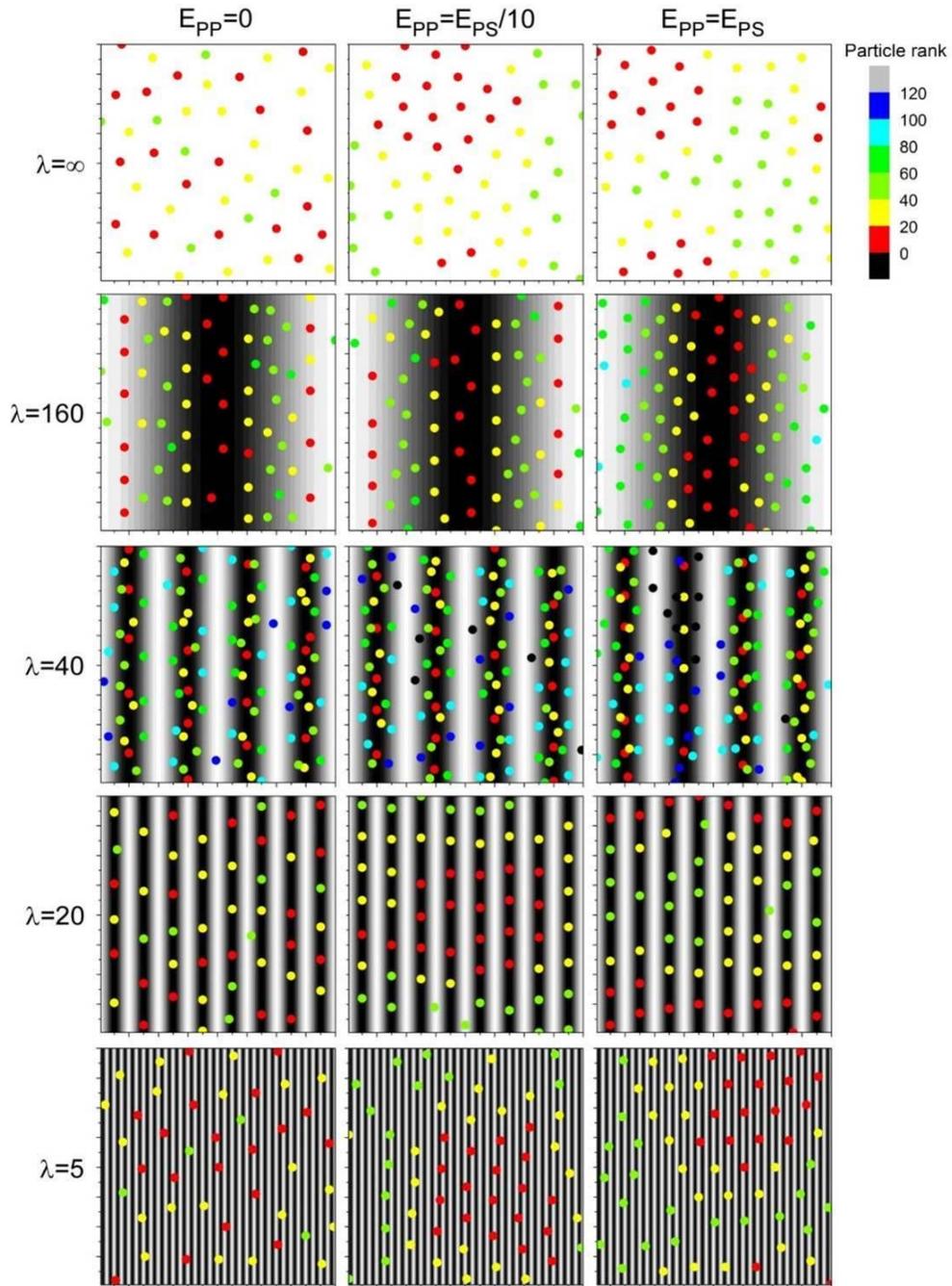


Figure 3.6. Order of arrival (red=soonest, blue=latest) of hard sphere particles ($D=20$) onto sinusoidally-corrugated surfaces with constant amplitude ($A=80$) and variable feature width (λ). Note that $\lambda=\infty$ corresponds to the flat substrate. The left, middle and right column denote data corresponding to different energy of particle/particle interactions (E_{PP}) relative to that of particle/substrate interaction (E_{PS}).

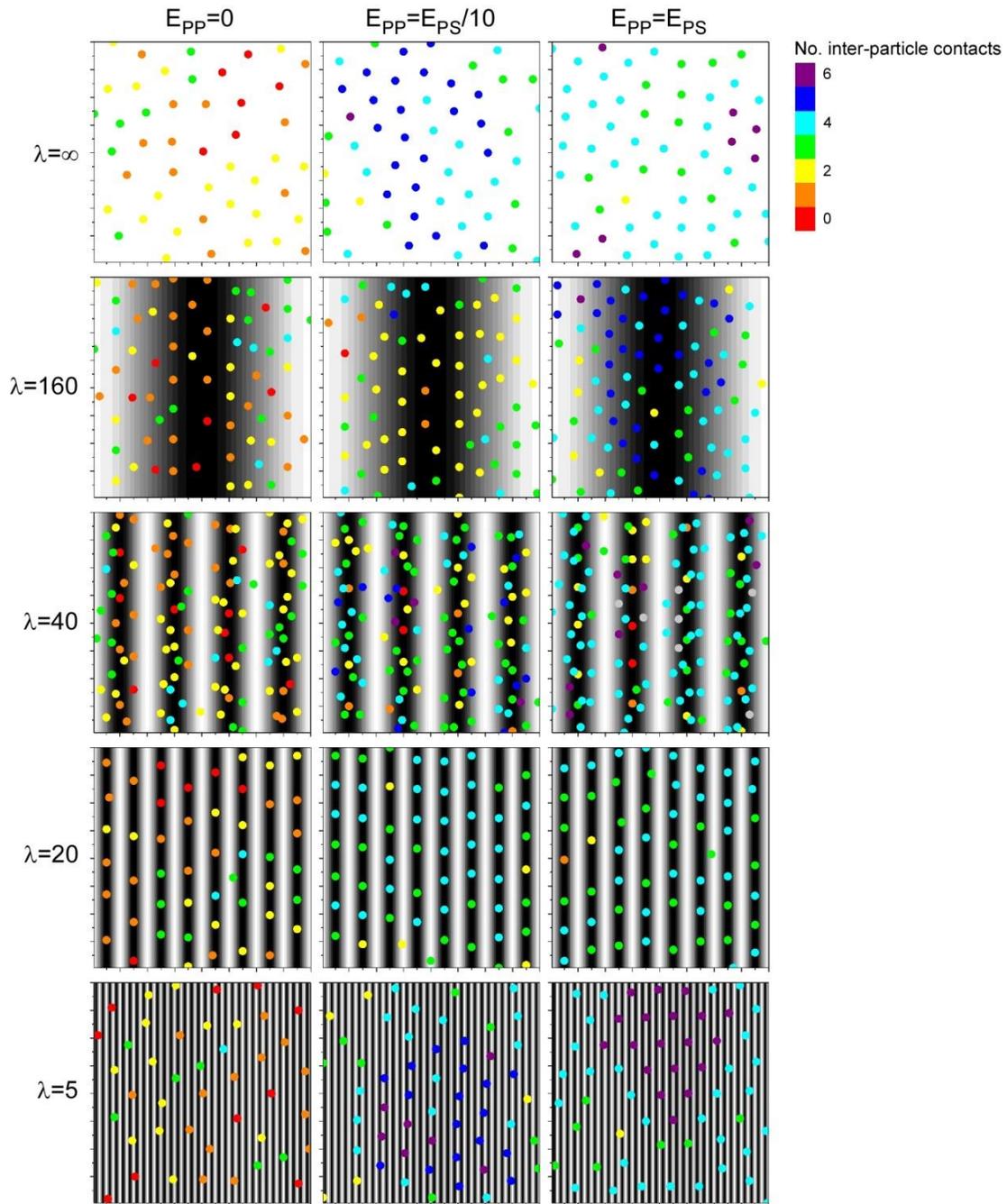


Figure 3.7. Particle/particle contacts (red=lowest, blue=highest) for hard sphere particles ($D=20$) onto sinusoidally-corrugated surfaces with constant amplitude ($A=80$) and variable feature width (λ). Note that $\lambda=\infty$ corresponds to the flat substrate. The left, middle and right column denote data corresponding to different energy of particle/particle interactions (E_{PP}) relative to that of particle/substrate interaction (E_{PS}).

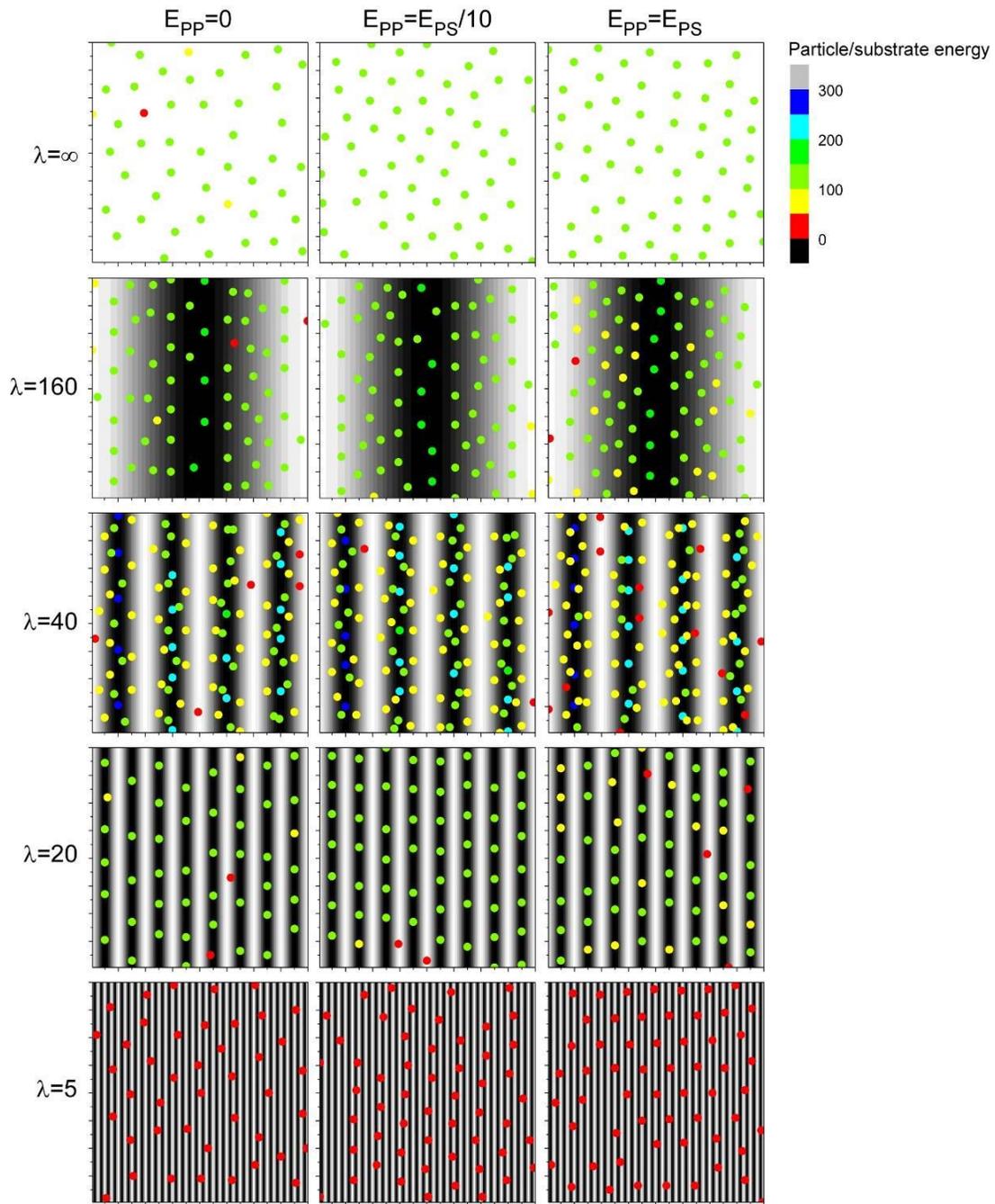


Figure 3.8. Particle/surface adhesion energy (red=lowest, blue=highest) for hard sphere particles ($D=20$) onto sinusoidally-corrugated surfaces with constant amplitude ($A=80$) and variable feature width (λ). Note that $\lambda=\infty$ corresponds to the flat substrate. The left, middle and right column denote data corresponding to different energy of particle/particle interactions (E_{PP}) relative to that of particle/substrate interaction (E_{PS}).

3.3.2 "Soft" Sphere Particles

In addition to MC simulations involving particles that exhibit implicit interactions with the substrate, we also simulated the adsorption of particles covered with explicit polymeric hairs. In **Figure 3.9** we plot the positions of particles with $D=20$ coated with polymer arms with the length (N) of 3 segments and grafting density (σ , *i.e.*, the number of polymers per unit area) equal to 0.1 on substrates with three different feature heights and six different feature widths. Just like in the case of adsorption of particles with implicit interaction shell, the particles with explicit interaction sites tend to adsorb preferentially inside the valleys of the substrate protrusions on substrates with relatively large feature width. Decreasing the feature width of the substrate reduces the available space on the substrate to which the particles can attach and, in turn, reduces the number of settled particles. The latter behavior is more pronounced for substrates whose λ becomes comparable to or smaller than the particle size (D). Here the particles are excluded from penetrating inside the substrate valleys and settle primarily on all areas of the substrate surface.

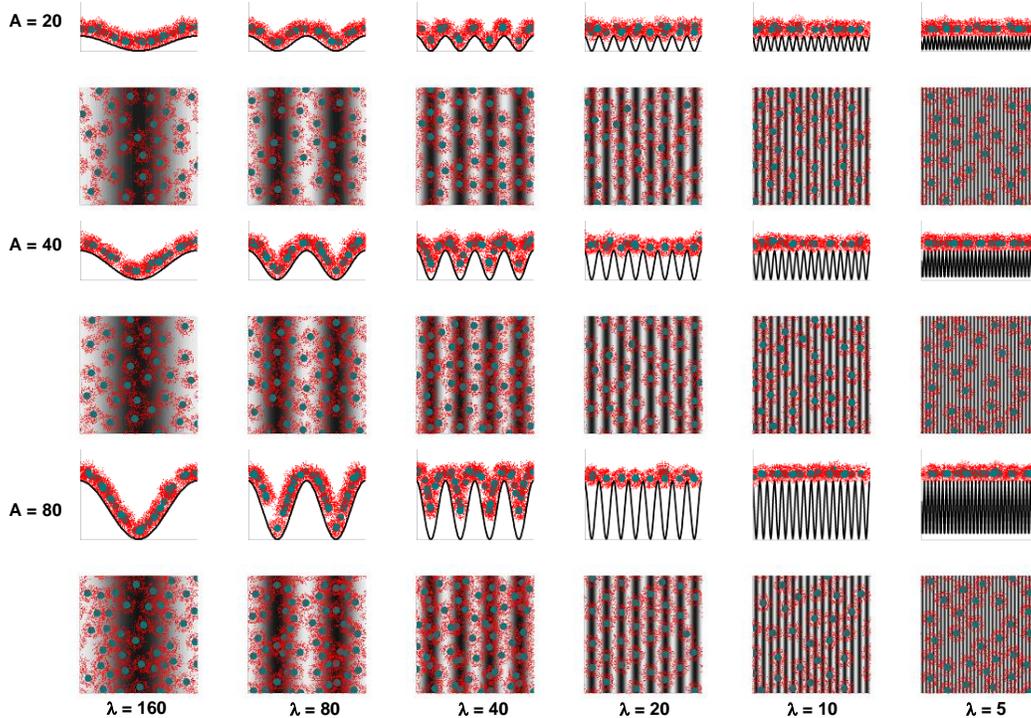


Figure 3.9. Particles covered with polymeric hair ($N=3$, $\sigma=0.04$) adsorbing onto sinusoidally-corrugated substrates with various wavelengths, *i.e.*, substrate feature widths. Substrate features decrease in amplitude going from top to bottom; the feature width (*i.e.*, wavelength) decreases going from left to right. Core of particles shown in blue, polymer "arms" shown in red, higher substrate features are depicted lighter while lower substrate features are marked darker.

In **Figure 3.10** we plot the adhesion energy of particles with $D=20$ with the explicit polymer hairs ($N=3$, $\sigma=0.04$) adsorbing onto substrates featuring three different values of A and six different values of λ . The adhesion energy per particle relative to that for a flat substrate is plotted for each data set as a function of the average particle counter, *i.e.*, the number of particles settling on each substrate. The general trends are similar to those reported earlier for the settlement of particles with an effective interaction potential with a

few exceptions. Particle adhesion increases with decreasing λ , due to increased substrate area available for particle adsorption, peaks at $\lambda \approx 2D$ and then continues to decrease with decreasing λ . The adhesion of particles on substrates with $\lambda < D$ is similar to that observed in particle settlement on flat substrates. For each feature width, the particle arriving at early stages of the adsorption process settle relatively strongly, while particles adsorbing in the late stages experience weaker adsorption to the substrate due to limited space on the substrate, to which they can settle. Unlike in the case of an effective interaction potential, where we noticed amplitude-dependent adhesion, in all cases studied here the amplitude does not seem to make a difference. In addition, the abrupt decrease in adhesion mentioned earlier for the case of particles with effective interaction potential in the late stages of adsorption is not present in here. Clearly, the presence of flexible hairs on the surface of the particles governs particle adsorption; it acts as a mediator during the adsorption process.

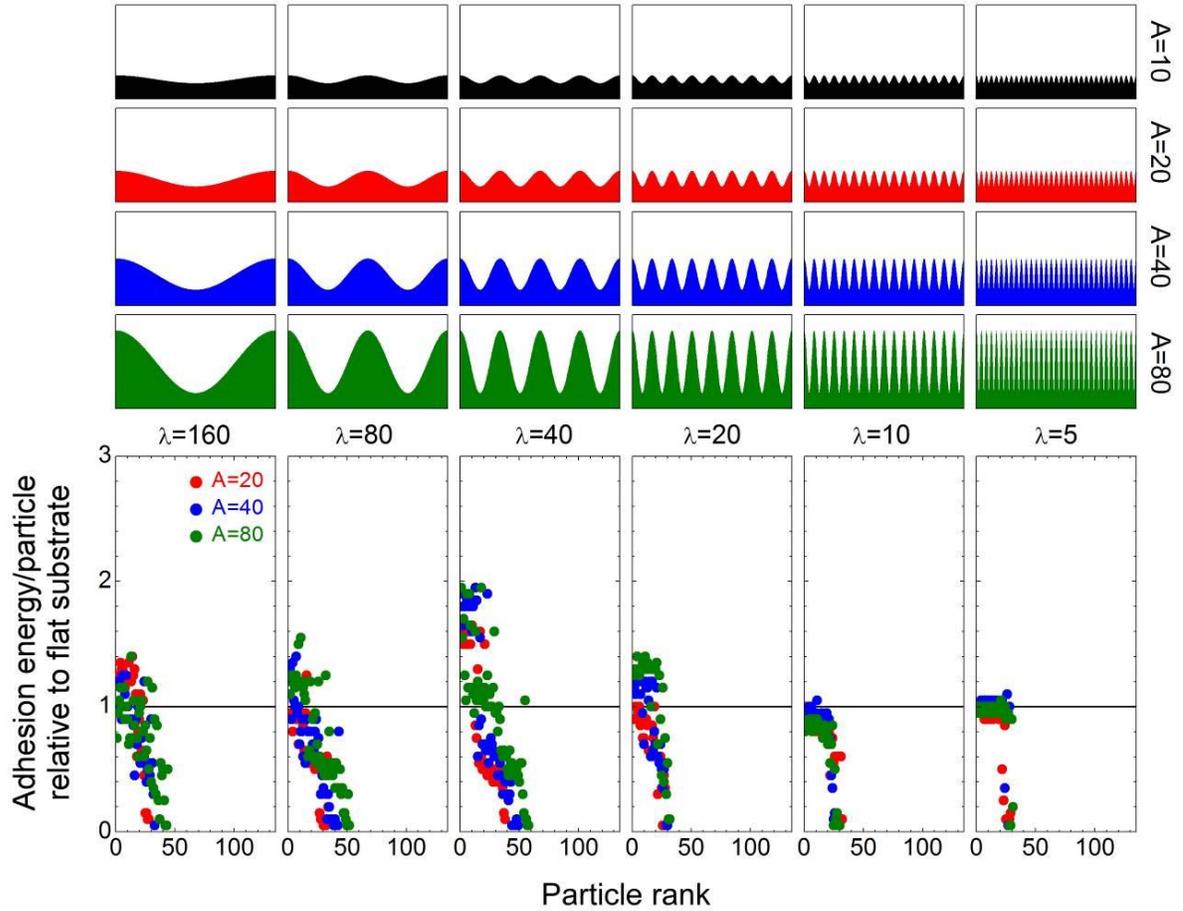


Figure 3.10. Adhesion energy per particle for particles covered with polymeric hair ($N=3$, $\sigma=0.04$) adsorbing onto sinusoidally-corrugated substrates. The adhesion energy has been normalized relative to adsorption of the same particles on flat substrates. The data are plotted for substrates with various values of feature width (λ) and feature height (A). The particle diameter is $D=20$.

A more quantitative picture of particle adhesion energy is obtained by determining the total adhesion energy of particles by integrating the areas under the respective curves in **Figure 3.10**. **Figure 3.11** depicts the total adhesion energy (a) and the adhesion energy per particle (b) as a function of λ/D . The data is colored based on the number of particles

adsorbed. The plots feature results of averaging a set of three identical simulations for each condition (A and λ of substrate). The trends in the total adhesion energy of particles are similar to those observed for the adsorption of particles with an effective potential shell. Namely, for $\lambda/D \gg 1$ the total adhesion energy is similar to that detected for particles adsorbing on flat surfaces. With decreasing λ/D the total adsorption energy and the total number of adsorbed particles increase relative to that on flat substrates as λ/D approaches unity; this increase is more pronounced for particles adsorbing on substrates with higher A . A maximum in the total adsorption energy is reached at $\lambda/D \sim 2$; further decrease in λ/D results in lower total adsorption energy of particles (relative to flat substrates). Recall that in the case of effective interaction shell potential the maximum adsorption is reached when $\lambda \sim 2D$, similarly for the present case involving the adsorption of particles with explicit polymeric hairs, the highest adsorption appears at $\lambda \sim 2D$. This is because in the latter case the particle diameter is effectively increased by the presence of the flexible hairs. The results in both cases are thus consistent and reveal that the maximum adsorption occurs when the particle size matches approximately the feature width of the substrate protrusions. By normalizing the total adsorption energy of particles to the adsorption energy per particle, the data in **Figure 3.11a** decrease are coincide with the adsorption of “hairy” particles on flat substrates (*cf.* **Figure 3.11b**). We attribute this behavior, in large part, to the “softness” of the adsorbing particles that can readily adapt to variations of the local topography of the substrate. The trends observed here are consistent with those reported for the adsorption of a single “hairy” particle [13]. Specifically, in addition to the size of the particle itself, the presence of the flexible polymeric hair anchored to the substrate of the particle determines

greatly the extent of particle adsorption on topographically corrugated substrates. Particles with long and dense flexible arms adsorb heavily on topographically-corrugated substrates; the extent of adsorption increases with increases and grafting density of the flexible adhesive arms and their length [13].

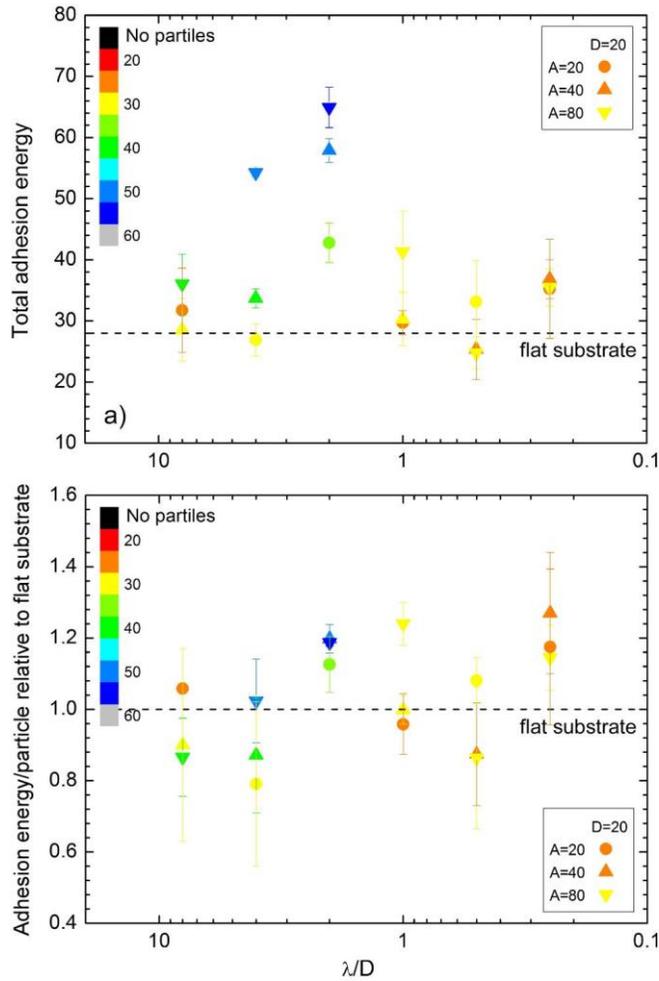


Figure 3.11. a) Total adhesion energy and b) adhesion energy per particle for particles covered with polymeric hair ($N=3$, $\sigma=0.04$) adsorbing onto sinusoidally-corrugated substrates as a function of feature width (λ) normalized by the particle diameter (D) for substrates featuring different amplitudes (A) and 2 different particle sized. The color scale represents the number of particles adhering to the given substrate (blue=highest, red= lowest). The particle diameter is $D=20$.

3.4 Conclusions

We have explored the settlement of both hard spherical particles with an effective interaction potential and those with flexible surface-anchored arms on topographically-corrugated substrates featuring sinusoidal shapes of varying feature height and feature widths. In addition to exploring the interplay between the particle size and the aforementioned attributes of the substrates, we also investigated the roles particle/particle interactions on surface organization of the settled particles. The major conclusion from this study is that the number of settled particles on the substrate depends critically on the interplay between the size and nature of the adsorbing particle and the characteristics of the underlying substrate. While substrates with relatively large substrate feature promote particle adhesion, reducing the feature width of the substrate to (or slightly below) the particle size decreases dramatically the number of particles settled and their adhesion to the substrate. We also addressed the role of inter-particle interactions on settlement on substrates. Specifically, we established that in cases involving strong particle/particle attraction, the particles aggregate on substrates in close-packed arrays. We have also documented that the structure of the interacting groups governing the adsorption of the particles to the substrate play a major role determining the adhesion of particles to underlying substrates. This is particularly important in cases involving the adsorption of particles with flexible hairs. We determined that particles with anchored flexible hairs adsorb more strongly to corrugated substrates relative to particles featuring an effective interaction potential shell. The flexibility of the

hairs and their ability to adopt a conformation that maximizes the adsorption energy is responsible for increasing the extent of adsorption of such particles relative to their counterparts featuring the effective interaction shell potential. Increasing the length and density of flexible hairs on the particle surfaces further exuberates this effect. Our simulations reveal that it is challenging to decrease the extent of adsorption of spherical particles with flexible hairs on substrates relative to adsorption on flat substrates.

3.5 Acknowledgements

This work was supported by the Office of Naval Research under Grant No. N000141210642.

3.6 References

1. Efimenko, K.; Rackaitis, M.; Manias, E.; Vaziri, A.; Mahadevan, L.; Genzer, J. Nested self-similar wrinkling patterns in skins. *Nature Materials* **2005**, *4*, 293-297.
2. Wohl, C. J.; Belcher, M.A.; Chen, L.; Connell, J.W. Laser ablative patterning of copoly(imide siloxane)s generating superhydrophobic surfaces. *Langmuir* **2010**, *26*, 11469-11478.
3. Di Mundo, R.; Nardulli, M.; Milella, A.; Favia, P.; d'Agostino, R.; Gristina, R. Cell adhesion on nanotextured slippery superhydrophobic substrates. *Langmuir* **2011**, *27*, 4914-4921.
4. Zhang, Z.; Chen, S.; Jiang, S. Dual-functional biomimetic materials: Nonfouling poly(carboxybetaine) with active functional groups for protein immobilization. *Biomacromolecules*, **2006**, *7*, 3311-3315.
5. Mrksich, M. A surface chemistry approach to studying cell adhesion. *Chemical Society Reviews* **2000**, *29*, 267-273.
6. Shao, Y.; Fu, J. Integrated Micro/Nanoengineered functional biomaterials for cell mechanics and mechanobiology: A materials perspective. *Advanced Materials* **2014**, *26*, 1494-1533.
7. Tseng, P.; Di Carlo, D. Substrates with patterned extracellular matrix and subcellular stiffness gradients reveal local biomechanical responses. *Advanced Materials* **2014**, *26*, 1242-1247.
8. Yao, X.; Peng, R.; Ding, J. Cell-material interactions revealed via material techniques of surface patterning. *Advanced Materials* **2013**, *25*, 5257-5286.
9. Marino, A.; Ciofani, G.; Filippeschi, C.; Pellegrino, M.; Pellegrini, M.; Orsini, P., Pasqualleti, M.; Mattoli, V.; Mazzolai, B. Two-photon polymerization of sub-micrometric patterned surfaces: Investigation of cell-substrate interactions and improved differentiation of neuron-like cells. *ACS Applied Materials & Interfaces* **2013**, *5*, 13012-13021.
10. Sangeetha, N.M.; Blanck, C.; Nguyen T.T.T., Contal, C.; Mesini, P.J. Size-selective 2D ordering of gold nanoparticles using surface topography of self-assembled diamide template. *ACS Nano* **2012**, *6*, 8498-8507.

11. Bae, W.; Kim, H.N.; Kim, D.; Park, S.; Jeong, H.E.; Suh, K. 25th anniversary article: Scalable multiscale patterned structures inspired by nature: The role of hierarchy. *Advanced Materials* **2014**, *26*, 675-700.
12. Kolewe, M.E.; Park, H.; Gray, C.; Ye, X.; Langer, R.; Freed, L.E. 3D structural patterns in scalable, elastomeric scaffolds guide engineered tissue architecture. *Advanced Materials* **2013**, *25*, 4459-4465.
13. Agarwal, A.; Farouz, Y.; Nesmith, A.P.; Deravi, L.F.; McCain, M.L.; Parker, K.K. Micropatterning alginate substrates for in vitro cardiovascular muscle on a chip. *Advanced Functional Materials* **2013**, *23*, 3738-3746.
14. Hanske, C.; Mueller, M.B.; Bieber, V.; Tebbe, M.; Jessl, S.; Wittemann, A., Fery, A. The role of substrate wettability in nanoparticle transfer from wrinkled elastomers: Fundamentals and application toward hierarchical patterning. *Langmuir* **2012**, *28*, 16745-16750.
15. Snell, K.E.; Stephant, N.; Pansu, R.B.; Audibert, J.; Lagugne-Labarthe, F.; Ishow, E. Nanoparticle organization through photoinduced bulk mass transfer. *Langmuir* **2014**, *i*, 2926-2935.
16. Driscoll, M.K.; Sun, X.; Guven, C.; Fourkas, J.T.; Losert, W. Cellular contact guidance through dynamic sensing of nanotopography. *ACS Nano* **2014**, *8*, 3546-3555.
17. Krishnan, S.; Weinman, C.J.; Ober, C.K. Advances in polymers for anti-biofouling surfaces. *Journal of Materials Chemistry* **2008**, *18*, 3405-3413.
18. Grozea, C.M.; Walker, G.C. Approaches in designing non-toxic polymer surfaces to deter marine biofouling. *Soft Matter* **2009**, *5*, 4088-4100.
19. Chapman, R.; Ostuni, E.; Liang, M.; Meluleni, G.; Kim, E.; Yan, L., Pier, G.; Warren, H.S.; Whitesides, G.M. Polymeric thin films that resist the adsorption of proteins and the adhesion of bacteria. *Langmuir* **2001**, *17*, 1225-1233.
20. Therien-Aubin, H.; Chen, L.; Ober, C K. Fouling-resistant polymer brush coatings. *Polymer* **2011**, *52*, 5419-5425.
21. Gunkel, G.; Weinhart, M.; Becherer, T.; Haag, R.; Huck, W.T.S. Effect of polymer brush architecture on antibiofouling properties. *Biomacromolecules* **2011**, *12*, 4169-4172.
22. Dimitriou, M.D.; Zhou, Z.; Yoo, H.; Killups, K.L.; Finlay, J.A.; Cone, G.; Sundaram, H.S.; Lynd, N.A.; Barteau, K.P.; Campos, L.M.; Fischer, D.A.; Callow, M.E.; Callow, J.A.; Ober, C.K.; Hawker, C.J.; Kramer, E.J.. A general approach to controlling the

- surface composition of poly(ethylene oxide)-based block copolymers for antifouling coatings. *Langmuir* **2011**, *27*, 13762-13772.
23. Zhang, Z.; Chao, T.; Chen, S.; Jiang, S. Superlow fouling sulfobetaine and carboxybetaine polymers on glass slides. *Langmuir* **2006**, *22*, 10072-10077.
 24. Zhang, Z.; Finlay, J.A.; Wang, L.; Gao, Y.; Callow, J.A.; Callow, M.E.; Jiang, S. Polysulfobetaine-grafted surfaces as environmentally benign ultralow fouling marine coatings. *Langmuir* **2009**, *25*, 13516-13521.
 25. Li, G.; Xue, H.; Gao, C.; Zhang, F.; Jiang, S. Nonfouling polyampholytes from an ion-pair comonomer with biomimetic adhesive groups. *Macromolecules* **2010**, *43*, 14-16.
 26. Koch, K.; Bhushan, B.; Jung, Y.C.; Barthlott, W. Fabrication of artificial lotus leaves and significance of hierarchical structure for superhydrophobicity and low adhesion. *Soft Matter* **2009**, *5*, 1386-1393.
 27. Feng, L.; Li, S.; Li, Y.; Li, H.; Zhang, L.; Zhai, J., Song, Y.; Liu, B.; Kiang, L.; Zhu, D. Super-hydrophobic surfaces: From natural to artificial. *Advanced Materials* **2002**, *14*, 1857-1860.
 28. Sun, M.; Luo, C.; Xu, L.; Ji, H.; Ouyang, Q.; Yu, D., Chen, Y.. Artificial lotus leaf by nanocasting. *Langmuir* **2005**, *21*, 8978-8981.
 29. Berntsson, K.; Andreasson, H.; Jonsson, P.; Larsson, L.; Ring, K.; Petronis, S.; Gatenholm, P.. Reduction of barnacle recruitment on micro-textured surfaces: Analysis of effective topographic characteristics and evaluation of skin friction. *Biofouling* **2000**, *16*, 245-261.
 30. Efimenko, K.; Finlay, J.; Callow, M.E.; Callow, J.A.; Genzer, J. Development and testing of hierarchically wrinkled coatings for marine antifouling. *ACS Applied Materials & Interfaces* **2009**, *1*, 1031-1040.
 31. Aldred, N.; Scardino, A.; Cavaco, A.; de Nys, R.; & Clare, A.S. Attachment strength is a key factor in the selection of surfaces by barnacle cyprids (*balanus amphitrite*) during settlement. *Biofouling* **2010**, *26*, 287-299.
 32. Scardino, A.; Harvey, E.; De Nys, R. Testing attachment point theory: Diatom attachment on microtextured polyimide biomimics. *Biofouling* **2006**, *22*, 55-60.
 33. Vasudevan, R.; Kennedy, A.J.; Merritt, M.; Crocker, F H.; Baney, R.H. Microscale patterned surfaces reduce bacterial fouling-microscopic and theoretical analysis. *Colloids and Surfaces B: Biointerfaces* **2014**, *117*, 225-232.

34. Perera-Costa, D.; Bruque, J M.; Gonzalez-Martin, M.; Gomez-Garcia, A.C.; Vadillo-Rodriguez, V. Studying the influence of surface topography on bacterial adhesion using spatially organized microtopographic surface patterns. *Langmuir* **2014**, *30*, 4633-4641.
35. Grinthal, A.; Aizenberg, J. Mobile interfaces: Liquids as a perfect structural material for multifunctional, antifouling surfaces. *Chemistry of Materials* **2014**, *26*, 698-708.
36. Guegan, C.; Garderes, J.; Le Pennec, G.; Gaillard, F.; Fay, F.; Linossier, I., Henry, J.M.; Bellon Fontaine, M.N.; Vallee Rehal, K. Alteration of bacterial adhesion induced by the substrate stiffness. *Colloids and Surfaces B: Biointerfaces* **2014**, *114*, 193-200.
37. Decker, J.T.; Kirschner, C.M.; Long, C.J.; Finlay, J.A.; Callow, M.E.; Callow, J.A., Brennan, A.B. Engineered antifouling microtopographies: An energetic model that predicts cell attachment. *Langmuir* **2013**, *29*, 13023-13030.
38. Myan, F.W.Y.; Walker, J.; Paramor, O. The interaction of marine fouling organisms with topography of varied scale and geometry: a review. *Biointerphases* **2013**, *8*, 30.
39. Carmesin, I.; Kremer, K. The bond fluctuation method - a new effective algorithm for the dynamics of polymers in all spatial dimensions. *Macromolecules* **1988**, *21*, 2819-2823.
40. Schoch, P. K.; Genzer, J. Adsorption of "soft" spherical particles onto sinusoidally-corrugated substrates. *Soft Matter* **2014**, *10*, 7452-7458.

CHAPTER 4

Adsorption of Size-Polydisperse Particles on Sinusoidally-Corrugated Surfaces

Manuscript in preparation:

P.K. Schoch and J. Genzer, 2015.

Adsorption of Size-Polydisperse Particles on Sinusoidally-Corrugated Surfaces

Phillip K. Schoch and Jan Genzer*

Department of Chemical and Biomolecular Engineering, North Carolina State University,
Raleigh, North Carolina

Abstract

We use our Monte Carlo adhesion computer simulation model developed previously to study core-shell spherical particles of polydisperse size settling on sinusoidally-corrugated substrates. The core-shell particles are composed of a hard inner core with an adhesive shell that mediates interaction with the substrate lattice elements. This simulation model allows multiple particles to settle onto each tested substrate to elucidate the behavior of the collective adhesive layer. Additionally, the probability distribution of particle sizes (diameters) is determined by either a single normal distribution function ($D_{\text{mean}}=20$) of standard deviation 0-8 (0-40% of D_{mean}) or a bimodal distribution function constructed by adding the probability distributions of two normal distributions of differing mean values. Particles move within a 3D lattice space and settle on the substrate due to attractive particle/substrate interactions. Once a single particle adheres to the substrate, a new particle is introduced into the lattice to begin a new settlement. Through this multi-particle settlement mode, we explore the interplay among the characteristics of the particles (*i.e.*, size and interaction shell) and the substrates (*i.e.*, wavelength and periodicity). We measure the

number of particles adsorbed, their sizes and their adhesion strength to the substrate. We analyze the ability of these sinusoidal substrates to reduce either number of adsorbed particles or the aggregate adhesion strength of adsorbed particles relative to flat substrates. Using comparisons of these surface textures to flat substrates we note the surface texture reduce adhesion strength by up to ~40% for feature height 20 at $\lambda/D_{\text{mean}} = 0.5$ depending on the standard deviation. Furthermore, we examine the settlement of particles with bimodal size distributions on these corrugated substrates. When using the mean particle size ratio of $D_{\text{meanB}}/D_{\text{meanA}}$, where $D_{\text{meanB}} > D_{\text{meanA}}$, we observe that for mean particle size ratio of 2 our surface texture continues to reduce the adhesion strength of particles by ~40-50% for some combinations of feature width and feature height when compared to flat analogues. However, at mean particle size ratio of 4, the surfaces tested were no longer able to reduce significantly. The best feature width and feature height combinations incurring only a ~0-5% reduction in particle adhesion when compared to flat analogues. This suggests that when particle sizes are far apart, either a second texture or a chemical coating is needed to act against the smaller particles.

4.1 Introduction

The settlement and adhesion of particles with polydispersity in size onto varying substrates is important to many fields including, biofouling and particle sorting [1-16]. In this work, we focus on the adsorption of multiple spherical particles of varying size-polydispersity onto topographically-corrugated substrates featuring sinusoidal patterns. These particles interact with the substrates via an-adhesive shell present on the surface of hard-core particles. Such a system approximates the adsorption of small biological organisms (*i.e.*, cyprids or zoospores) that settle with a host of other species concurrently or may have variations in size themselves. This work aims to understand the efficacy of periodic substrate topography in governing the adhesion of polydisperse fouling particles. In order to evaluate the efficiency of topographically corrugated substrates in combating adsorption of size-polydisperse particles, we employ two benchmark systems. First, an adsorption of the same population of size-polydisperse particles onto flat surfaces. Second, an adsorption of particles with uniform sizes (monodisperse) onto topographically-corrugated substrates with the same shape and feature width/height as in the case of the adsorption of size-polydisperse particles.

Use of substrate topography to control the adsorption of “foulants” is less emphasized compared to research pertaining to chemical composition of coatings aimed to reduce or prevent adsorption. In biofouling, most efforts have aimed at reducing the adsorption of foulants via chemical methods [17-25]. For example, ethylene glycol [17,22,26] or some charge-bearing surfaces [23-25] are capable of minimizing (at least temporarily) bioadsorption. Utilizing substrates with engineered surface topographies provides an

alternative means towards enhancing the resistance of materials surfaces to fouling by controlling the number of interaction points between the foulant and the adsorbing surface. Nature provides ample inspiration for controlling the extent and strength of adsorption on nano- and micro-structured substrates. One of the best-known examples is the Lotus leaf that creates a superhydrophobic surface by minimizing the number of contacts between the adsorbing water or other hydrophilic liquid, and the substrate through the combination of waxy hydrophobic residues on nanostructured substrate features and their spatial arrangement on the substrate [27-29]. The synergy between the chemical and topographical properties of the Lotus leaf yields low adhesiveness and self-cleaning characteristics [27]. Several studies have explored experimentally the application of textured surfaces in preventing biological adhesion. Examples include the Sharklet patterns [30-32], hierarchical wrinkles with multiple dimensions [1,33], corrugated periodic structured substrates [18,30,34-38] or substrates with random topographical features. In spite of these efforts, fundamental understanding about the role of the shape, periodicity, and amplitude of topographically-corrugated substrates in influencing adsorption of size-monodisperse particles is lacking. Including size polydispersity of the particles into the overall picture increases the complexity of the problem even further. Previous studies have alluded to contact point theory [30,34-36] and investigated periodic topographies with promising results; yet those studies did not develop a substantial theoretical basis for predicting fouling behavior.

To build off previous computer simulation efforts at understanding how periodically textured substrates can be effective against particle adsorption, we expand our existing

computer simulation model to consider adsorption of particles with size distributions. In our model, the fouling particles are simulated as hard-core species that exhibit an implicit interaction field (shell) that interacts with the underlying substrate. We modify systematically the frequency (feature width) and amplitude (feature height) of the substrates and study their effects on the adsorption of particles with variable particle diameters. In this model, we modulate the polydispersity of adsorbing particles using normal distributions and adjusting the standard deviation. Additionally, we combine normal distributions into a composite to form a bimodal distribution. This allows us to analyze how significant of size differences these sinusoid surfaces can tolerate.

4.2 Computer Model

We employ a Monte Carlo simulation scheme to model the behavior of adhesive hard sphere particles on substrates featuring sinusoidal profiles defined by their amplitude and frequency/wavelength. In this work, we refer to the wavelength as surface feature width and amplitude as feature height. The spherical particles interact with the corrugated substrates via non-specific interactions in an effective interaction shell present on the surface of the particle. The adhesion energy for each particle is calculated by counting the number of surface lattice sites within the effective interaction shell of the adhering particle. These particles are allowed to perform one move per Monte Carlo step (MCS) in one principle direction (*i.e.*, $\pm x$; $\pm y$; and $\pm z$) within a cubic lattice. After each MCS, the total adhesion energy for all particles is calculated and recorded; the spatial location of each particle is also

recorded. System testing was performed at high number of MC steps (*i.e.*, 50,000 steps per particle) to ensure all particles were able to reach multiple maxima in their allotted settlement MC steps. After these steps, the location, where the particle achieves its highest adhesion energy, is considered as its settled location on the substrate. Particles are inserted onto the lattice sequentially, *i.e.*, only one particle moves at any time and all settled particles remain stationary. We do not increase the allotted number of MC steps for new particles because the total number of MC steps was equilibrated such that a single particle has ample time to explore a large area and reach several maxima. The simulation ends once twenty consecutive trials for a given particle have failed to attach that said particle to the surface. Twenty trials was chosen as an amount through testing to achieve near maximum number of particles adsorbing without giving too many trials that would allow very low probability small particles to dominate. We note that in our model, a particle is considered to be adhered to the substrate if it is in a direct contact with the substrate. Thus, in determining the strength of particle adhesion, we do not account for particles in multilayer assemblies that are not attached directly to the substrate. It would be interesting to revisit the problem and compare the results of this model to a scheme, which considers concurrent motion of all particles. This, however, is outside the scope of the current work.

Figure 4.1 provides the layout of the simulation set up and defines the parameters of the corrugated substrate and the particles employed in the simulation. Specifically, the substrates comprise sinusoidal topographies with adjustable amplitude and wavelength, referred to as feature height and feature width, respectively. Data discussed in this paper include a set of three feature heights and five feature widths plus flat analogues, which

combined create 16 unique surfaces for each set of particle conditions tested. The core-shell particles are defined by their core diameter (D_{core}), size of interaction shell (D_{shell}). D_{shell} is the same for all particles and is defined as $D_{\text{core}} + (10)^{0.5}$; this was taken from previous simulations as the maximum bond length for coarse-grained elements in bond fluctuation model (BFM). In this work, we aim to test the effectiveness of surface textures on monodisperse versus polydisperse sets of particles centered of the same mean value ($D_{\text{core mean}}$). Later, we explore the effects of bimodal distributions on the effectiveness of surface textures to prevent or reduce particle settlement. In order to create polydisperse particles centered at the same mean value, we use a normal distribution random number generator (RNG) to generate normally distributed particle diameters (D_{core}). To change the polydispersity, we modulate the standard deviation of the normal distribution. $D_{\text{core mean}}$ value is set at 20 for non-bimodal distributions. **Figure 4.2** (top) illustrates the different distributions by plotting the probability density function to diameters generated. In addition, the distributions are broken up into colored bins of diameters that will be used to track the settlement of particles as groups on the substrate. Standard deviations (STD) of 2, 4 and 8 were used. In bimodal testing, two normal distributions are generated and given equal probability. Bimodal distribution of $D_{\text{core meanA}} = 10$ (STD 1) and $D_{\text{core meanB}} = 40$ (STD 4) as well as bimodal distribution of $D_{\text{core meanA}} = 20$ (STD 2) and $D_{\text{core meanB}} = 40$ (STD 4) were simulated. The $D_{\text{core meanA}} = 10$ (STD 1) and $D_{\text{core meanB}} = 40$ (STD 4) bimodal distribution can be found in **Figure 4.2** (bottom). Further we characterize this bimodal distribution by the ratio of these two mean values, such that size ratio = $D_{\text{core meanB}} / D_{\text{core meanA}}$. Each data point

presented denotes an average quantity obtained by averaging ten independent simulation sets using the same input parameters.

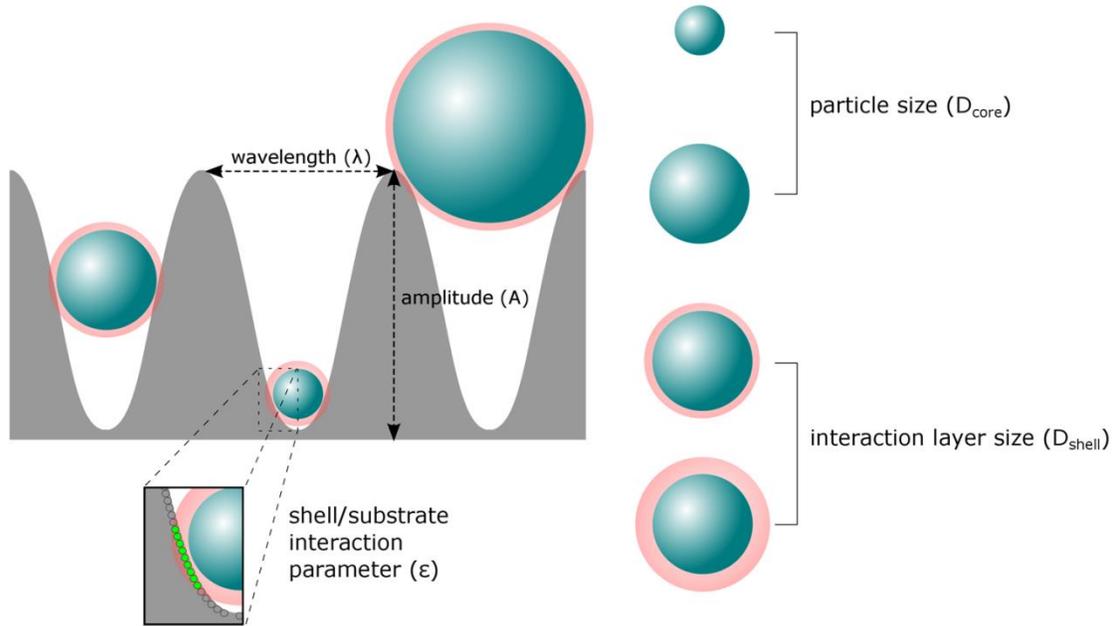


Figure 4.1. Simulation schematic detailing the basics of the simulation setup. The substrate in gray, is defined by $F(x)=A*\sin(\lambda\pi x/x_{max})$ where A varies from 0 to 80 and λ varies from 5 to 80. The particles (green) are defined by their diameter (D) and interact with the substrate adhesively via an interactive shell (light red).

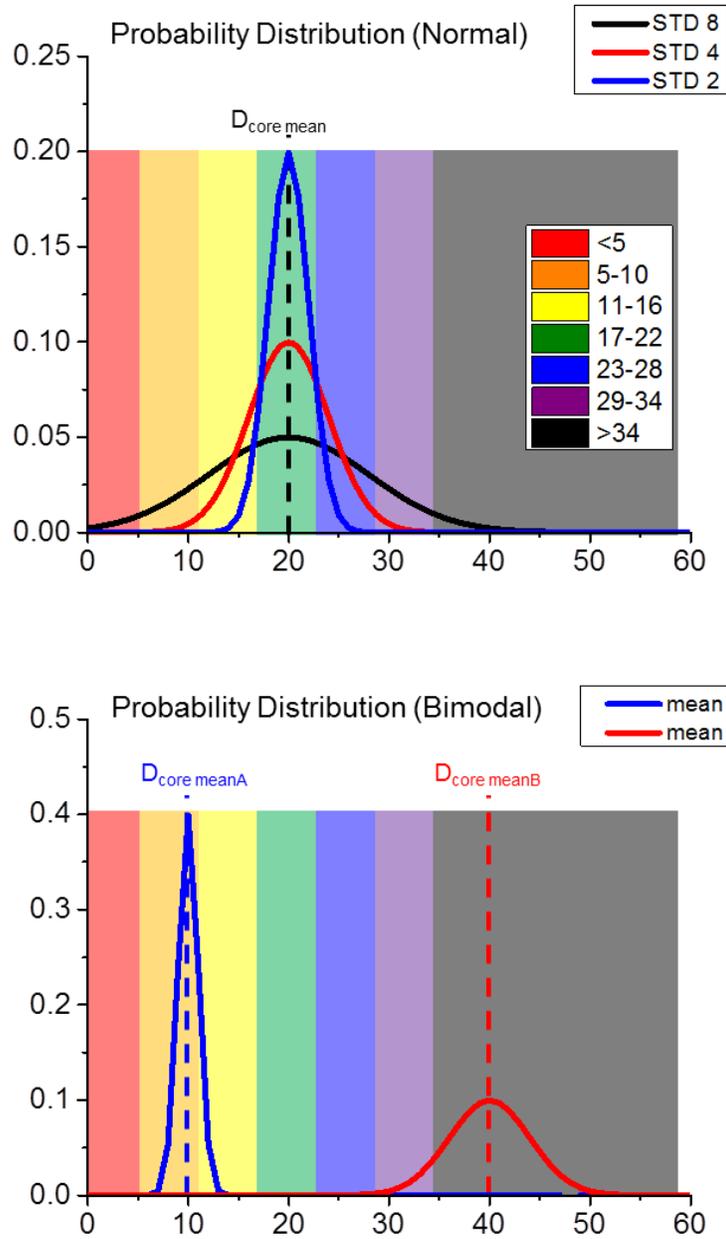


Figure 4.2. (Top) Probability Density Functions for normal distributions with $D_{\text{core mean}} = 20$ and standard deviations (2, 4, 8). The distributions are binned by diameter and colored according to the legend on the right. (Bottom) Construction of a bimodal distribution $D_{\text{core meanA}} = 10$ (STD 1) and $D_{\text{core meanB}} = 40$ (STD 4) is plotted according to their probability density functions. $D_{\text{core meanA}}$ is colored blue while $D_{\text{core meanB}}$ is colored red. Their respective means are shown by the dashed vertical lines.

4.3 Results and Discussion

4.3.1 Polydisperse vs. Monodisperse Particle Distributions on Sinusoidal Substrates

One of the main goals of this study is to compare the assembly of particles with predefined distribution of sizes to the same behavior of particles with a uniform size distribution. This is accomplished by using the same mean value for D_{core} of the simulated particles and altering the standard deviation of a normal distribution to change the polydispersity of the particle distribution. **Figure 4.3** details visually the differences that result when comparing the settlement of monodisperse and polydisperse particle distribution settling on sinusoidally corrugated surfaces with various feature widths and feature heights. The top set of surfaces depicts the monodisperse case where $D_{\text{core mean}} = 20$ (monodisperse) and the bottom set of surfaces is the most polydisperse case where $D_{\text{core mean}} = 20$ with a STD 8. Particles in this figure are colored by the legend on the right by their core diameter previously shown in **Figure 4.2**. As mentioned in **Figure 4.2**, each color corresponds to a collection of particle that belong to a single bin; the sizes of the particles that are members of a given bin are shown by the numbers in the legend next to each corresponding color field. Moving from left to right in the figure, the surfaces have increasing feature width. At feature widths greater than the diameter of individual particles ($\lambda > D$), we observe these particles begin penetrating into the surface structures. In the polydisperse case, initially only the smallest particles ($D_{\text{core}} < 5$) can penetrate. By the midpoint of feature width (20), $\lambda / D_{\text{mean}} = 1$, particles $D_{\text{core}} < 20$ penetrate the surface protrusions. Finally, at the largest feature width (80), $\lambda / D_{\text{mean}} = 4$, all particle diameters are able to penetrate and the surface is ineffective against these particles.

Contrasting this to the monodisperse case, the particles do not begin significant penetration of the surface at high feature height, until feature width > 20 , $\lambda/D_{\text{mean}} > 1$. Recall from previous work that our $D = 20$ particles were at their lowest adsorption counts for $\lambda/D = 0.5$ [39,40].

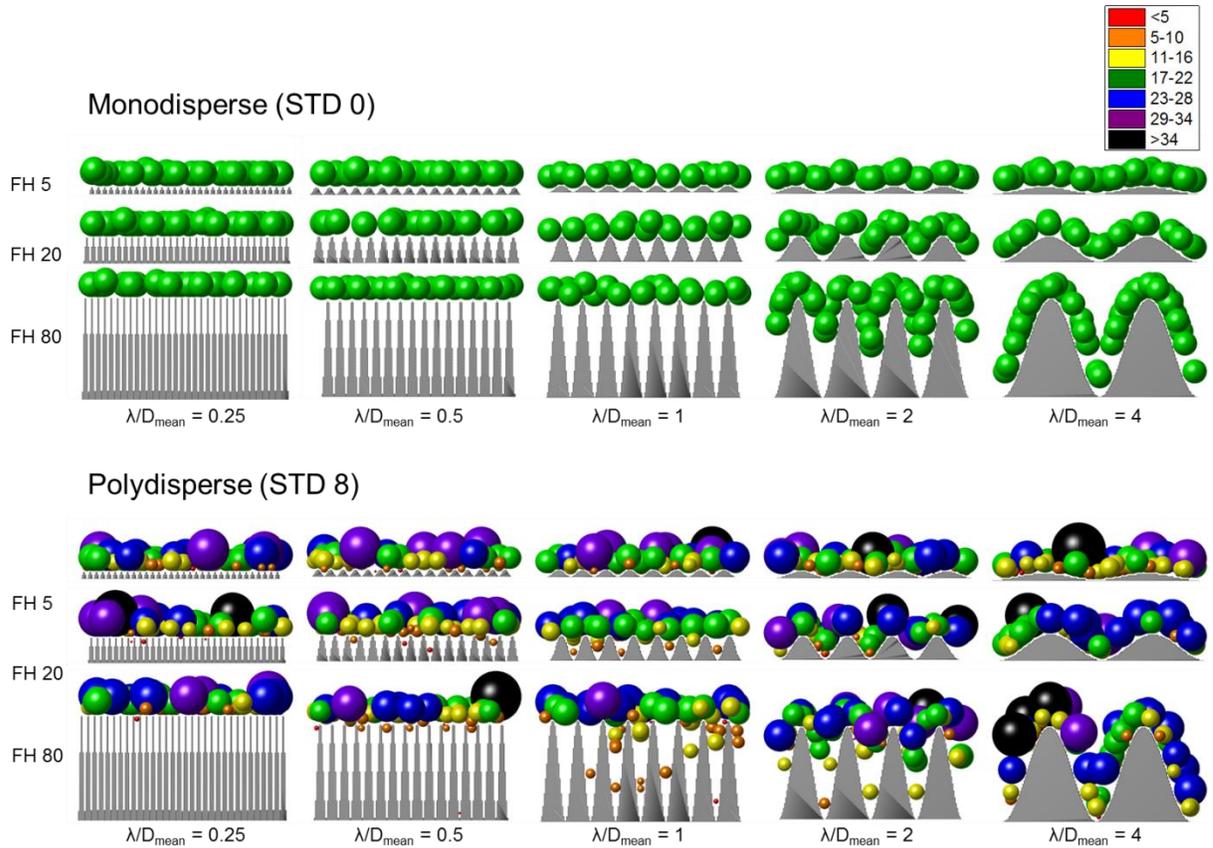


Figure 4.3. Settlement of monodisperse (top) and polydisperse (bottom) particles on a variety sinusoidal surfaces with feature heights $FH = 5 - 80$ and feature widths (λ) relative to $\lambda/D = 0.25 - 4$. Wavelength increases from left to right; feature height increases from top to bottom; the particles are colored according to the legend by particle diameter.

Along with this visual position data, we collect information about particle count and adhesion energy, as shown in **Figure 4.4** and **Figure 4.5**, respectively. Both figures utilize the same legend for coloring the particle count and adhesion energy contributions of the respective particle core diameters as **Figure 4.3**. This allows the data to not only show the aggregate particle count and adhesion energy but visualize the breakdown of the contributions of small, medium and large particles to the result. Looking at **Figure 4.4**, we observe that as the polydispersity (*i.e.*, STD) increases from left to right more particles accumulate on the surfaces; this is true particularly for particles smaller than the mean diameter ($D_{\text{core}} < 20$). As we discuss later (*cf.* **Figure 4.9**), this occurs due to available substrate space for larger particles being occupied as more particles adsorb, but enough substrate space remains accessible to the smaller particles as they can move around the larger particles. The other noticeable effect seen in this data is the similar shape for the different feature height data sets (rows), *i.e.*, for feature height 80 (bottom row) the smallest values of particle count at $\lambda < 10$ are followed by increasing particle counts as λ increase from 20 to 80.

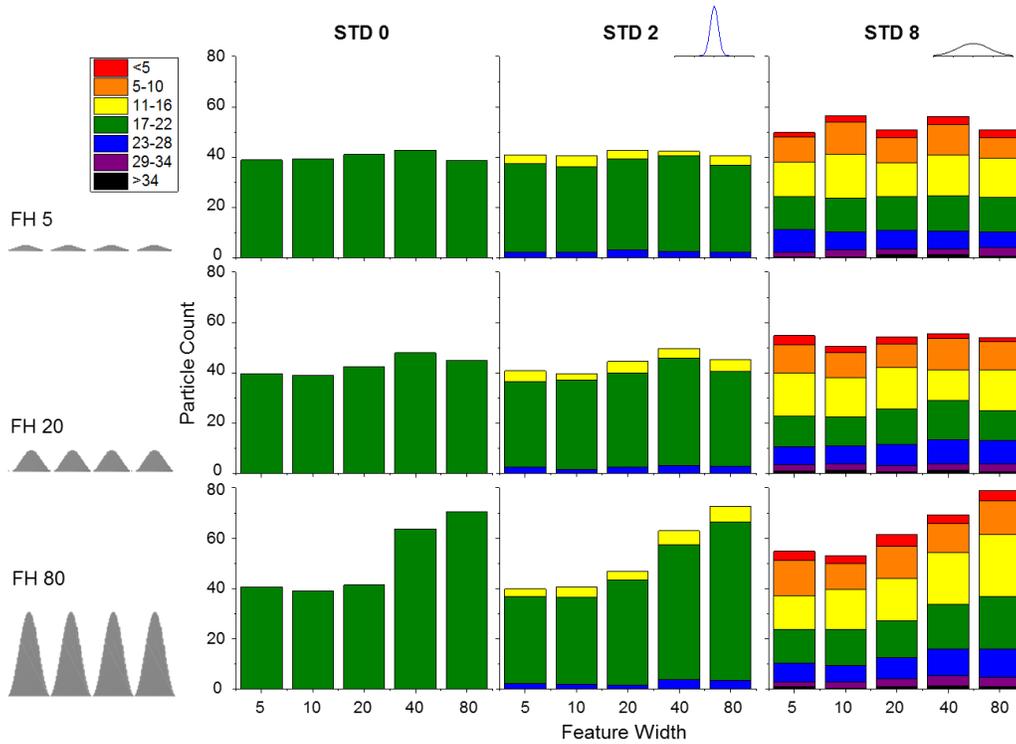


Figure 4.4. Varying the width of the normal distribution by modulating the standard deviation of the distribution function results showing settled particle counts as a function of feature width (λ). The distributions are composed of stacked columns colored by diameter of particles contribution. Increasing the standard deviation of the adsorbing particles leads to increased total particles adsorbed.

While monitoring the adhesion energy of different particle distributions on sinusoidally-corrugated substrates, we notice a few other trends (*cf.* **Figure 4.5**). Most importantly, we detect the emergence of critical adsorption feature width in the region of $\lambda/D_{\text{core mean}} \sim 0.5-1.0$ ($10 \leq \lambda \leq 20$) as seen in previous publications [39,40]. The value of $\lambda/D_{\text{core mean}} = 0.5$ ($\lambda = 10$) shows up across all data sets as a minimum of adhesion energy. This minimum occurs due to the majority of particles being too large to penetrate into the

surface ($\lambda < D$), thus preventing higher adhesion energies as the excess surface area is not seen by the particles. Examining the adhesion energy for $\lambda = 10$, we note that the increasing polydispersity of particle diameters (*i.e.*, increasing STD, columns in **Figure 4.5** from left to right) mitigates this effect to some degree, as the higher abundance of smaller particles in STD 8 are able to adsorb readily on the substrates. The feature height 20 and feature width 10 represents the minimum adhesion energy for this system. This combination of feature height and feature width creates a mismatch in the radius of curvature between the substrate peaks and the adhering spherical particles, reducing the amount of surface lattice sites inside the interactive shell.

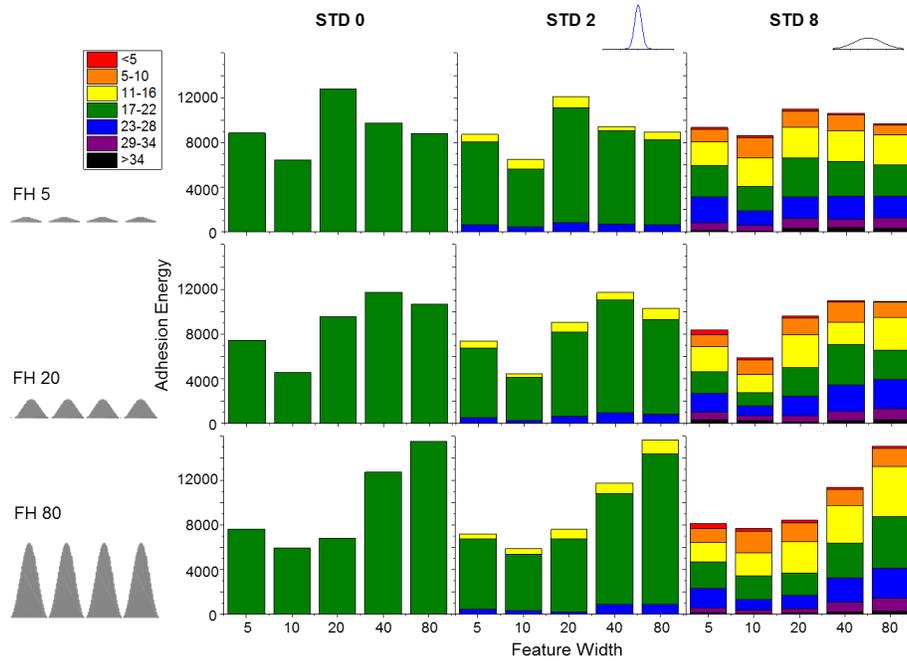


Figure 4.5. Varying the width of the normal distribution by modulating the standard deviation of the distribution function results showing settled particle adhesion energy as a function of feature width (λ). The distributions are composed of stacked columns colored by diameter of particles contribution. Increasing the standard deviation of the adsorbing particles leads to increased total adhesion energy in some cases.

When examining the data in **Figure 4.4** and **Figure 4.5** we notice the increasing proportion that the smaller particles ($D < 20$) play in the number of adsorbed particles and adhesion energy of those particles as the polydispersity increases to STD 8. To compare the polydisperse data sets and the monodisperse case, in **Figure 4.6** we plot the particle count (**Figure 4.4**) and the adhesion energy (**Figure 4.5**) data relative to the monodisperse case. For these plots, values greater than 1 indicate performance worse than the monodisperse case. At $\lambda > 20$ and < 10 , we note that the adhesion energy of all distributions is similar. The monodisperse case outperforms the polydisperse cases for feature width 10. At all conditions, the surfaces exposed to the polydisperse particles adsorb more particles than the monodisperse case, in some cases (STD 8) ~50% more particles than monodisperse. To further our analysis of these surfaces we need to compare the adsorption of size-polydisperse particles to flat substrates.

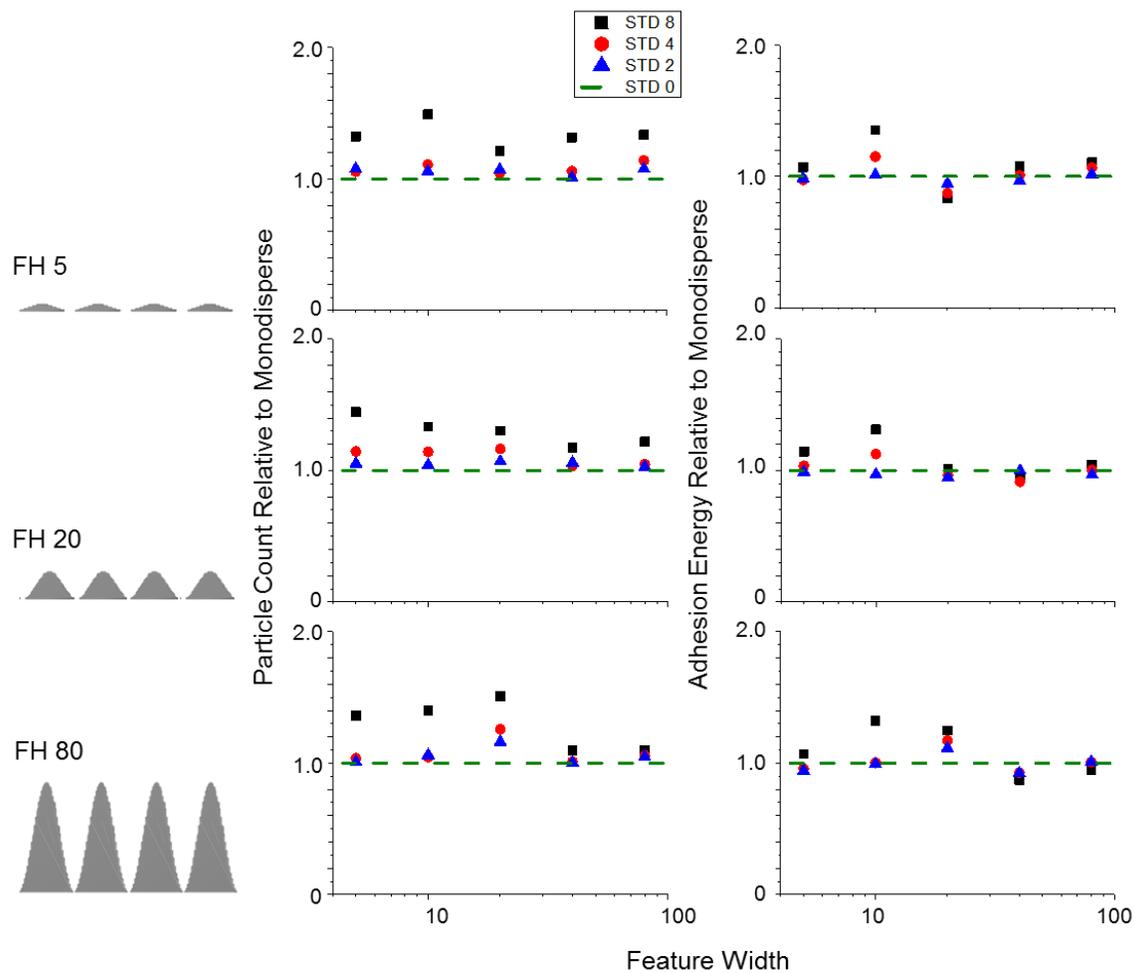


Figure 4.6. Adsorbed particle counts (left column) and adhesion energy (right column) relative to the monodisperse case for normal distributions of standard deviations 4 (black squares), 2 (red circles) and 1 (blue triangles). Monodisperse plotted as horizontal green dashed line. More particles adsorbed for all distributions vs monodisperse. In some conditions, the polydisperse conditions have lower energy than monodisperse and in other cases have higher energy.

4.3.2 Polydisperse and Monodisperse Particle Behavior Relative to Flat Substrates

Another main goal of this study is to utilize particle adsorption on flat substrates as a basis of comparison relative to particle settlement on textured surfaces. If the textured surfaces are unable to outperform flat substrates then they would not be very useful in preventing or reducing particle adhesion. Thus for each particle distribution we simulate the same adsorption process on flat substrates. We can then scale our adsorption data obtained from adsorption on corrugated substrate relative to the values obtained for flat substrates. **Figure 4.7** details this relative behavior for all particle distributions for various sets of feature heights and feature widths tested relative to their respective flat analogues. The numbers of adsorbed particles are similar to flat substrates for most feature heights until the largest feature height, FH 80 (bottom row). For feature height 80, in particular, the number of particles adsorbed begins a significant takeoff at feature width ≥ 20 where the majority of particle sizes can penetrate the surface to access the extra surface area of the sinusoid. Interestingly, only the feature widths of 40 and 80 exhibit higher adhesion energy for this same feature height. Thus, while more particles may be adsorbing at feature width 20, those particles that do adsorb do so with lower total adhesion energies than they do on flat surfaces. Across all feature heights, we see that the textured surfaces outperform the flat substrates significantly at feature width of 10 with up to 50% adhesion energy reduction at FH 20. This occurs at $\lambda/D_{\text{core}} = 0.5$ as had been shown in our previous studies [39,40]. However, the depth of this minimum relative to the flat substrates decreases with increasing particle

polydispersity, *e.g.* at FH 80 and FW 20 STD 0 and 2 (~20% lower adhesion energy) to STD 4 and 8 (~10% lower adhesion energy) relative to flat substrates.

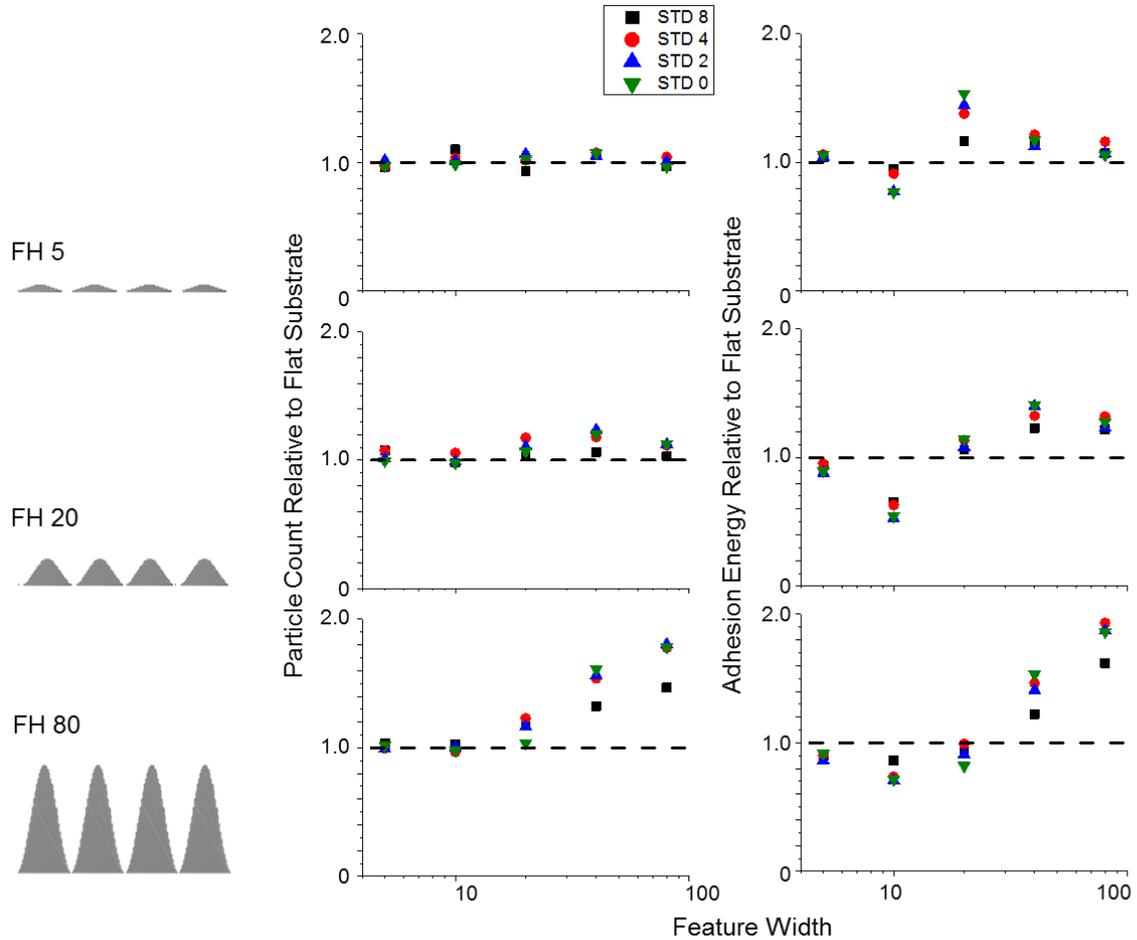


Figure 4.7. Adsorbed particle counts (left column) and adhesion energy (right column) relative to their flat analogues for normal distributions of standard deviations 4 (black squares), 2 (red circles), 1 (blue triangles) and 0 (green downward triangles). Flat substrates plotted as horizontal black dashed line. Textured substrates outperform flat substrates below feature width of 20 in adhesion energy. At and above feature width 20, the textured substrates perform worse as excess surface area is readily available as more particles adsorb.

We further aim to comprehend the adsorption energy behavior of settled particles within each of the aforementioned bins for each STD considered. In **Figure 4.8** we plot the adhesion energy of particles (relative to the flat substrate) as a function of feature width for three different feature heights (rows) for three STD values: 0 (*i.e.*, monodisperse, left column), 2 (middle column), and 8 (right column). We evaluate the affinity of particles within each of the particle bins (see legend to **Figure 4.8**) to adhere to the corrugated substrate defined by feature width and feature height relative to flat substrates. In **Figure 4.8** positive values indicate this particle size range achieved adhesion energy higher than that on flat substrates and negative values indicate adhesion energy lower than that achieved on flat substrates. By this measure, we can evaluate how well the specific particle size “likes” the substrate. For example, looking at the first column of data (monodisperse) we see the green bars indicating the D_{core} 17-22 bin have a minimum as previously stated as $\lambda/D_{\text{core}} \sim 0.5$. This data analysis confirms our hypothesis across all particle sizes, namely, that when the $\lambda/D_{\text{core}} < 1$ the particle tends to adsorb less strongly to the substrate. In many cases a 25-50% decrease in adhesion energy is observed when $\lambda/D_{\text{core}} < 1$. When the feature width becomes sufficiently small larger particles begin adsorbing similar to flat again; thus at $\lambda/D_{\text{core}} \ll 1$ we see flat adsorption energies (values close to zero). This behavior is seen in feature height 5 and 20 for most particle sizes where feature width equals 5. Very small particles ($D_{\text{core}} < 5$) stick strongly to surfaces with low feature widths and achieve greater than 50% increase in adhesion energy for several feature widths and feature heights. However, as the feature width increases particles regress to their flat substrate energies (trend towards zero) due to the surface “feeling” locally flat to these small particles at high λ . This data set shows clearly the

cutoff points in the effectiveness of the various surface textures against adhesion of polydisperse particle populations. One could imagine if the particle population had more very small particles they would adhere strongly and likely be difficult to remove from the substrate. Populations with many small particles will be discussed later with bimodal distributions.

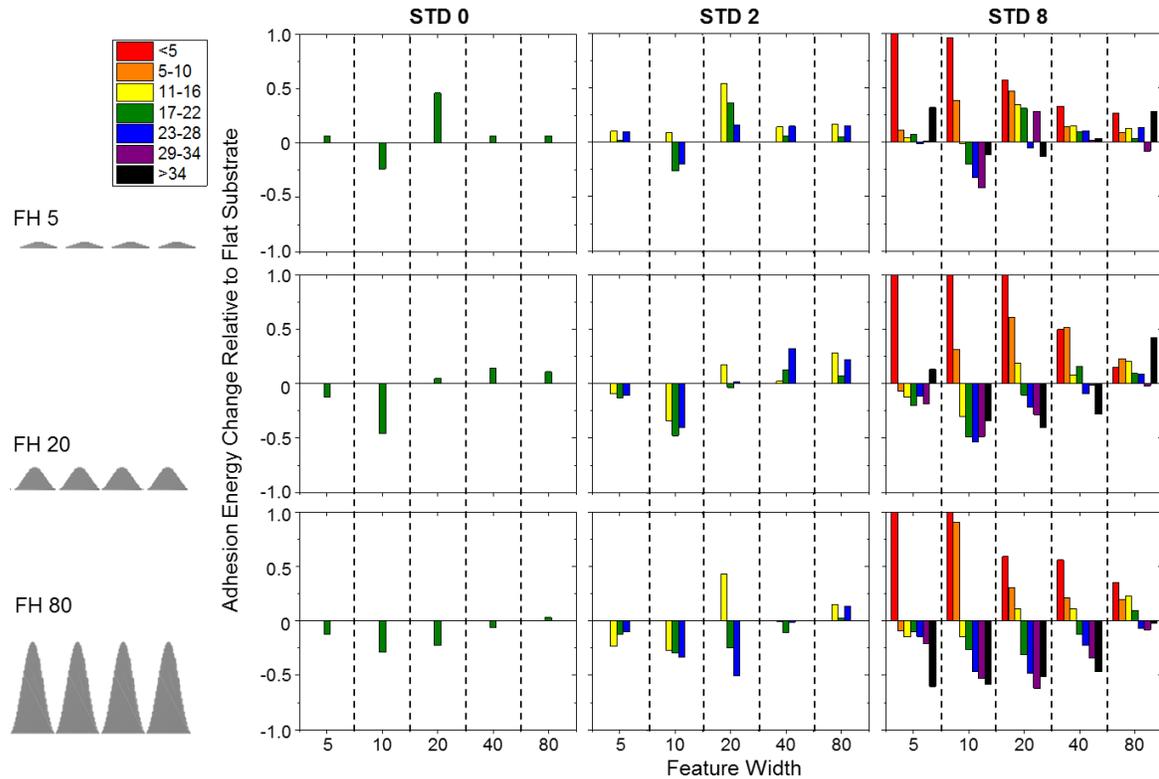


Figure 4.8. Adhesion energies of particle diameters (colored by bin) relative to that for flat substrates. Columns color corresponds to legend for diameter of particles. High amplitude substrates perform best at creating sub-optimal adhesion for particles greater than or equal to the feature width. Large particles sense the substrates as flat for very high and very low feature width.

Figure 4.9 compares the distribution probability of various particle sizes as simulated by our random number generator (*i.e.*, “bulk assembly” particles) relative to the probability distribution detected in the adsorbed particles on our surfaces. As is apparent from the particle size distributions, the surface adsorbed particle sizes skew towards smaller particles and this phenomena appears especially at larger polydispersities. We can see these changes clearly by scaling the probabilities of the surface adsorbed particles to what is generated by the random number generator. For this scaling, we define the fractional deviation as the probability of the size for particles adsorbed divided by the probability of particles generated minus unity. This approach offers a measure of a fractional deviation from the normal distribution where positive values indicate adsorbed particle sizes that were more abundant than expected by a normal distribution and negative values indicate adsorbed particles were less abundant than in a normal distribution. Here we see how significantly the small particles are favored by steric effects over the large particles. Some small adsorbed particles were >75% more abundant than in a normal distribution and some large particles >75% less abundant than in a normal distribution. This is due to the ability of the small particles to continue adsorbing after the available space for larger particles is already occupied. At very long adsorption times, we would expect to see this effect further exacerbated.

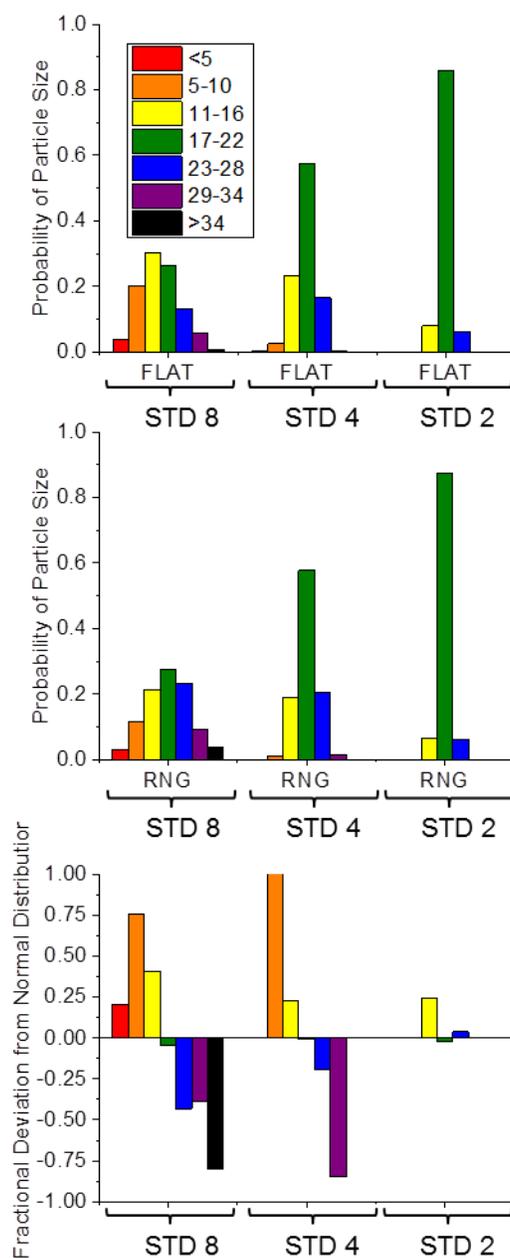


Figure 4.9. (Top) Particle probability distributions of our normal random number generator (RNG) compared to the adsorbed particles on flat substrate. (Bottom) Fractional deviation from the flat substrates relative to the random number generator for particle sizes. Diameters colored as per legend.

4.3.3 Behavior of Bimodal Distributions on Sinusoidal Substrates

Previously our simulations worked off the basis of an entire distribution centered on a single mean value for D_{core} . Here we consider one more extension to our existing model and create bimodal distributions to test the efficacy of textured surfaces in resisting particle adsorption. This system is meant to be akin to different species of marine foulers adsorbing with distinctly different sizes yet similar chemical adhesiveness. For this reason we test a bimodal setup with $D_{\text{core meanA}} = 20$ and $D_{\text{core meanB}} = 40$ (hereafter denoted as 20-40) as well as another with $D_{\text{core meanA}} = 10$ and $D_{\text{core meanB}} = 40$ (hereafter denoted as 10-40). **Figure 4.10** provides a snapshot of particles of different sizes at their respective adsorbed positions on surfaces of five feature widths and three different feature heights. If we look specifically at the highest feature heights, we can see that the 20-40 and 10-40 distributions exhibit very different adsorption behaviors. For the 20-40 distribution, we see that at $\lambda > D$ the respective particle sizes penetrate and adsorb on the surface readily. At feature width 40 we observe a case of the smaller particle set penetrating while the larger particle are still excluded from the excess surface area. While this behavior is nearly identical to that of the 10-40 distribution, the onset of particle penetration is significantly different between the two bimodal distributions. In the 10-40 case of $D_{\text{core meanA}} = 10$, the particles penetrate the surface starting at feature width 20 while the larger particles must “wait” until feature width 80.

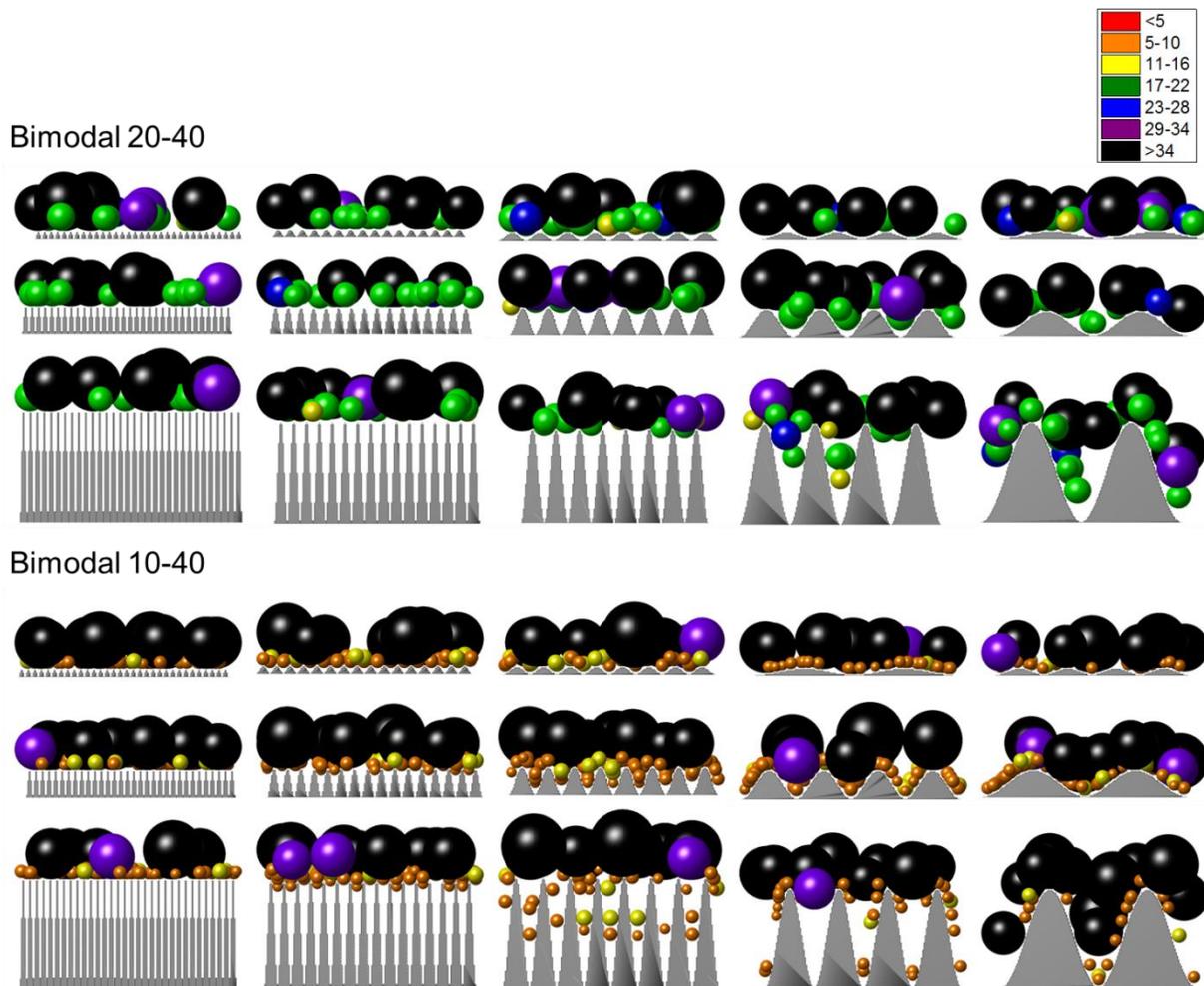


Figure 4.10. Side views of adsorbed particle locations for two bimodal distributions, (Top) bimodal of 20 and 40 diameter, (Bottom) bimodal of 10 and 40 diameter. Evident that the further apart the particle mean diameters are, the greater the penetration into the substrate by the smaller particles.

The corresponding adhesion energy for the two bimodal distributions are plotted as a function of feature width and three feature heights (FH 5, 20, 80) in **Figure 4.11**. Here we see that the bimodal 20-40 system retains low adhesion energies by the textured substrates especially at feature widths of 10 and 20. This is due to overlap in the minima of adhesion

energies for the two modes in the 20-40 system. However, the 10-40 does not possess low adhesion energies at any feature width. The texture is able to reduce the adhesion of very large particles for the feature width of 10 and 20, but at that same condition the $D_{\text{core}}=10$ particles adsorb readily and create maxima in the overall adhesion energy. **Figure 4.12** demonstrates this effect clearly. We note that the 20-40 distribution (left column) has reduced adhesion for most if not all particle sizes at feature width 10 for all feature heights. In the case of the 10-40 distribution, we the D_{coreB} particles contribute far less energy than the smaller D_{coreA} particles. These smaller particles (D_{coreA}) have higher energies than on flat substrates beginning at feature width 10.

Finally, we can compare our textured substrates to their flat counterparts for total number of adsorbed particles and total adhesion energy. This comparison yields information whether surface texture is advantageous for the bimodal distributions. **Figure 4.13** displays the number of adsorbed particles (left column) and adhesion energy (right column) relative to flat surfaces for both bimodal distributions and all surface textures. We detect large differences in surface adsorption effects on the particle counts and adhesion energies for the 20-40 vs. 10-40 distributions. For discussion of these particle size distributions, we define a size factor defined here as the ratio of the two peaks in the bimodal distribution, $D_{\text{core meanB}}/D_{\text{core meanA}}$. When the distribution is as far apart as the 10-40, a size factor of mean particle size ratio of 4 (40/10), the surfaces fail to control more than one set of particles at a time concurrently leading to significant number of particles adsorbed and high adhesion energies at larger feature heights. Increases in number of particles and adhesion energies for the 10-40 distribution of 50-75% for some surfaces relative to flat substrates. In contrast, for

the 20-40 distribution, a size factor of mean particle size ratio of 2 (20/10), the number of adsorbing particles stays at the level observed for flat substrates. The adhesion energy is actually reduced 25-50% relative to flat substrates for feature width of 10 and for feature heights 20 and 80 at feature width 20. These bimodal distributions point out how increasing the size factor of mean particle size ratio from 2 to 4 can cause the surface texture to perform no better or worse than flat substrates at reducing adsorbed particle numbers and adhesion strength.

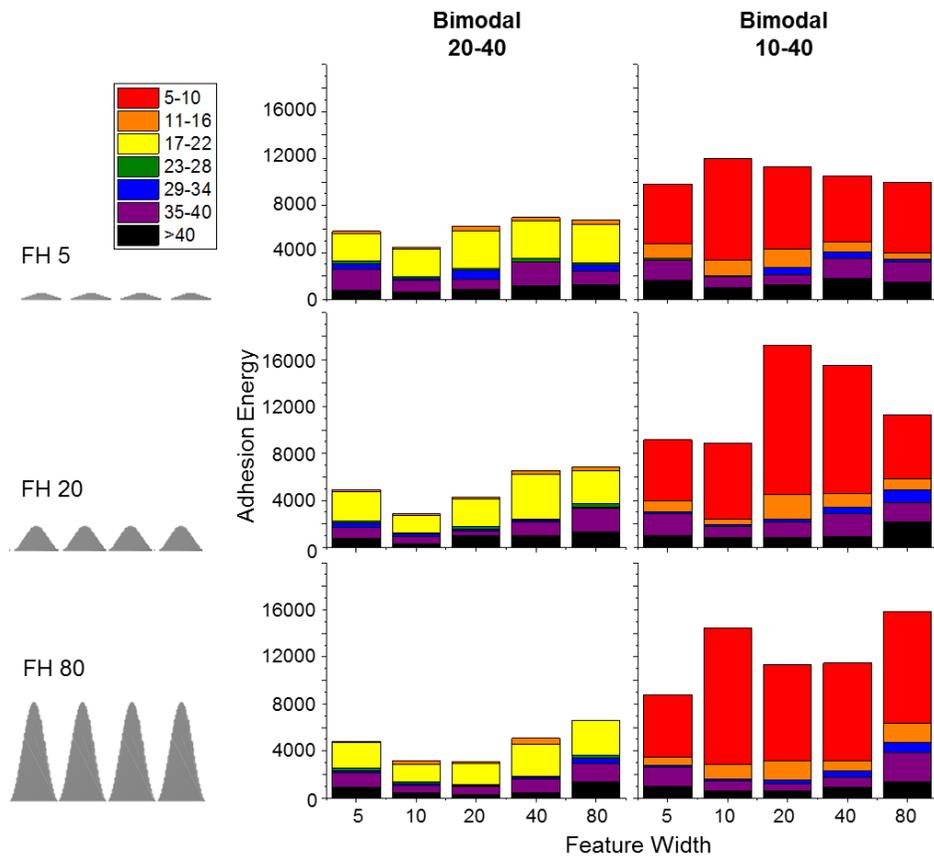


Figure 4.11. Adhesion energy colored by contribution by particle diameter for two different bimodal distributions. Bimodal 5-20 has significantly higher adhesion energies as many more particles adsorb for most feature widths. At large feature width, the second mode at diameter 40 is able to penetrate the surface and increase the adhesion energy.

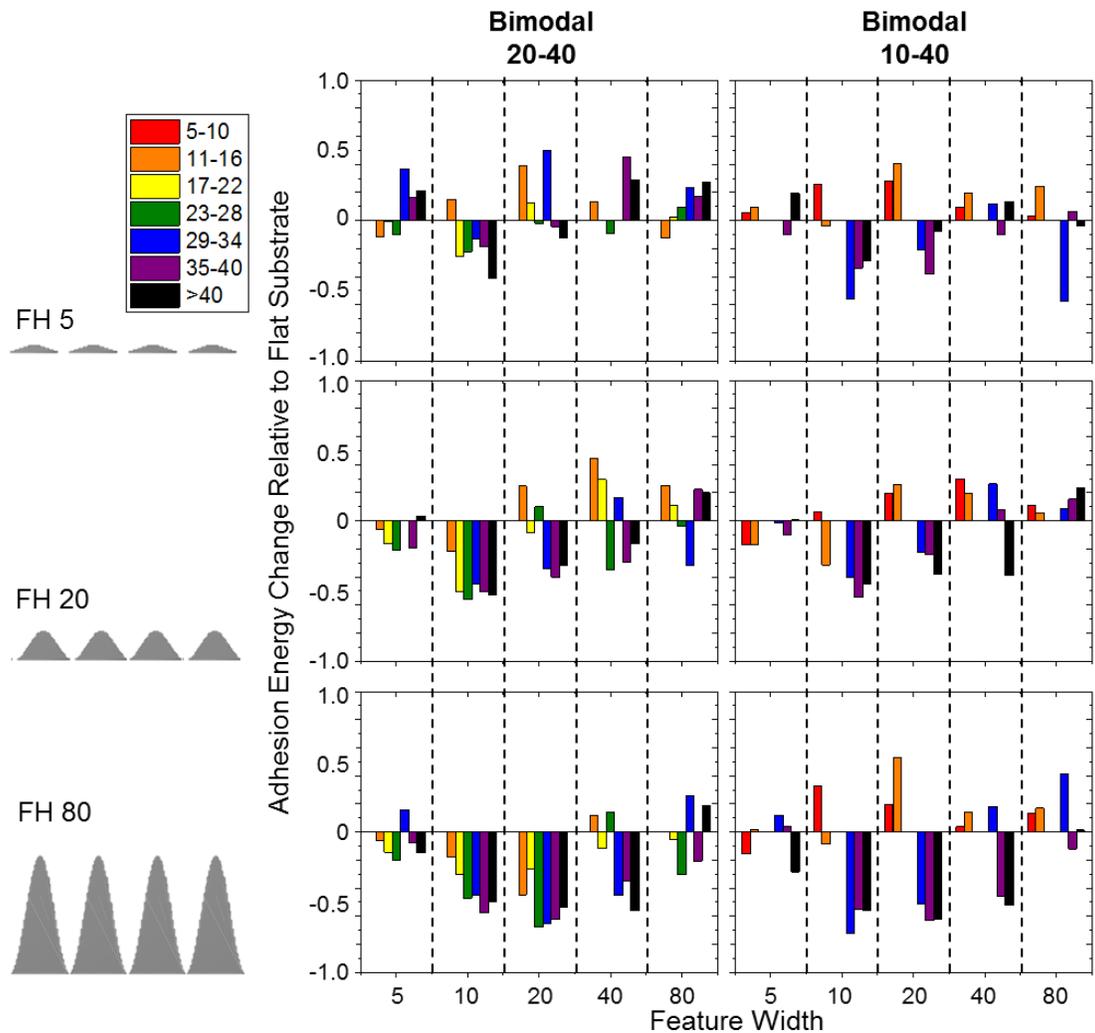


Figure 4.12. Adhesion energies relative to that for flat substrates by particle size (diameter). Column colors correspond to legend for diameter of particles. High amplitude substrates perform best at creating sub-optimal adhesion for particles greater than or equal to the feature width. Large particles sense the substrates as flat for very high and very low feature width. Bimodal 10-20 is more effective at most particle diameters.

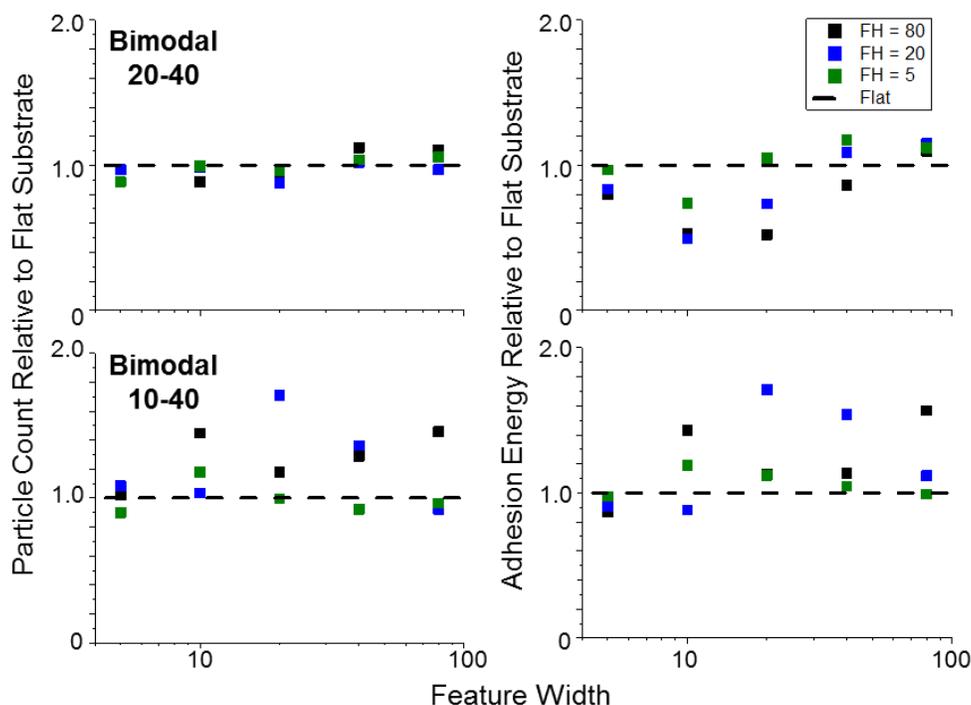


Figure 4.13. Adsorbed particle counts (left column) and adhesion energy (right column) on textured surfaces relative to flat substrates for various feature heights (black 80, blue 20 and green 5). Flat substrate marked by dashed black line at 1. Bimodal 5-20 causes significant problems for textured surfaces above $\lambda = 5$. For $\lambda \leq 20$ bimodal 10-20 is less adhesive to textured surfaces than flat substrates.

4.4 Conclusions

In this study, we explored sinusoidal surfaces' abilities to decrease the adsorption of a monodisperse set of particles as well as the retention of that ability in case of widely distributed particle sizes. Broadening the particle size distribution increased the number of adsorbing particles relative to monodisperse distributions. However, some surfaces where $\lambda/D_{\text{core mean}} < 1$ were still effective in reducing particle adhesion, by lowering number of particles adsorbed and/or adhesion energy, when compared to flat analogues. This efficacy

was highly dependent on feature height for critical feature widths. From this data, surfaces with tall enough features (aspect ratio ≥ 1) reduce the number of surface lattice sites inside the interaction shell between most particles and substrate. There is strong size dependence for adhesion energy, such that particles with $\lambda/D > 1$ adhere stronger than they do to flat surfaces but with $\lambda/D < 1$ adsorb weaker than they do to flat surfaces. At the far extremes of $\lambda/D \gg 1$ and $\lambda/D \ll 1$, we observe that particle adsorption energies are similar to those observed on flat substrates.

Furthermore, we explored the case of a bimodal distribution of particles introduced to the same range of sinusoidal surfaces. It is evident that surface texture can continue to be effective against a moderate size difference (mean particle size ratio of 2) bimodal distribution. However, for large disparities of particle sizes, *i.e.*, mean particle size ratio of 4, the surface textures generally fail to reduce adhesion and adsorption relative to simply using a flat surface. Thus, one would need multiple texture generations or a chemical coating to be properly effective against such bimodal distributions. This finding can assist in the designing of new surface textures given a set of particulates or fouling material sizes. To test the bimodal distributions experimentally, we would design a system of biological or model particles such that their size factor can be varied and allow these particle to settle onto sets of microstructures, analyzing how many of each size adhere. For a biological system, a combination of marine fouling species could be useful. For example diatoms ($\sim 10\text{s } \mu\text{m}$) and barnacle cyprids ($\sim 100\text{s } \mu\text{m}$) could be co-deposited. A model system based on colloidal particles may be more useful as the polydispersity and mean diameter of particles would be easier to control.

4.5 Acknowledgements

This work was supported by the Office of Naval Research under Grant No. N000141210642.

4.6 References

1. Efimenko, K.; Rackaitis, M.; Manias, E.; Vaziri, A.; Mahadevan, L.; Genzer, J. Nested self-similar wrinkling patterns in skins. *Nature Materials* **2005**, *4*, 293-297.
2. Wohl, C. J.; Belcher, M.A.; Chen, L.; Connell, J.W. Laser ablative patterning of copoly(imide siloxane)s generating superhydrophobic surfaces. *Langmuir* **2010**, *26*, 11469-11478.
3. Di Mundo, R.; Nardulli, M.; Milella, A.; Favia, P.; d'Agostino, R.; Gristina, R. Cell adhesion on nanotextured slippery superhydrophobic substrates. *Langmuir* **2011**, *27*, 4914-4921.
4. Zhang, Z.; Chen, S.; Jiang, S. Dual-functional biomimetic materials: Nonfouling poly(carboxybetaine) with active functional groups for protein immobilization. *Biomacromolecules*, **2006**, *7*, 3311-3315.
5. Mrksich, M. A surface chemistry approach to studying cell adhesion. *Chemical Society Reviews* **2000**, *29*, 267-273.
6. Shao, Y.; Fu, J. Integrated Micro/Nanoengineered functional biomaterials for cell mechanics and mechanobiology: A materials perspective. *Advanced Materials* **2014**, *26*, 1494-1533.
7. Tseng, P.; Di Carlo, D. Substrates with patterned extracellular matrix and subcellular stiffness gradients reveal local biomechanical responses. *Advanced Materials* **2014**, *26*, 1242-1247.
8. Yao, X.; Peng, R.; Ding, J. Cell-material interactions revealed via material techniques of surface patterning. *Advanced Materials* **2013**, *25*, 5257-5286.
9. Marino, A.; Ciofani, G.; Filippeschi, C.; Pellegrino, M.; Pellegrini, M.; Orsini, P., Pasqualleti, M.; Mattoli, V.; Mazzolai, B. Two-photon polymerization of sub-micrometric patterned surfaces: Investigation of cell-substrate interactions and improved differentiation of neuron-like cells. *ACS Applied Materials & Interfaces* **2013**, *5*, 13012-13021.
10. Sangeetha, N.M.; Blanck, C.; Nguyen T.T.T., Contal, C.; Mesini, P.J. Size-selective 2D ordering of gold nanoparticles using surface topography of self-assembled diamide template. *ACS Nano* **2012**, *6*, 8498-8507.

11. Bae, W.; Kim, H.N.; Kim, D.; Park, S.; Jeong, H.E.; Suh, K. 25th anniversary article: Scalable multiscale patterned structures inspired by nature: The role of hierarchy. *Advanced Materials* **2014**, *26*, 675-700.
12. Kolewe, M.E.; Park, H.; Gray, C.; Ye, X.; Langer, R.; Freed, L.E. 3D structural patterns in scalable, elastomeric scaffolds guide engineered tissue architecture. *Advanced Materials* **2013**, *25*, 4459-4465.
13. Agarwal, A.; Farouz, Y.; Nesmith, A.P.; Deravi, L.F.; McCain, M.L.; Parker, K.K. Micropatterning alginate substrates for in vitro cardiovascular muscle on a chip. *Advanced Functional Materials* **2013**, *23*, 3738-3746.
14. Hanske, C.; Mueller, M.B.; Bieber, V.; Tebbe, M.; Jessl, S.; Wittemann, A., Fery, A. The role of substrate wettability in nanoparticle transfer from wrinkled elastomers: Fundamentals and application toward hierarchical patterning. *Langmuir* **2012**, *28*, 16745-16750.
15. Snell, K.E.; Stephant, N.; Pansu, R.B.; Audibert, J.; Lagugne-Labarthe, F.; Ishow, E. Nanoparticle organization through photoinduced bulk mass transfer. *Langmuir* **2014**, *i*, 2926-2935.
16. Driscoll, M.K.; Sun, X.; Guven, C.; Fourkas, J.T.; Losert, W. Cellular contact guidance through dynamic sensing of nanotopography. *ACS Nano* **2014**, *8*, 3546-3555.
17. Krishnan, S.; Weinman, C.J.; Ober, C.K. Advances in polymers for anti-biofouling surfaces. *Journal of Materials Chemistry* **2008**, *18*, 3405-3413.
18. Grozea, C.M.; Walker, G.C. Approaches in designing non-toxic polymer surfaces to deter marine biofouling. *Soft Matter* **2009**, *5*, 4088-4100.
19. Chapman, R.; Ostuni, E.; Liang, M.; Meluleni, G.; Kim, E.; Yan, L., Pier, G.; Warren, H.S.; Whitesides, G.M. Polymeric thin films that resist the adsorption of proteins and the adhesion of bacteria. *Langmuir* **2001**, *17*, 1225-1233.
20. Therien-Aubin, H.; Chen, L.; Ober, C K. Fouling-resistant polymer brush coatings. *Polymer* **2011**, *52*, 5419-5425.
21. Gunkel, G.; Weinhart, M.; Becherer, T.; Haag, R.; Huck, W.T.S. Effect of polymer brush architecture on antibiofouling properties. *Biomacromolecules* **2011**, *12*, 4169-4172.
22. Dimitriou, M.D.; Zhou, Z.; Yoo, H.; Killups, K.L.; Finlay, J.A.; Cone, G.; Sundaram, H.S.; Lynd, N.A.; Barteau, K.P.; Campos, L.M.; Fischer, D.A.; Callow, M.E.; Callow, J.A.; Ober, C.K.; Hawker, C.J.; Kramer, E.J.. A general approach to controlling the

- surface composition of poly(ethylene oxide)-based block copolymers for antifouling coatings. *Langmuir* **2011**, *27*, 13762-13772.
23. Zhang, Z.; Chao, T.; Chen, S.; Jiang, S. Superlow fouling sulfobetaine and carboxybetaine polymers on glass slides. *Langmuir* **2006**, *22*, 10072-10077.
 24. Zhang, Z.; Finlay, J.A.; Wang, L.; Gao, Y.; Callow, J.A.; Callow, M.E.; Jiang, S. Polysulfobetaine-grafted surfaces as environmentally benign ultralow fouling marine coatings. *Langmuir* **2009**, *25*, 13516-13521.
 25. Li, G.; Xue, H.; Gao, C.; Zhang, F.; Jiang, S. Nonfouling polyampholytes from an ion-pair comonomer with biomimetic adhesive groups. *Macromolecules* **2010**, *43*, 14-16.
 26. Krishnan, S.; Wang, N.; Ober, C. K.; Finlay, J. A.; Callow, M. E.; Callow, J. A.; Hexemer, A.; Sohn, K. E.; Kramer, E. J.; Fischer, D. A. Comparison of the fouling release properties of hydrophobic fluorinated and hydrophilic PEGylated block copolymer surfaces: Attachment strength of the diatom *Navicula* and the green alga *Ulva*. *Biomacromolecules* **2006**, *7*, 1449-1462.
 27. Koch, K.; Bhushan, B.; Jung, Y.C.; Barthlott, W. Fabrication of artificial lotus leaves and significance of hierarchical structure for superhydrophobicity and low adhesion. *Soft Matter* **2009**, *5*, 1386-1393.
 28. Feng, L.; Li, S.; Li, Y.; Li, H.; Zhang, L.; Zhai, J., Song, Y.; Liu, B.; Kiang, L.; Zhu, D. Super-hydrophobic surfaces: From natural to artificial. *Advanced Materials* **2002**, *14*, 1857-1860.
 29. Sun, M.; Luo, C.; Xu, L.; Ji, H.; Ouyang, Q.; Yu, D., Chen, Y.. Artificial lotus leaf by nanocasting. *Langmuir* **2005**, *21*, 8978-8981.
 30. Berntsson, K.; Andreasson, H.; Jonsson, P.; Larsson, L.; Ring, K.; Petronis, S.; Gatenholm, P.. Reduction of barnacle recruitment on micro-textured surfaces: Analysis of effective topographic characteristics and evaluation of skin friction. *Biofouling* **2000**, *16*, 245-261.
 31. Carman, M.; Estes, T.; Feinberg, A.; Schumacher, J.; Wilkerson, W.; Wilson, L.; Callow, M.; Callow, J.; Brennan, A. Engineered antifouling microtopographies - correlating wettability with cell attachment. *Biofouling* **2006**, *22*, 11-21.
 32. Schumacher, J. F.; Carman, M. L.; Estes, T. G.; Feinberg, A. W.; Wilson, L. H.; Callow, M. E.; Callow, J. A.; Finlay, J. A.; Brennan, A. B. Engineered antifouling microtopographies - effect of feature size, geometry, and roughness on settlement of zoospores of the green alga *Ulva*. *Biofouling* **2007**, *23*, 55-62.

33. Efimenko, K.; Finlay, J.; Callow, M.E.; Callow, J.A.; Genzer, J. Development and testing of hierarchically wrinkled coatings for marine antifouling. *ACS Applied Materials & Interfaces* **2009**, *1*, 1031-1040.
34. Aldred, N.; Scardino, A.; Cavaco, A.; de Nys, R.; & Clare, A.S. Attachment strength is a key factor in the selection of surfaces by barnacle cyprids (*balanus amphitrite*) during settlement. *Biofouling* **2010**, *26*, 287-299.
35. Scardino, A.; Harvey, E.; De Nys, R. Testing attachment point theory: Diatom attachment on microtextured polyimide biomimics. *Biofouling* **2006**, *22*, 55-60.
36. Vasudevan, R.; Kennedy, A.J.; Merritt, M.; Crocker, F H.; Baney, R.H. Microscale patterned surfaces reduce bacterial fouling-microscopic and theoretical analysis. *Colloids and Surfaces B: Biointerfaces* **2014**, *117*, 225-232.
37. Perera-Costa, D.; Bruque, J M.; Gonzalez-Martin, M.; Gomez-Garcia, A.C.; Vellido-Rodriguez, V. Studying the influence of surface topography on bacterial adhesion using spatially organized microtopographic surface patterns. *Langmuir* **2014**, *30*, 4633-4641.
38. Grinthal, A.; Aizenberg, J. Mobile interfaces: Liquids as a perfect structural material for multifunctional, antifouling surfaces. *Chemistry of Materials* **2014**, *26*, 698-708.
39. Schoch, P. K.; Genzer, J. Adsorption of "soft" spherical particles onto sinusoidally-corrugated substrates. *Soft Matter* **2014**, *10*, 7452-7458..
40. Schoch, P. K.; Genzer, J. Adsorption of Multiple Spherical Particles onto Sinusoidally Corrugated Substrates. *Langmuir* **2014**, *30*, 9407-9417.

CHAPTER 5

Marine Fouling on Model Microtextured Surfaces with Tailored Surface Chemistries

Manuscript in preparation:

P.K. Schoch, W. Hoffman, N. Aldred, A. Claire and J. Genzer, 2015.

Marine Fouling on Model Microtextured Surfaces with Tailored Surface Chemistries

Phillip K. Schoch and Jan Genzer*

Department of Chemical and Biomolecular Engineering, North Carolina State University,
Raleigh, North Carolina

Abstract

We discuss our experimental efforts aimed at gaining fundamental understanding of the role of surface topography in reducing marine biofouling, testing and validating our model predictions, and combining chemical coatings with topographical coatings. We begin by selecting a microstructure manufacturing technique, photolithography, which allows us to access the size range of the microorganisms that cause much of the marine biofouling. In this case we desire to study barnacle cyprids, primarily, which are $\sim 100\text{s } \mu\text{m}$ in size. We use the barnacle species *Balanus Amphitrite* as it is known as a model organism for its ability to settle without a biofilm present. We create a set of master molds using a negative photoresist of two aspect ratios (1 and 2) and five feature widths (10, 20, 40, 100, and 200 μm). We then replicate these molds using soft lithography via a commercial silicone elastomer (Sylgard-184) and replicate again the silicone molds into positive replicas by hot embossing them into thermoplastics (polystyrene). We develop a technique termed “thermal reflow” to turn the rectangular profiles created by the photolithography masters into sinusoidal-like profiles as had been tested in our modeling work. Samples of rectangular and sinusoidal profiles are

tested against barnacle cyprids in settlement assays revealing significant reduction in adsorption when the feature width (λ) of our periodic features is just smaller than the cyprids themselves ($\lambda/D_{\text{cyprid}} \sim 0.25-1.0$). This observation coincides with many of our model predictions from Chapters 2-4. Continuing this work, we developed low-fouling polymers in conjunction with a spraycoating delivery method to coat microtextured surfaces. These polymers cross-link to form polymer network gels, thus creating stable coatings. In barnacle cyprid settlement testing, one polymer (betainized poly(4-vinyl pyridine)) only allowed 15% of cyprids to attach. When juvenile cyprids were grown on this same polymer, over 45% were released upon exposure to a 62 kPa impact pressure water jet. This shows promise as both a low-fouling and foul-release coatings to augment our microstructures.

5.1 Introduction

Marine biofouling involves a series of complex processes, by which man-made surfaces become heavily populated with a variety of biological materials, *i.e.*, proteins, bacteria, microorganisms, and eventually macroorganisms. Marine biofouling is a serious problem for naval vessels and man-made surfaces submerged in water as it causes significant reduction in surface performance and increases corrosion. Primarily the issue resides with large roughness being created by populations of microorganisms (clam larvae, barnacle cyprids, and oyster larvae) developing into large (millimeter scale) hard structures on the hulls of naval vessels. For example, barnacles grow from their larval stage (cyprid) $\sim 100\text{s } \mu\text{m}$ to their adult size $\sim 2\text{-}3 \text{ mm}$, an order of magnitude change. This buildup of biofouling increases fuel costs for shipping and increases frequency of dry-docking [1]. Toxic coatings based primarily around biocidal compounds made with transition metals, such as copper or tin, had been used successfully for many years to mitigate this issue. However, this trend has shifted dramatically in recent years due to concerns over the leaching of these metals into local marine biomes with long residence times. In fact, many countries around the world have prohibited ships coated with biocidal materials from entering their harbors [1]. Additionally, there are environmental concerns about the transport of invasive, foreign organisms between different harbors by these shipping vessels. With these concerns in mind, researchers have aimed at developing stable, low-fouling, non-leaching and non-toxic coatings.

The fouling process itself consists primarily of three regimes: 1) the formation of a conditioning film of small molecules, proteins and bacteria onto a substrate prepping the surface for the next stage also known as a biofilm; 2) the adsorption of microorganisms onto the substrate, which yields the final regime; 3) the growth of these microorganisms into large communities and subsequent roughening of the substrate. **Figure 5.1** shows the breakdown of the first two regimes and depicts the design of two possible coating types, *i.e.*, chemical and topographical, for the prevention or obstruction of conditioning films and adsorption of microorganisms, respectively. The past two decades witnessed large activity centered on identifying an optimal chemical coating. A wide variety of surface chemistries has been investigated with varying success. Several chemistries have shown promise over the years including self-ablating chemistry of polyethylene oxides [2-4], low surface energy chemistry of highly fluorinated materials [4] and polydimethylsiloxanes (PDMS) [5], and more recently high surface energy materials based on charged polymers of dual-charge zwitterions [6-8]. Topographical approaches to reduce marine fouling have also been investigated [9-16], but less work has followed this area to create fundamental understanding. Many surfaces shapes and textures in topographically-corrugated surfaces have shown promising results including hierarchical wrinkled substrates [10,11], hexagonal shapes of varying spacing [17], PDMS patterned Sharklet [18,19] and periodically patterned materials [1,9,12-16].

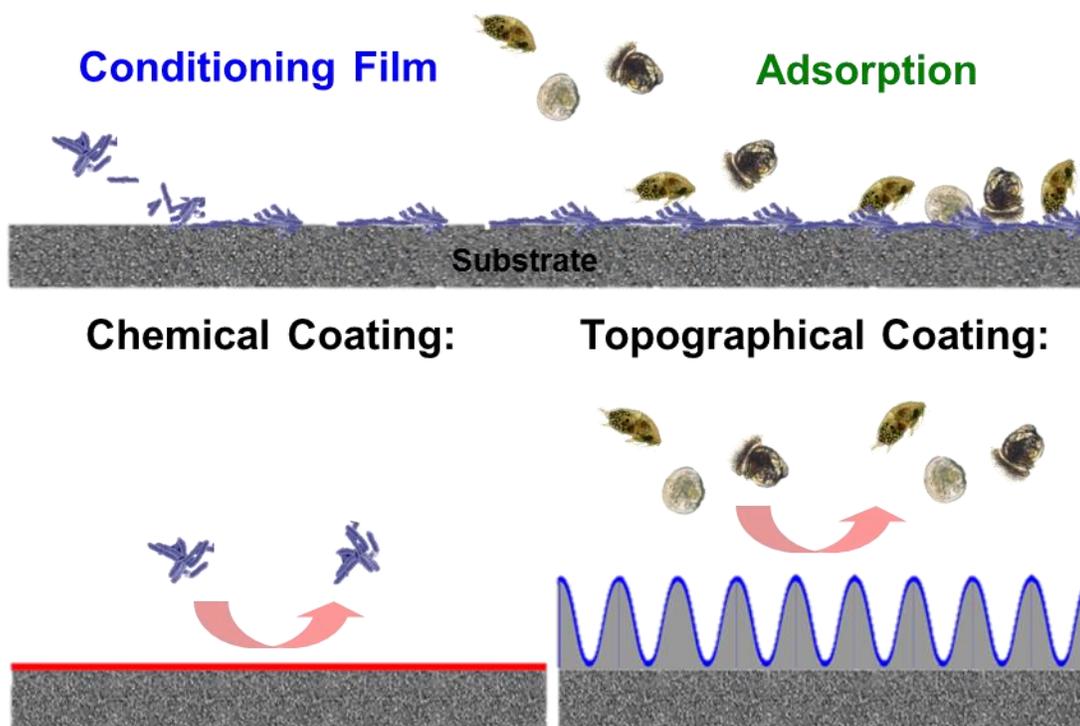


Figure 5.1. Approaches to designing low- and non-fouling surfaces. Chemical coatings typically target the conditioning film, disrupting the adsorption of proteins, small molecules and small marine foulers. Topographical coatings target the biggest problem marine foulers by disrupting the microenvironment they use to settle.

Aldred *et al.* alluded to an adhesion point theory in their work of marine adhesion on periodically patterned substrates [12]. In Chapters 2 and 3 in this Ph.D. Dissertation, we expanded upon this theory with computer simulations covering the adsorption of hairy particles onto sinusoidally corrugated surfaces [20,21]. Chapter 4 expands further on this notion to examine the adsorption of particles with size-polydispersity on sinusoidally-corrugated substrates and comment on the interplay between the sizes of the particles and the dimensions of the surface features (*i.e.*, width and height). In addition to the aforementioned

computer simulation studies, we aim to validate the theoretical predictions with experimental work involving adsorption of marine species (see below) onto manufactured topographically-corrugated substrates with tuned sizes (and to some extent, shapes) of the surface features and tailored surface chemistries. To accomplish these goals, we set out to discover what appropriate technologies are to be used to fabricate these surface topographies over appropriate size scales. Once a technology is settled upon, we test our surfaces against an important biofouling marine organism, barnacle cyprids, with the collaboration of a group at Newcastle University, the UK. We then propose a variety of surface chemistries based on industrially available polymers that can be modified further by using simple post-polymerization reactions and then formed into polymer network gels UV cross-linking. We deliver our surface chemistries via industrially relevant processes to our topographies via a spraycoating process similar to what is currently used in coating ship hulls.

5.2 Experimental Methods

5.2.1 Creation of Microtextured Master Molds

Photomasks were printed by CAD/Art Services, Inc. at various line sizes. SU-8 2010 and 2050 were purchased from Sigma Aldrich. Polished silicon wafers (diameter: 7.5 cm, crystallographic orientation: [1 0 0], p-doped) were used. The SU-8 2000 series comes with a data sheet, provided by Microchem, for proper use and development of the photoresist into microstructures [22]. In a typical process, a wafer is first placed in a dry oven at 120°C for >30 min prior to spincoating. Afterwards, the wafer is placed on a spincoater and ~4 mL of

SU-8 photoresist is added to the center of the wafer. The wafer with the deposited photoresist is then spun according to the directions provided by Microchem to reach desired thickness based on SU-8 viscosity. The photoresist-coated wafer is subsequently placed on a preheated (65°C) hotplate and then transferred to a preheated (90°C) hotplate, times on each plate are a function of photoresist thickness specified by Microchem. After this stage the sample is removed from the hotplate; the photoresist should be “dry” and not sticky. The photomask of choice is then contacted (ink side down) with the surface of the photoresist and the entire assembly is sandwiched between two thick glass plates. Finally, a UV filter is placed atop the top facing glass plate to screen out most wavelengths of UV radiation below 350 nm. This stack of materials is then inserted (face up) under a readied UV flood lamp outputting a spectrum including 365 nm and 254 nm light. The photoresist is subsequently exposed to UV light for a predetermined dosage according to Microchem (150 mJ/cm² for 20 μm thick layer, 250 mJ/cm² for 200 μm thick layer). The wafer is then removed from the glass plate assembly and placed back at 65°C on a hotplate for a post bake followed by 90°C baking on a hotplate. The times for this post-bake treatment were double those suggested by Microchem due to increased stability of microstructures during later steps. The wafer and photoresist are then immersed into a developer solution for washing time directed by Microchem. The resulting material on the wafer should bear the negative image of the photomask with height specified by the spin coat.

5.2.2 Molding and Replication of Masters

Master photoresist molds as created by the procedure outlined in section 5.2.1 are replicated using a poly(dimethylsiloxane) kit from Dow Corning (Sylgard-184). Sylgard-184 is prepared as directed by the manufacturer (10:1 mass ratio of polymer mixture to cross-linker mixture). The entire mixture is degassed under vacuum then flowed over the master mold in a polystyrene Petri dish. This replica is cured at 70°C in an oven for ~1 hour. To avoid breaking the wafer and master mold, the container should be larger than the wafer and the excess Sylgard-184 should be removed before removing the replica and master from the petri dish. Once the master and replica are removed, the replica can be simply peeled away slowly from the master. Any excess Sylgard-184 remaining can be trimmed off. Masters can be replicated many times; ours have remained stable for 10 replications, in this method with care. The Sylgard-184 negative mold is then replicated into a flexible thermoplastic (Polystyrene) to protect the master molds from excessive handling.

5.2.3 Hot Embossing and Reflow of Thermoplastic Molds

Sylgard-184 negative replicas can be used as master molds for thermoplastics to be used as molding materials. A piece (1 in²) of thermoplastic sheet (i.e., polystyrene) is heated at ~150°C, thus above its glass transition temperature, T_g (~105°C), and a weight (2.5 lbs) is placed atop the Sylgard-184 master (1 in²). The thermoplastic flows into the Sylgard-184 mold, assisted by the force due to the weight above to fill all areas of the mold. The thermoplastic and Sylgard-184 are then removed after a period of time (10 min at 150 °C) sufficient for proper replication (dependent on viscosity of PS). The thermoplastic is then

cooled to room temperature before peeling the Sylgard-184 mold off. Occasionally, small imperfections remain in the polystyrene replica. These can be treated by annealing just below the T_g of polystyrene for a period of time. Further, when replicating a column shaped Sylgard-184 mold, the resulting polystyrene replica can be treated with a heat gun for a period of 5 minutes to change the microtexture from columns to sinusoidal shapes as the thermoplastic reflows given sufficient heat and time.

5.2.4 Chemical Modification of Polystyrene and Polyvinyl Pyridines

Polystyrene (PS) obtained from Sigma Aldrich, can be modified to become polystyrene sulfonic acid (PSSa) and subsequently neutralized to polystyrene sulfonate (PSS). This procedure is adopted from [23] using the acetyl sulfate sulfonation method. Initially dry acetic anhydride is mixed with sulfuric acid cooled by an ice bath. The product is acetyl sulfate and acetic acid in a 1:1 ratio along with excess acetic anhydride. In parallel, a solution of PS in 1,2 dichloroethane is prepared. While stirring the PS mixture, the acetyl sulfate mixture is added drop-wise to achieve a 1:1 molar ratio of acetyl sulfate to PS repeat units. Once all of the acetyl sulfate mixture has been added, the reaction mixture is heated at 50°C for time sufficient (2 hours) to achieve large conversion of PS to PSSa (as determined by IR). The resulting PSSa can then be precipitated in cold deionized (DI) water. The PSSa can be further neutralized using a 0.1 M NaOH solution added drop-wise until a neutral pH is achieved thus converting it to PSS.

Poly(2-vinylpyridine) (P2VP) and Poly(4-vinylpyridine) (P4VP) obtained from Polymer Source can be modified by quaternization or betainization reactions to form a

polycation or polyzwitterion, respectively [24,25]. P2VP and P4VP are modified in identical fashion and will be referred to as PVP from here on. For quaternization, a PVP solution is prepared in methanol. Methyl Iodide (Sigma Aldrich) is added in a 1:1 molar ratio to PVP repeat units. This mixture is sealed and placed in a heated bath at 50°C for 12 hours to complete the reaction (as determined by IR) creating quaternized PVP (QPVP). Similarly, for betainization, a PVP solution is prepared in methanol. This solution is then added to 1,3-propane sultone powder. The 1,3-propane sultone and PVP solution are mixed at a 1:1 molar ratio. This mixture is sealed and placed in a heated bath at 50°C for 12 hours to complete the reaction, creating betainized PVP (BPVP). Each resulting modified PVP can be subsequently precipitated in a higher alcohol (butanol or hexanol) before solvating in methanol again if further purification is desired.

5.2.5 Spraycoating of Microtextured Molds

A glass sprayer head was employed to coat microtextured surfaces with parent and modified forms of PS and PVP as well as a PS-co-PVP copolymer. The glass sprayer was connected to a reservoir of polymer solution, hooked up to a source of dry pressurized gas (nitrogen) and placed a set distance (12 inches for MeOH spraycoating) away from the substrate to achieve proper droplet size upon striking the surface. The glass spraycoater used was able to deliver droplets down to 10 μm in diameter upon collision with the substrate, the in-flight diameter is unknown.

5.2.6 Stabilization of Hydrophilic Coatings

Upon spraycoating or spincoating of PS, PVP and their modified forms onto substrates, they are treated using UV light to cross-link them. Samples are placed in a UV/ozone (UVO) chamber using a low-pressure Hg lamp outputting 254 nm and 184 nm light. To avoid ozone formation and excessive degradation of material, the chamber is purged with inert gas (nitrogen or argon) to displace oxygen, essentially treating the polymers with only UV light. Additionally hydrophilic coatings (PSS, QPVP and BPVP) are stabilized using an undercoat of PS that is cross-linked in place beneath the hydrophilic coating. Each coating (PS then modified polymer) receives a specific amount of UV dosage per material and thickness.

5.2.7 Barnacle Cyprid Settlement and Removal Testing

Samples of microtextured materials, spraycoated microtextured materials and flat analogues were submitted to collaborators in the United Kingdom at Newcastle University for testing of marine fouling. Their settlement tests using barnacle cyprids (*Balanus Amphitrite*) involve placing a 1 mL droplet of cyprids in solution over a sample for 48 hours incubated at 28 °C. Numbers of settled cyprids were then counted as a percentage of the total number of cyprids in the droplet. This test is performed in conjunction with a removal assay to analyze the strength of adhesion of a large amount of settled cyprids on the substrates. For this, ~100 cyprids were added to each surface then allowed to settle for 48 hours before the unattached cyprids were removed. At this point, the settled cyprids were cultured for 6 days at room temperature to metamorphosize into juvenile barnacles. The attached barnacles were

then counted on a sample-by-sample basis. Finally, a 62 kPa (impact pressure) water-jet was induced removing weakly attached cyprids. All remaining barnacles were then counted and are expressed in the data as a percentage of the total initial settled amount.

5.3 Results and Discussion

5.3.1 Creating High Quality Microtextures

Prior work pertaining to manufacturing topographically corrugated substrates centered on skin wrinkling behavior of PDMS in particular Sylgard-184 [10,11], a composite material produced by Dow Corning that consists of a PDMS blended with silica particles. That investigation found very high fouling reduction efficacy against a wide variety of marine organisms including barnacle cyprids. These cyprids are the focus of our initial design of substrates and testing the validity of our previously published modeling work [20,21]. Unfortunately, the skin-wrinkling phenomenon used previously does not allow us to access the range of aspect ratios that we tested in the model. Skin wrinkling has been shown to be limited to aspect ratios of ~ 0.16 - 0.20 [10,11]. The aspect ratio is defined as the ratio of the height of a given structure to its width. The skin-wrinkling phenomenon utilizing high strain (30~70%) creates many periodicities all at once in a hierarchical structure whereas we aim to study the periodicity effects systematically. For these reasons, we sought alternative surface fabrication techniques.

Keeping in mind barnacle cyprids sizes (~ 100 s μm), the range of topographies from $10 \mu\text{m}$ to 1 mm was sought. Varieties of technologies exist in the fabrication of small surface

structures (**Figure 5.2**). In this figure, we illustrate a variety of fabrication techniques and their achievable size scales as well as some common marine foulers and their size scales. Electron beam lithography is useful to fabricate small size scales and it takes a relatively long time to fabricate samples with a relatively large area ($>1 \text{ in}^2$). However, this method facilitates creation of substrates with very high aspect ratio of surface structures. On the other end of the spectrum, machining or milling of small parts in plastics and metals is relatively inexpensive and has high control over design. However, these techniques lack the relevant size scales needed for testing our model predictions for marine foulers. Photolithography is a well-known and highly utilized technique for creating a large variety of precise surface structures. By utilizing a negative photoresist (SU-8) one can achieve both a large array of feature widths (100s of nm to 10s of mm) and aspect ratios [26]. This, along with creating large area patterns ($> 1 \text{ in}^2$) and SU-8 being robust mechanically upon curing, made this method an ideal choice for creating master molds of surface topographies.

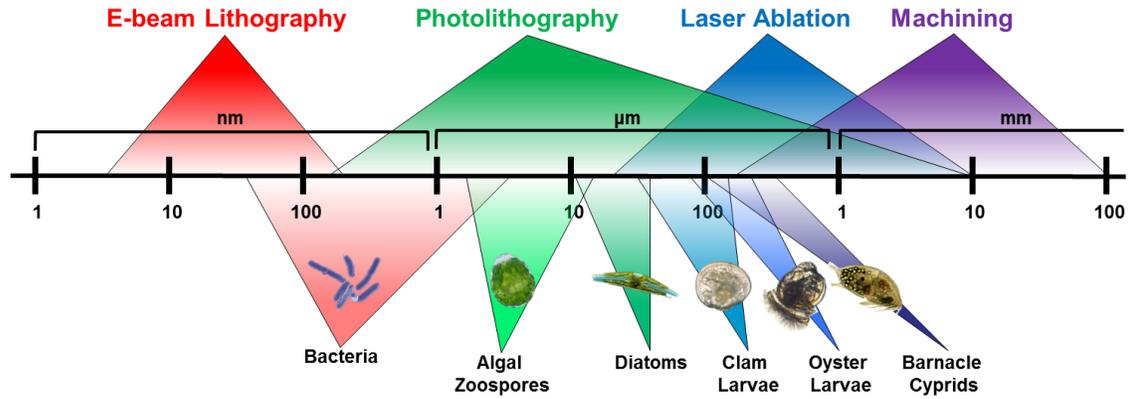


Figure 5.2. Size scale of nano- and micro-structure manufacturing technologies and a selection of marine fouling organisms. Sizes: Electron beam lithography (E-beam) 1s nm – 100s nm; Photolithography 100s nm – 10s μm; Laser ablation 10s μm – 10s mm; Machining/milling 100s μm – 100s mm.

Figure 5.3 provides an overview of the steps involved in creating master mold templates using an SU-8 negative photoresist on silicon wafer. In this process, the photoresist is spincoated to a desired thickness, based on the viscosity of the SU-8 and the spin speed, followed by a baking step wherein solvent is evaporated to prepare for UV light exposure. Once the sample is sufficiently dried, a photomask is applied. Inexpensive photomasks printed on transparencies were purchased with feature sizes ranging from 10 μm to 1 mm. However, creating features with lower sizes required, more expensive chrome on glass photomasks. Next, the system is exposed to 365 nm UV light to initiate the curing of the photoresist. Once cured, the unexposed SU-8 is developed and washed away leaving the desired structures. SU-8 possesses good mechanical properties (high adhesion to silicon

wafer, high modulus (2 GPa), high T_g (210 °C)) according to Microchem [22], which allows it to be replicated several times without significant defects.

To scale up this process we utilized soft lithography to replicate the SU-8 masters. We replicated the master SU-8 ~5 times into Sylgard-184 to obtain fidelity Sylgard-184 masters then hot embossed PS ~5 times off those and in turn, utilized them to make even more Sylgard-184 replicas so that a sufficient number of samples for later testing were available. **Figure 5.4** shows cross-sections and overhead microscope images illustrating the topographies created. These images are collected from Sylgard-184 replicas of the SU-8 master in order to not destroy the master molds. We successfully created several high quality molds in varying sizes. Molds from 10 to 200 μm with aspect ratios of 1 and 2 were created for each size (**Figure 5.4**). This demonstrates the high versatility of our photolithography technique.

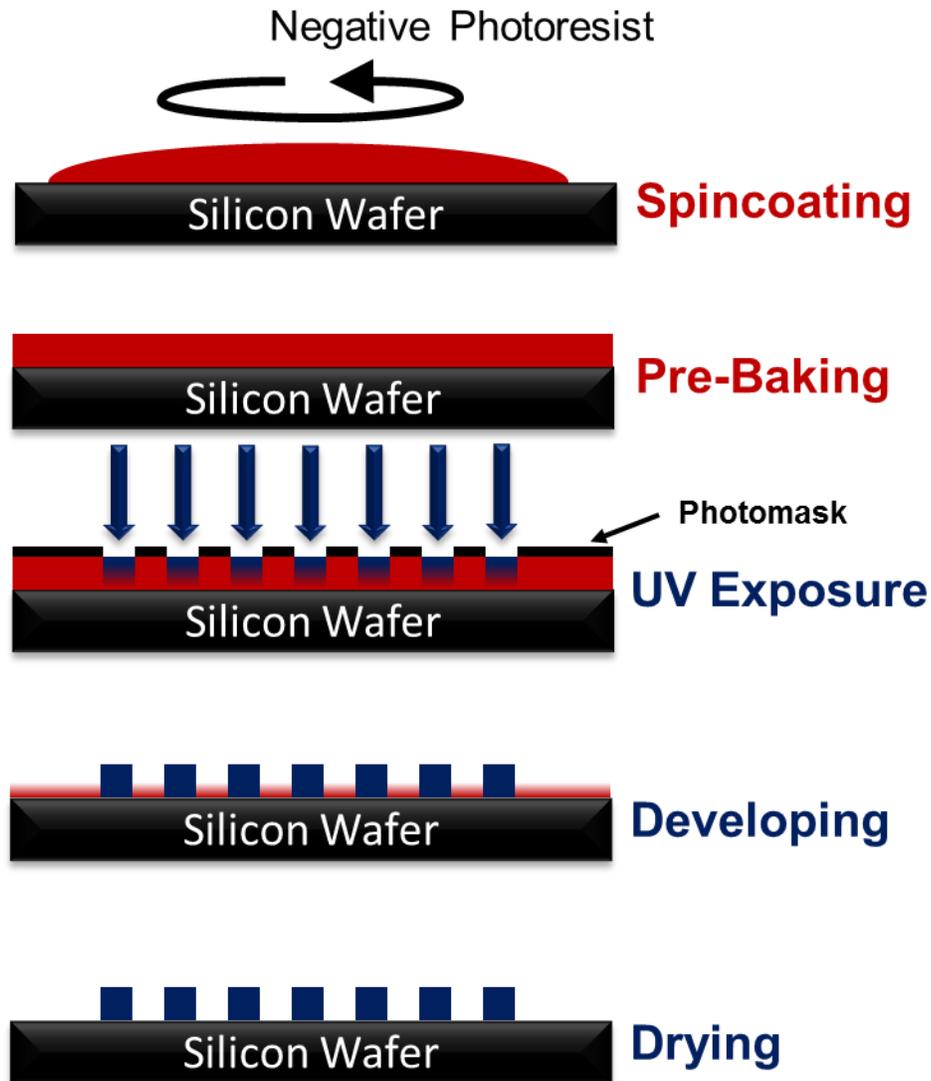


Figure 5.3. Order of operations in developing master molds using negative photoresist photolithography. Negative photoresist (SU-8) is applied to silicon wafer and spincoated to a desired thickness. The resist is then baked to remove solvent and prepare for UV exposure. A photomask is applied followed by exposure to UV light (254 nm) causing cross-linking of the exposed areas of photoresist. After cross-linking the uncured photoresist is removed in a developer solution and dried. Red material indicates un-cross-linked photoresist, Blue indicates cross-linked photoresist.

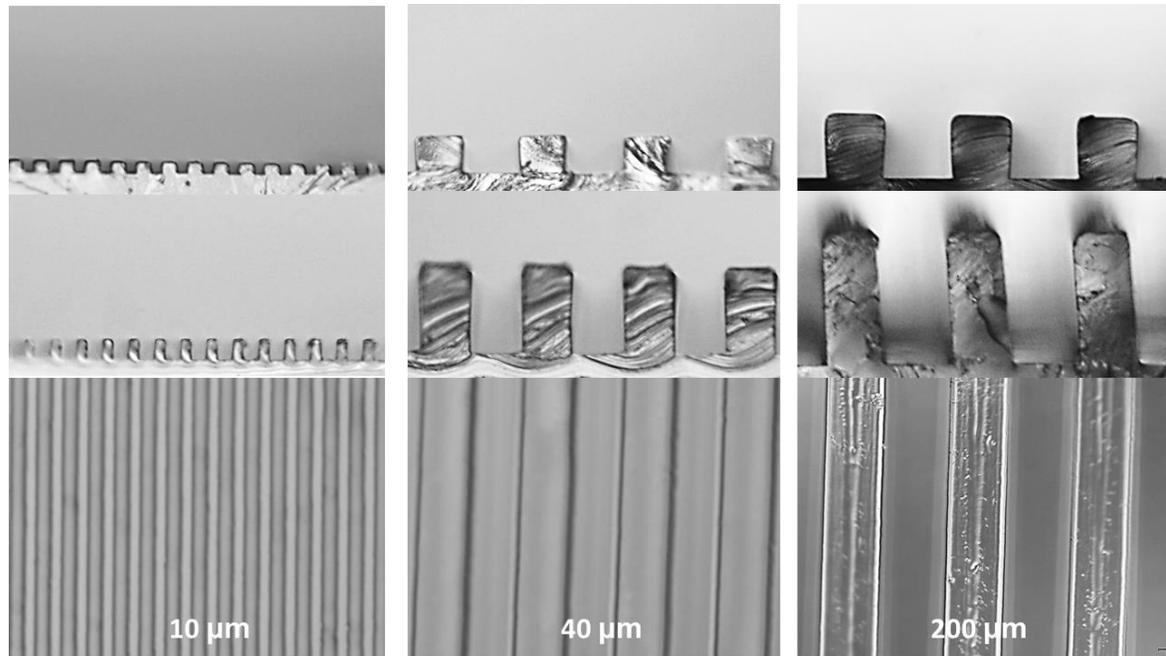


Figure 5.4. Selection of microtopographies created using negative photoresist (SU-8). Images of PDMS (negative) replicas provided. (Top row) Aspect ratio 1 replicas; (Middle row) Aspect ratio 2 replicas; (Bottom row) overhead view of replicas. Columns correspond to feature sizes of 10, 40 and 200 μm respectively.

5.3.2 Effect of Molding with Thermoplastic Materials and Reflowing Polystyrene

The hot embossing process is employed to prepare inexpensive replicas of these surface textures. This allows for high quality replicas to be created quickly and in a thermoplastic polymer (*i.e.*, polystyrene). **Figure 5.5** details the process by which these thermoplastic replicas are made. Using a downward force and heating the thermoplastic (in our case polystyrene) above its T_g , allows the thermoplastic to fill the features of the master mold. In this case, we utilize the Sylgard-184 replicas as masters due to the materials low

surface energy and flexibility. This allows the master to be peeled away with ease when the thermoplastic is cooled back below its T_g as well as allowing for low defect replication.

Hot Embossing

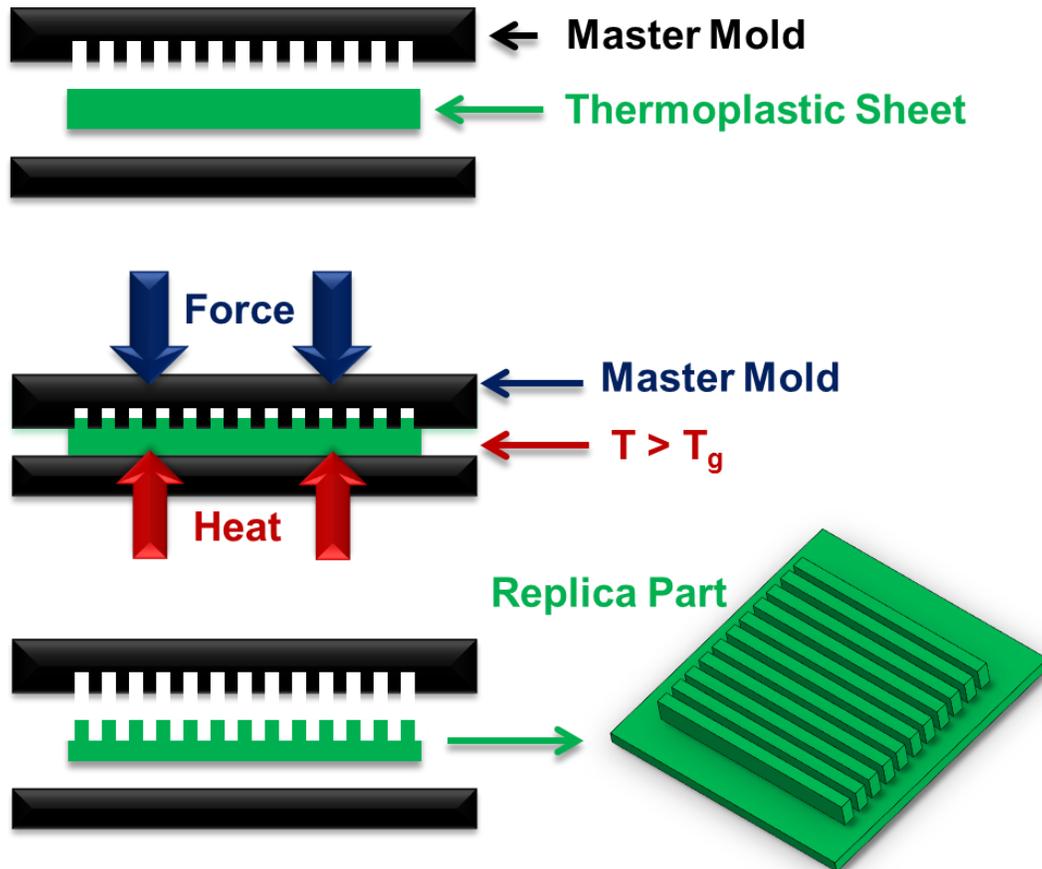


Figure 5.5. Hot embossing procedure to quickly create high quality replicas of master molds. Using a previously made master mold (flexible, low-surface energy material is best), and a sheet of desired thermoplastic a replica is formed. Using downward force on the master and pressing it into the heated ($T > T_g$) thermoplastic (for polystyrene 150°C was used), the thermoplastic fills the master mold. After sufficient time (~10 min), the thermoplastic is cooled then released from the mold revealing the newly created replica part. This process was utilized using Sylgard-184 masters and Polystyrene (thermoplastic) sheet.

The replication of surface texture into a thermoplastic is especially useful as it allows us to transform readily rectangular column structures into near sinusoid shaped structures. Thermal reflow of the thermoplastic replicas yields nearly sinusoidal topographies similar to the topographies explored in Chapters 2-4. The results of this process are detailed in **Figure 5.6**. Cross-sections and overhead images of a set of 35 μm structures are shown. Most of the height of the feature is preserved while changing the rectangular shape to a reflowed smooth wave.

Thermal Reflow

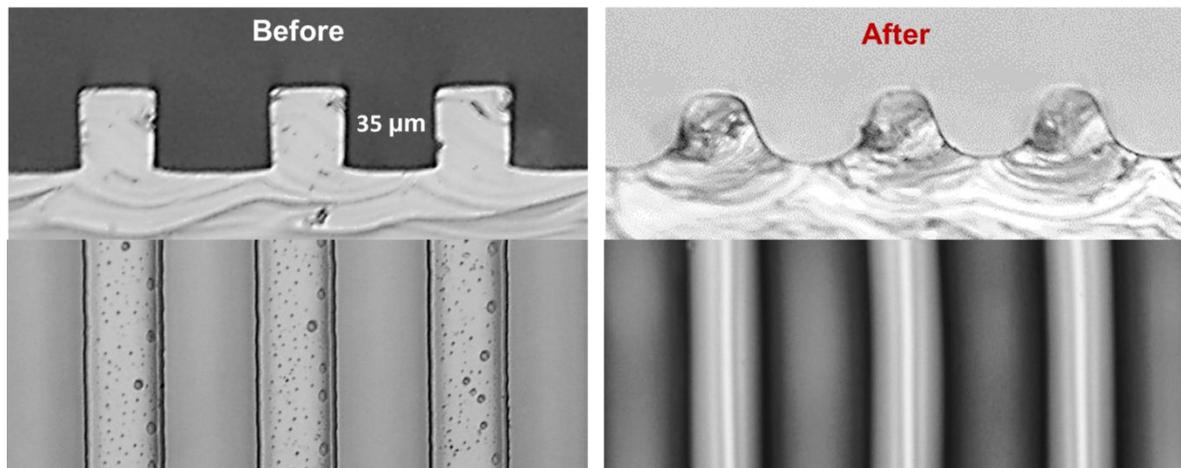


Figure 5.6. Behavior of rectangular column surface features before and after thermal reflow. (Top row) Profile of surface features, (bottom row) overhead view of surface features. Thermal reflow using short time heating (5 min) of surface features above T_g of thermoplastic to transition rectangular surface features into sinusoid-shaped features.

To properly test our model predictions with our fabricated substrates we collaborated with a group at Newcastle University, the UK. Our collaborators run assays on specific species of barnacle cyprids (*Balanus Amphitrite*) detailed in 5.2.7. Cyprid is the larval stage

of the barnacle and occurs while the barnacle is an adolescent free-floating organism that seeks out surfaces in marine environments for suitable locations to settle, grow into an adult barnacle, and finally proliferate. The goal for these substrates is to disrupt the settlement (adsorption) process of the cyprids. Our collaborators utilize an assay of the settlement of a high number of cyprids settling onto a square inch area over 24-48 hours. This assay requires 12 replicas of each substrate condition to determine statistical importance of settlement numbers. **Figure 5.7** shows the results of such an assay upon Sylgard-184 surfaces of both rectangular and sinusoidal surface shapes. At small feature sizes ($< 80 \mu\text{m}$) the settlement behavior is not significantly improved when compared to a flat substrate. However, this changes dramatically at $80 \mu\text{m}$. At this feature width, the model predictions come in to play where the feature size is sub optimal for the settlement of cyprids. Interestingly, the sinusoid substrates at $80 \mu\text{m}$ significantly outperform their rectangular analogues as the sinusoid shows zero cyprid settlement. This may be due to the continuous curvature of the sinusoid versus the flat top surfaces of the rectangular structures. This effect requires further examination, though it does correlate well with our model predictions.

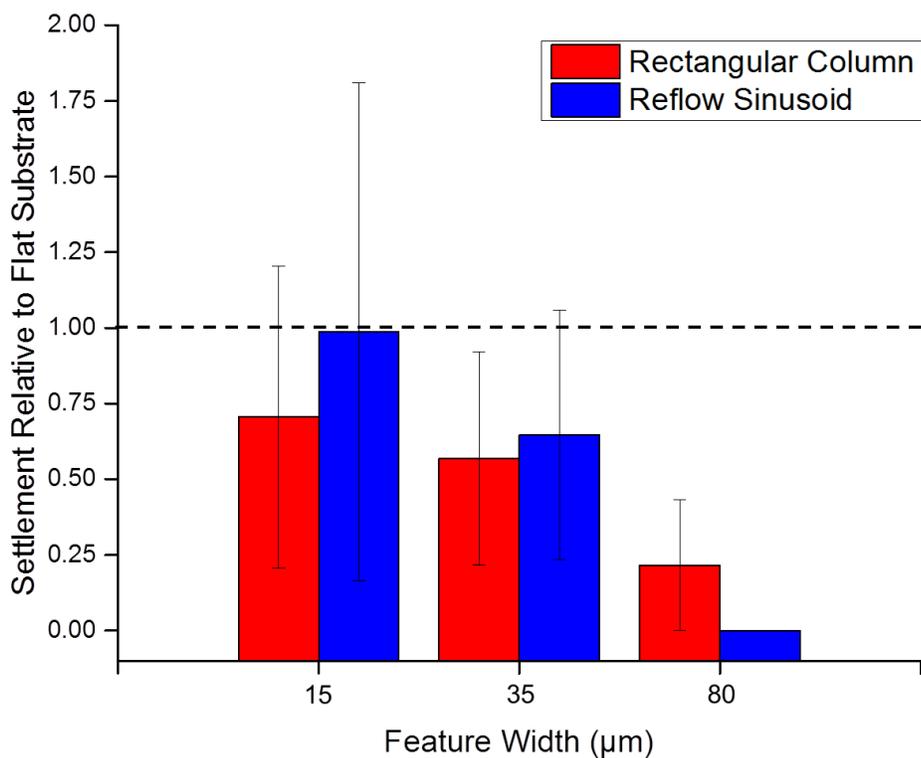


Figure 5.7. Settlement behavior of barnacle cyprids on rectangular columns versus reflowed sinusoids of same dimensions plotted versus width of surface features. Note the y-axis starts below zero to show y-values of zero. Behavior is similar at small dimensions but at 80 μm the sinusoid prevents any cyprids from settling while the columns allow some but show significant improvement over flat substrates. Above the dashed line indicates higher settlement, worse performance, relative to flat substrates. Below the dashed line indicates lower settlement, better performance, relative to flat substrates.

Continuing with work on rectangular substrates at many more feature sizes, we aimed to identify what size the crossover point at which cyprids no longer desired to settle on the surfaces. **Figure 5.8** compares the adsorption of cyprids against surfaces with identical shape and size but different surface chemistries. In the case of Sylgard-184 we observe a drop-off in settlement as the surface feature width nears the size of the cyprids. Interestingly the

higher aspect ratio (2) surfaces for all feature widths show significant reduction of settlement over not only their aspect ratio 1 counterparts but also the flat substrates. Additionally, the surfaces with narrower feature widths of 10 and 20 μm at aspect ratio 1 attract more cyprids than flat substrates of the same surface chemistry.

Collapsing the result of cyprid settlements for all of surface textures studied onto a single plot leads to data shown in **Figure 5.9**. Here the relative settlement behavior of barnacle cyprids on surfaces of varying surface chemistry is scaled to their respective flat substrate analogues. In **Figure 5.9**, features greater than 70 μm show significant reduction of cyprid settlement with the exception of one sample set at 100 μm . This behavior is in agreement with predictions from our simulation model predictions; namely, that the space between features (feature width or λ) is a critical factor influencing settlement of fouling organisms.

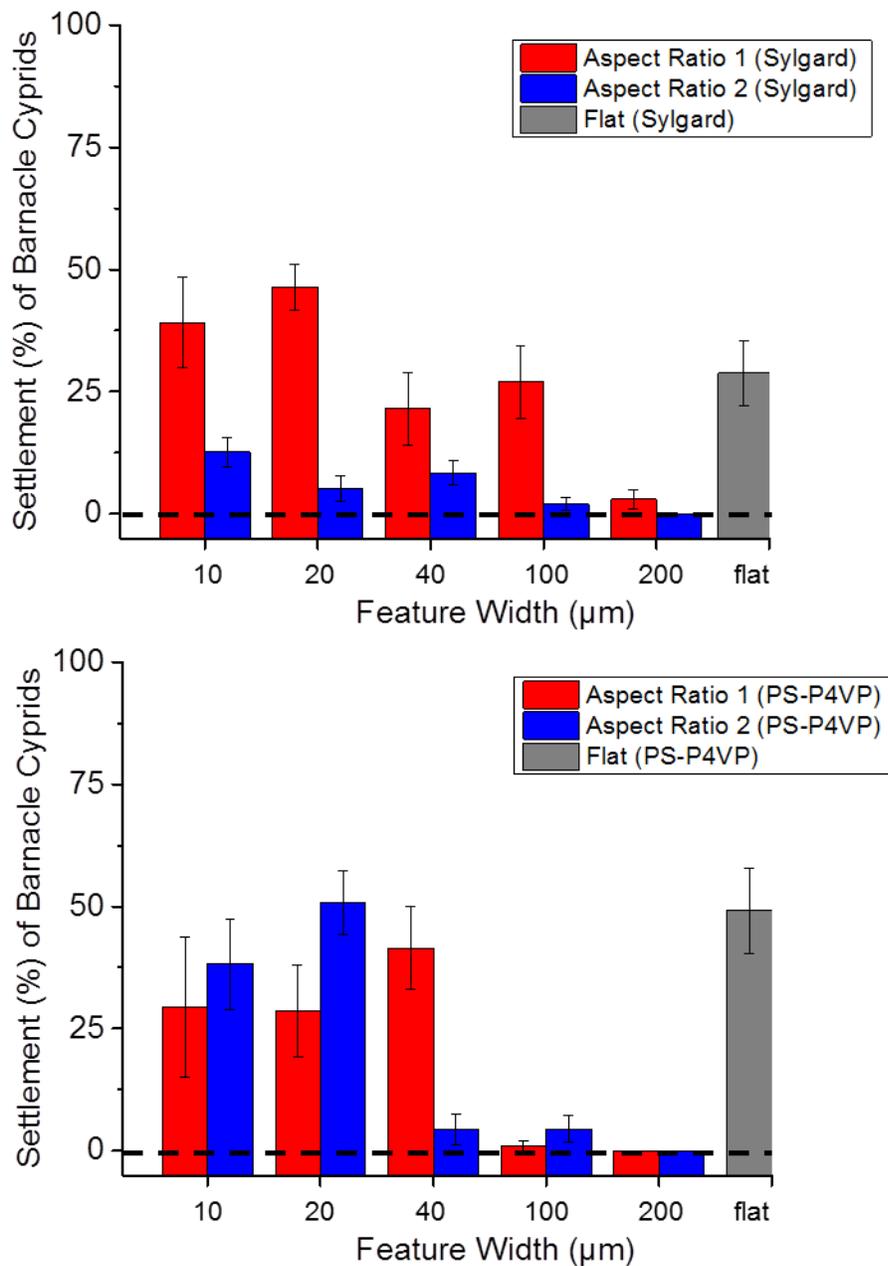


Figure 5.8. Behavior of barnacle cyprid settlement on identical surface structures with differing surface chemistries. (Top) Sylgard-184 surface features show strong dependence of settlement on surface feature dimensions, specifically higher aspect ratio surfaces perform much better across all sizes, including zero settlement at 200 μm. (Bottom) PS-P4VP coated surfaces show similar settlement below 100 μm but a significant drop-off is observed above 100 μm, including zero settlement at 200 μm for both aspect ratios.

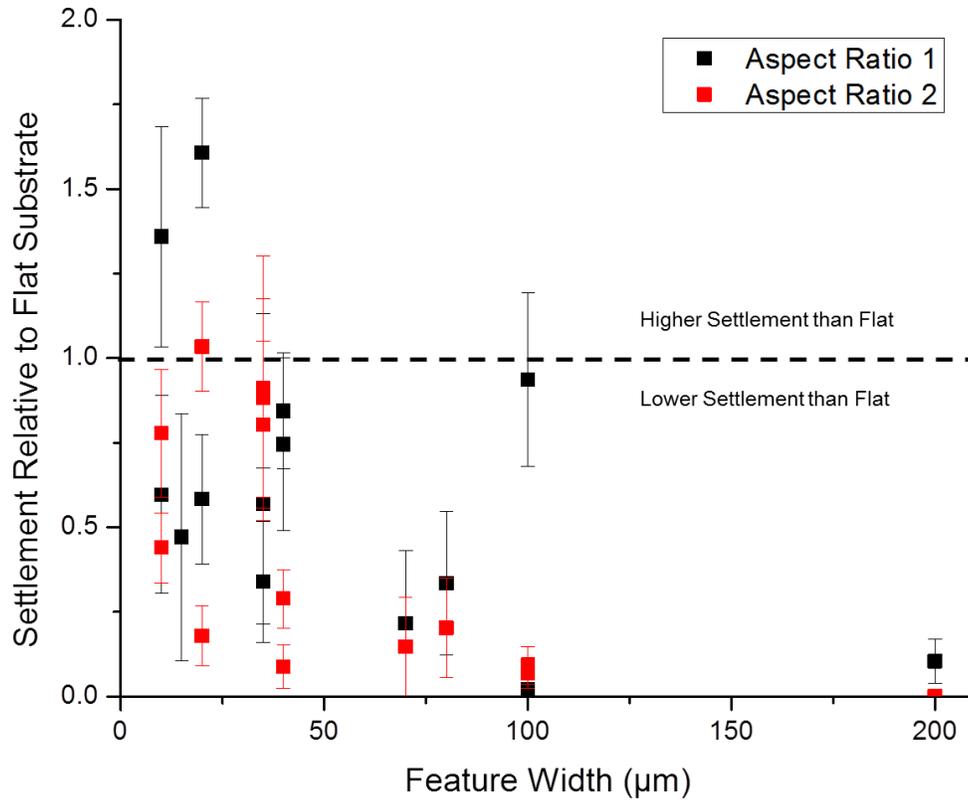


Figure 5.9. Results of extensive testing of topographically-corrugated samples with barnacle cyprid settlement assays. Relative settlement behavior, independent of surface chemistry, of various sized topographies is plotted as a function of the surface feature sizes. Improvement over flat surface analogues is seen for most surfaces around 70 μm for both aspect ratios and for all samples greater than 100 μm. Above the dashed line indicates higher settlement, worse performance, relative to flat substrates. Below the dashed line indicates lower settlement, better performance, relative to flat substrates.

5.3.4 Modification of Microtexture Surface Chemistry via Polystyrene and Polyvinyl Pyridine Derivatives

The data in **Figure 5.8** (bottom) show the performance of results from a coating made of a random copolymer of polystyrene and poly (4-vinylpyridine), PS-co-P4VP, purchased from Sigma Aldrich. The data in **Figure 5.8** suggest that this copolymer surface chemistry is more attractive to cyprids in flat geometry than Sylgard-184. When the surfaces reach a critical size (100 μm), in both aspect ratios, the cyprids do not settle. In fact, at feature width of 200 μm and both aspect ratios tested, no cyprids were observed to have settled. This material was chosen due to the ability of both PS and P4VP to undergo a variety of modification reactions as well as a cross-linking reaction occurring through their backbones. This surface chemical coating was deposited on the substrates using a spraycoating process similar to that which the ship painting industry currently uses. We aim to further develop this surface chemistry to augment the anti-fouling characteristics of the surface topographies by modifying the copolymer to become a polyzwitterion, polycation and/or polyanion.

Polystyrene and polyvinyl pyridines are unique due to their ability to undergo cross-linking via UV-light (254 nm) through their polymer backbones [27-30]. This allows them to both adhere well to substrates and form polymer network gels, for a more stable anti-fouling system. Additionally such coatings can undergo a variety of post-polymerization reactions to become charged materials. Polystyrene becomes polystyrene sulfonate (PSS) when exposed to a sufficiently strong sulfonating agent, such as acetyl sulfate or sulfuric acid [23]. This endows polystyrene with a sulfonyl group that is negatively charged. Polyvinyl pyridines, P2VP and P4VP, can become positively charged or zwitterionic when undergoing

quaternization or betainization reactions respectively [24,25]. Quaternization utilizes an alkyl halide, such as methyl iodide, to induce a pH independent positive charge on the nitrogen of the pyridyl ring (QP2VP and QP4VP). Betainization occurs in the presence of alkyl sultone compounds, such as 1,3-propane sultone, which undergoes ring opening followed by reaction with the nitrogen of the pyridyl ring (BP2VP and BP4VP). Thus, a positive charge is created at the nitrogen and a negative charge exists at the sulfonyl group. See supplemental information for IR spectra and reaction schemes for each reaction.

These modified polymers are then deposited onto textured surfaces via spraycoating (*cf.* **Figure 5.10**). As mentioned earlier, spraycoating is chosen specifically due to its application in commercial coating processes that are used to paint ship hulls. As shown in **Figure 5.10**, we achieved conformal surface coatings across a variety of different surface chemistries. The spraycoating process is followed by UV cross-linking the polymers to stabilize the new chemical coating onto the substrate and to form surface-attached-networks. This stabilization is enhanced by first depositing a thin layer of PS primer onto the substrate of interest, and crosslinking it, before spraycoating the functional coating layer as illustrated in **Figure 5.11**. The ability to coat hydrophobic surfaces with stable hydrophilic coatings as documented by monitoring the water contact angles after 2 weeks submersion in artificial seawater. Images in **Figure 5.11** show the coating remaining after the 2 weeks of submersion.

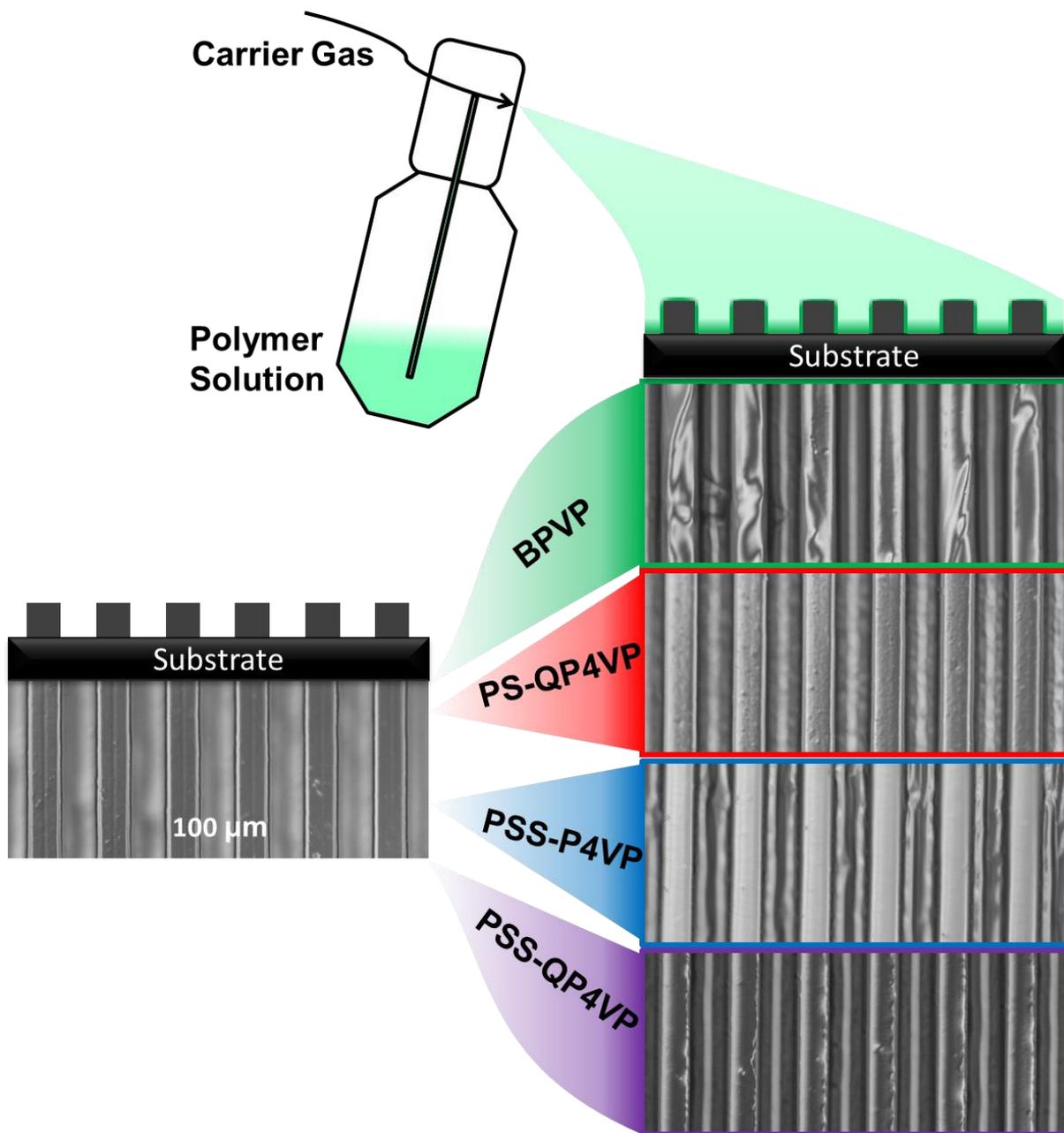


Figure 5.10. Topographically-corrugated sample surface chemistry modified via spraycoating with a variety of modified polymers forming conformal coatings. A polymer solution prepared in (relatively) volatile solvent is sprayed directly onto substrates yielding modified surface chemistries of the topographies.

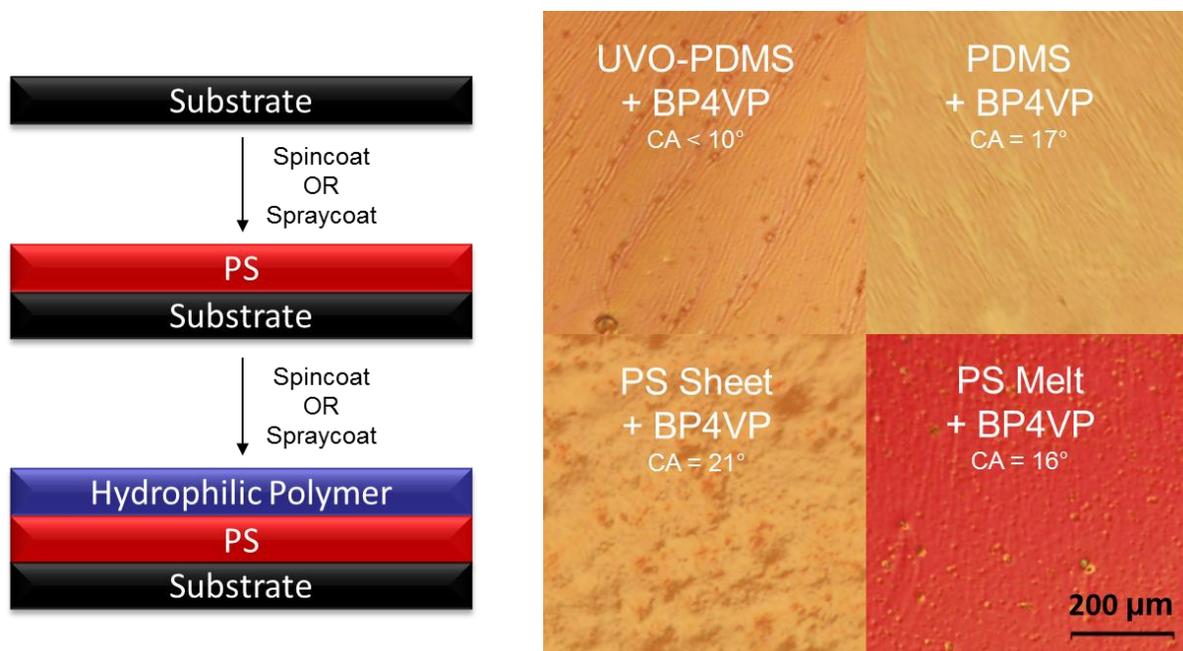


Figure 5.11. Utilizing modified polymers the surface chemistry including surface energy and contact angle can be changed dramatically. (Left) Procedure to stabilize hydrophilic polymers to variety of substrate materials (PDMS, UVO-PDMS, PS sheet, PS melt). (Right) Substrate materials shown with application of BP4VP after 2 weeks submersion in artificial seawater.

These surface chemistries, in flat geometries, were supplied to our collaborators in the UK for settlement and removal testing for barnacle cyprids (*Balanus Amphitrite*) detailed in 5.2.7. These cyprids are unique in that they will settle on surfaces without a biofilm present [1], so they are particularly useful for model surfaces. Samples were prepared on glass slides with a variety of surface chemistries. Of particular interest are the betainized P4VP (BP4VP) and P2VP (BP2VP) cross-linked films (*cf.* **Figure 5.12**). Their settlement percentages are reported and show low settlement (10-15%) of the barnacle cyprids. Polystyrene is used as a control here as cyprids tend not to settle on hydrophobic surfaces. That makes this result

interesting since the betainized surfaces have very low water contact angles ($< 20^\circ$) compared to the hydrophobic polystyrene (90°). A separate batch of samples underwent the barnacle removal assay. In this assay, the cyprids were allowed to grow on the substrates for 6 days to metamorphosize into juvenile barnacles after which they were exposed to a 62 kPa impact pressure water jet. Remaining juvenile barnacles were counted and are reported as percent removal compared to the settled amount. Sylgard-184 is a useful benchmark for removal behavior as it releases cyprids easily (*cf.* **Figure 5.12**). Notice the BP4VP samples also release the cyprids well (~45%), within error of how well cyprids release off Sylgard-184. We believe that this is due to the high hydrophilicity of the BP4VP zwitterion, binding water tightly such that other materials are not able to attach strongly. Therefore, not only do the barnacle cyprids not settle strongly, but also many of the cyprids that do attach and develop into juvenile barnacles can be washed away using low pressure (62 kPa impact pressure) water. This makes BP4VP a promising candidate for coating the already low-fouling surface textures.

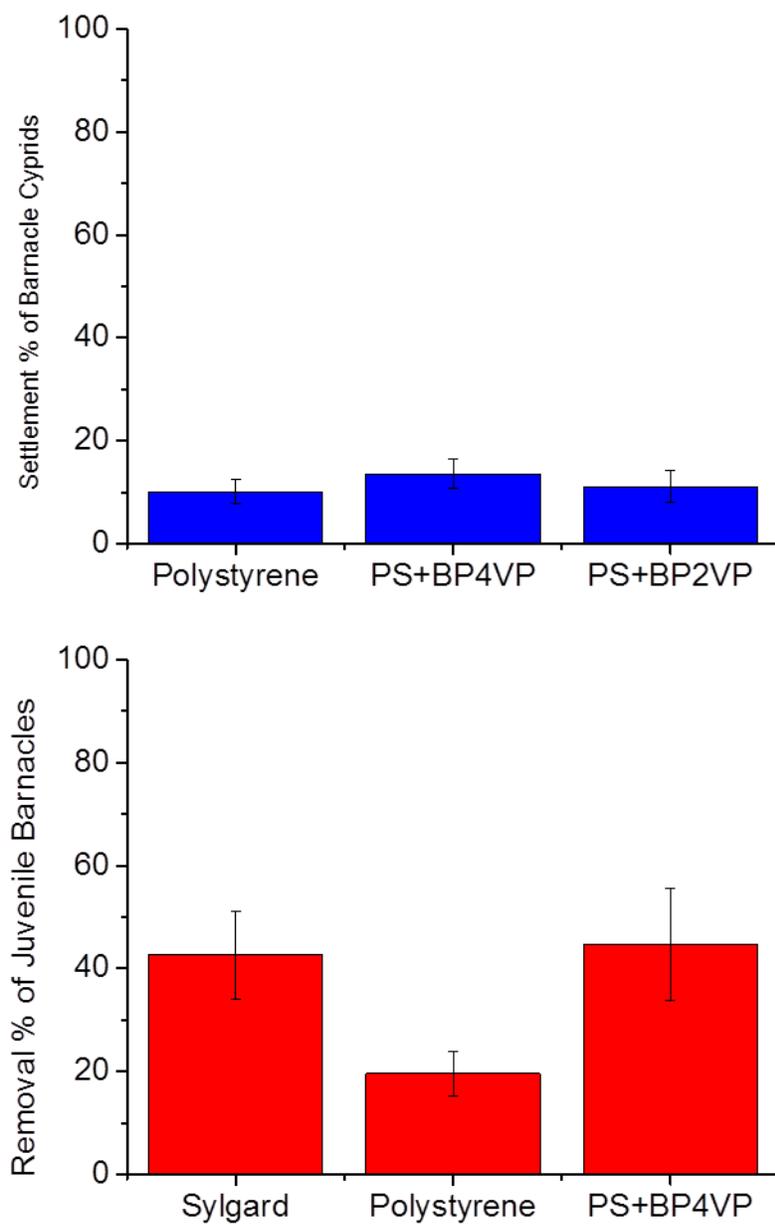


Figure 5.12. (Top) Settlement % (blue columns) of 3-day old *B. Amphitrite* cyprids larvae on the test surfaces after 24 h. (Bottom) Removal % (red columns) of 6-day old juvenile barnacles (*B. Amphitrite*) from the test surfaces using a water jet with a calibrated impact pressure of 62 kPa.

5.4 Conclusions

We have successfully developed several important technologies towards reducing marine fouling as well as worked to validate predictions of our model. Initially we utilized photolithography to make high quality microtextures that we could then replicate using soft lithography. Hot embossing into thermoplastic (polystyrene) successfully scaled this up further by allowing the creation of dozens of near identical replicas. This polystyrene was reflowed into sinusoid geometries and both sinusoids and columnar structures. These structures featured surface dimensions (widths) from 10-200 μm and aspect ratios (i.e., height/width of the surface features) of 1-2. Samples of these structures underwent barnacle cyprid assays in collaboration with Newcastle University, the UK. This testing revealed low settlement minima with respect to feature spacing of half the size of the cyprids. This result was very similar to that of our model established in previous publications [20,21]. In addition to studying surface topography, we successfully developed a variety of hydrophilic polymers capable of forming polymer network gels. Furthermore, these polymers can be deployed by spraycoating to modify the interface of our newly created surface topographies. Some of these new surface chemistries, betainized P4VP in particular, showed success against barnacle cyprids upon settlement (~15% settlement) and removal (~45% removal) testing. This makes it a good candidate to act as both a low-fouling and foul-release coating.

5.5 Acknowledgements

This work was supported by the Office of Naval Research under Grant No. N000141210642.

5.6 References

1. Grozea, C.M.; Walker, G.C. Approaches in designing non-toxic polymer surfaces to deter marine biofouling. *Soft Matter* **2009**, *5*, 4088-4100.
2. Krishnan, S.; Weinman, C.J.; Ober, C.K. Advances in polymers for anti-biofouling surfaces. *Journal of Materials Chemistry* **2008**, *18*, 3405-3413.
3. Dimitriou, M.D.; Zhou, Z.; Yoo, H.; Killops, K.L.; Finlay, J.A.; Cone, G.; Sundaram, H.S.; Lynd, N.A.; Barteau, K.P.; Campos, L.M.; Fischer, D.A.; Callow, M.E.; Callow, J.A.; Ober, C.K.; Hawker, C.J.; Kramer, E.J.. A general approach to controlling the surface composition of poly(ethylene oxide)-based block copolymers for antifouling coatings. *Langmuir* **2011**, *27*, 13762-13772.
4. Krishnan, S.; Wang, N.; Ober, C. K.; Finlay, J. A.; Callow, M. E.; Callow, J. A.; Hexemer, A.; Sohn, K. E.; Kramer, E. J.; Fischer, D. A. Comparison of the fouling release properties of hydrophobic fluorinated and hydrophilic PEGylated block copolymer surfaces: Attachment strength of the diatom *Navicula* and the green alga *Ulva*. *Biomacromolecules* **2006**, *7*, 1449-1462.
5. Yebra, D.; Kiil, S.; Dam-Johansen, K. Antifouling technology - past, present and future steps towards efficient and environmentally friendly antifouling coatings. *Prog. Org. Coat.* **2004**, *50*, 75-104.
6. Zhang, Z.; Chao, T.; Chen, S.; Jiang, S. Superlow fouling sulfobetaine and carboxybetaine polymers on glass slides. *Langmuir* **2006**, *22*, 10072-10077.
7. Zhang, Z.; Finlay, J.A.; Wang, L.; Gao, Y.; Callow, J.A.; Callow, M.E.; Jiang, S. Polysulfobetaine-grafted surfaces as environmentally benign ultralow fouling marine coatings. *Langmuir* **2009**, *25*, 13516-13521.
8. Li, G.; Xue, H.; Gao, C.; Zhang, F.; Jiang, S. Nonfouling polyampholytes from an ion-pair comonomer with biomimetic adhesive groups. *Macromolecules* **2010**, *43*, 14-16.
9. Berntsson, K.; Andreasson, H.; Jonsson, P.; Larsson, L.; Ring, K.; Petronis, S.; Gatenholm, P.. Reduction of barnacle recruitment on micro-textured surfaces: Analysis of effective topographic characteristics and evaluation of skin friction. *Biofouling* **2000**, *16*, 245-261.
10. Efimenko, K.; Rackaitis, M.; Manias, E.; Vaziri, A.; Mahadevan, L.; Genzer, J. Nested self-similar wrinkling patterns in skins. *Nature Materials* **2005**, *4*, 293-297.

11. Efimenko, K.; Finlay, J.; Callow, M.E.; Callow, J.A.; Genzer, J. Development and testing of hierarchically wrinkled coatings for marine antifouling. *ACS Applied Materials & Interfaces* **2009**, *1*, 1031-1040.
12. Aldred, N.; Scardino, A.; Cavaco, A.; de Nys, R.; & Clare, A.S. Attachment strength is a key factor in the selection of surfaces by barnacle cyprids (*balanus amphitrite*) during settlement. *Biofouling* **2010**, *26*, 287-299.
13. Scardino, A.; Harvey, E.; De Nys, R. Testing attachment point theory: Diatom attachment on microtextured polyimide biomimics. *Biofouling* **2006**, *22*, 55-60.
14. Vasudevan, R.; Kennedy, A.J.; Merritt, M.; Crocker, F H.; Baney, R.H. Microscale patterned surfaces reduce bacterial fouling-microscopic and theoretical analysis. *Colloids and Surfaces B: Biointerfaces* **2014**, *117*, 225-232.
15. Perera-Costa, D.; Bruque, J M.; Gonzalez-Martin, M.; Gomez-Garcia, A.C.; Vellido-Rodriguez, V. Studying the influence of surface topography on bacterial adhesion using spatially organized microtopographic surface patterns. *Langmuir* **2014**, *30*, 4633-4641.
16. Grinthal, A.; Aizenberg, J. Mobile interfaces: Liquids as a perfect structural material for multifunctional, antifouling surfaces. *Chemistry of Materials* **2014**, *26*, 698-708.
17. Xiao, L.; Thompson, S. E. M.; Roehrig, M.; Callow, M. E.; Callow, J. A.; Grunze, M.; Rosenhahn, A. Hot Embossed Microtopographic Gradients Reveal Morphological Cues That Guide the Settlement of Zoospores. *Langmuir* **2013**, *29*, 1093-1099.
18. Carman, M.; Estes, T.; Feinberg, A.; Schumacher, J.; Wilkerson, W.; Wilson, L.; Callow, M.; Callow, J.; Brennan, A. Engineered antifouling microtopographies - correlating wettability with cell attachment. *Biofouling* **2006**, *22*, 11-21.
19. Schumacher, J. F.; Carman, M. L.; Estes, T. G.; Feinberg, A. W.; Wilson, L. H.; Callow, M. E.; Callow, J. A.; Finlay, J. A.; Brennan, A. B. Engineered antifouling microtopographies - effect of feature size, geometry, and roughness on settlement of zoospores of the green alga *Ulva*. *Biofouling* **2007**, *23*, 55-62.
20. Schoch, P. K.; Genzer, J. Adsorption of "soft" spherical particles onto sinusoidally-corrugated substrates. *Soft Matter* **2014**, *10*, 7452-7458.
21. Schoch, P. K.; Genzer, J. Adsorption of Multiple Spherical Particles onto Sinusoidally Corrugated Substrates. *Langmuir* **2014**, *30*, 9407-9417.

22. SU-8 2000 series Data Sheet. Retrieved May 10, **2015**, from http://www.microchem.com/pdf/SU-82000DataSheet2000_5thru2015Ver4.pdf
23. Kucera, F.; Jancar, J. Homogeneous and heterogeneous sulfonation of polymers: A review. *Polym. Eng. Sci.* **1998**, *38*, 783-792.
24. Song, L.; Lam, Y. Selective betainization of PS-P4VP and solution properties. *Langmuir* **2006**, *22*, 319-324.
25. Boucher, E.; Khosravibabadi, E. Kinetics and Mechanism of the Quaternization of Poly(4-Vinyl Pyridine) with Alkyl Iodides. *Journal of the Chemical Society-Faraday Transactions i* **1983**, *79*, 1951-1958.
26. del Campo, A.; Greiner, C. SU-8: a photoresist for high-aspect-ratio and 3D submicron lithography. *J Micromech Microengineering* **2007**, *17*, R81-R95.
27. Knudsen, D.; Harnish, B.; Toth, R.; Yan, M. Creating Microstructures on Silicon Wafers Using UV-Crosslinked Polystyrene Thin Films. *Polym. Eng. Sci.* **2009**, *49*, 945-948.
28. Yan, M.; Harnish, B. A simple method for the attachment of polymer films on solid substrates. *Adv Mater* **2003**, *15*, 244-+.
29. Harnish, B.; Robinson, J.; Pei, Z.; Ramstrom, O.; Yan, M. UV-cross-linked poly(vinylpyridine) thin films as reversibly responsive surfaces. *Chem. Mat.* **2005**, *17*, 4092-4096.
30. Yousif, E.; Haddad, R. Photodegradation and photostabilization of polymers, especially polystyrene: review. *SpringerPlus* **2013**, *2*, 398.

Supplemental Information

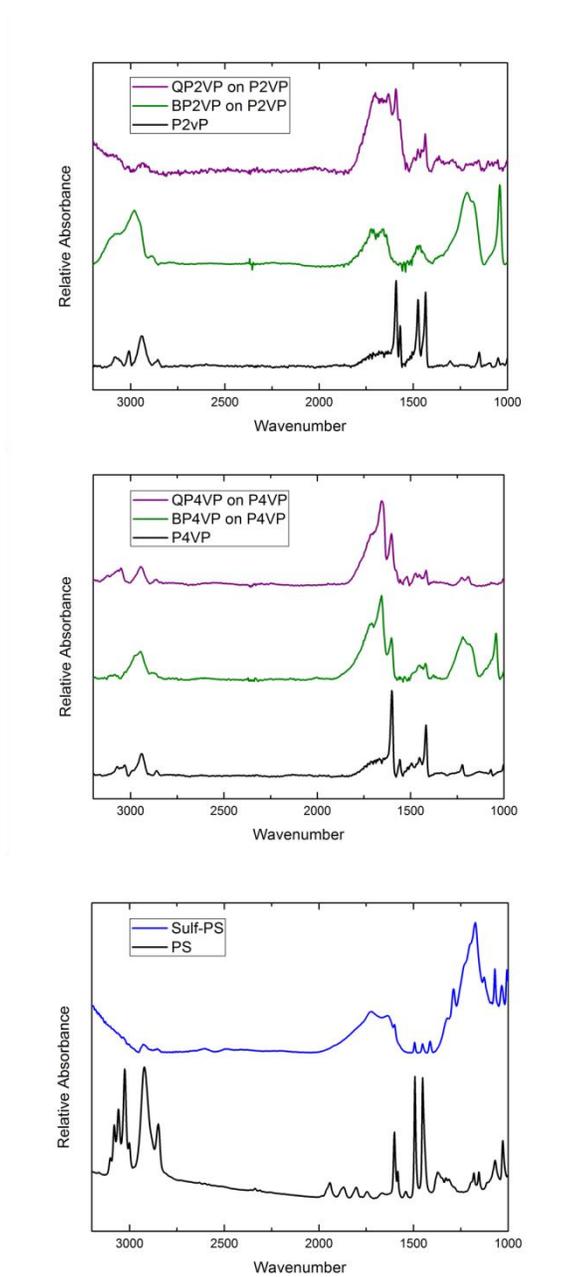


Figure 5.S1. IR spectra for quaternization and betainization of P2VP and P4VP. IR spectra for sulfonation of PS.

CHAPTER 6

Outlook

6.1 Outlook

This Ph.D. Dissertation has contributed to improving understanding the fundamentals of using substrate topography to combat non-specific adhesion of particles and marine microorganisms using both experimental efforts and via computer simulations. Chapters 2 and 3 explored utilization of monodisperse spherical particles, simulated as either polymer-coated “sticky” spheres or core-shell spheres, as model foulers to gain insight into the relationship between particle size and feature width and feature height of periodic surface structures comprising sinusoidally-corrugated topographies. Chapter 4 challenged the effectiveness of single feature widths of periodic surface structures by introducing adhesive particles with polydispersity in sizes. In particular, we explored how well such feature widths, optimized to a specific particle diameter, perform against distributions of smaller and much larger particles. Finally, Chapter 5 discussed our progress in creating such microstructures experimentally as well as methods to replicate these structures in high volume with low defect counts. Chapter 5 also introduced a method to coat such microstructures with low-fouling/foul-release surface chemistries in a similar technology, spraycoating, used by the current ship paint industry. The goal of this chapter is to provide inspiration for future work to other researchers, particularly future Genzer group members. There is significant room to expand our work in on-demand surface chemistries for coatings microstructures as well as our simulation methods and algorithms.

6.1.1 Asymmetrical Particle Simulations

In Chapters 2-4, we relied on spherical particles in our simulations setups. This assumption was quite useful and arguably, accurate considering that many marine fouling organisms have approximately spherical shapes. However, many other marine fouling microorganisms are asymmetrical, either in shape of their “core” or distribution of their adhesive “hair” or flagella. To model adsorption of the latter class of organisms, the initial setup of the model needs to be modified. For asymmetrical distribution of adhesive flagella or “hair”, the surface grafting points of the coarse-grained polymer chains should be localized to reflect that of the true organism. **Figure 6.1** displays one imagined asymmetrical particle that more closely reflects the adhesive flagella of an algal zoospore. For asymmetrical particle shapes, one needs to change the particle design to move away from spheres to model cones, cylinders or multi-component shapes. For both these areas active collaboration with biologists studying such marine microorganisms is needed to address how best to model their shapes and asymmetries. Additionally, the model would have to be improved to allow for free-rotation of the particle to address the new asymmetries exploring the substrates. Finally, multiple different shapes could be used simultaneously in distributions similar to work shown in Chapter 4.

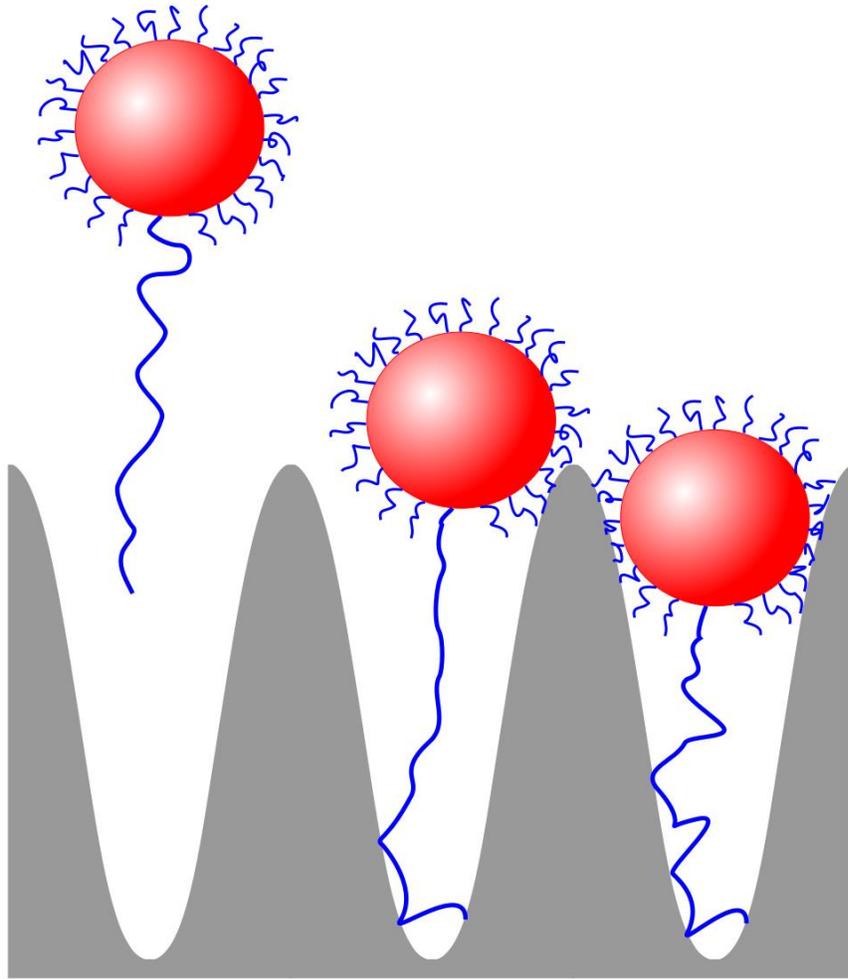


Figure 6.1. Concept of an algal zoospore, asymmetric particle to be used in the adhesion model. Depicted is the potential method of settlement and interaction with the substrate. This particle might use long flagella to sense the surface and drag itself in for settlement.

6.1.2 Optimization of Surface Topographies via Genetic Algorithm

Throughout our simulation work (Chapters 2-4) we utilized model surfaces comprising sinusoidal surface features. Utilization of substrates was inspired by previous work relating to surface topographies formed by modulus mismatched materials resulting in

surface wrinkling [1,2]. To further this progress and make our simulation more general, we considered a so-called genetic algorithm that would facilitate to move our model beyond pre-defined surfaces with fixed dimensions and shapes. A genetic algorithm allows for a combination of controlled and random mutation of a set of parameters built into a “genome” in conjunction with a “fitness” function. The “genome” is the set of parameters that define the candidate to be tested. The “fitness” function is the basis model used for comparison. The general flowchart for such an algorithm is provided in **Figure 6.2** applied to a system of sinusoidal waves in both x- and y-dimensions. For our purpose, the “genome” consists of parameters that define our substrate profiles and the “fitness” function is our previously developed adhesion model. For this simple case of bi-directional sinusoidal substrates, this is fully defined by four parameters, two amplitudes (A_x , A_y) and two wavelengths (λ_x , λ_y). As a demonstration of this technique, a genetic algorithm was implemented for the case of a bi-directional sinusoidal surface ($\sin(x)$ and $\sin(y)$). Convergence to a set of solutions was optimized quickly (*cf.* **Figure 6.3**). Within only a few generations of the simulations initiation, the adhesion energies of designed surface dropped by 75%. A major step forward would be to allow this algorithm to utilize a non-mathematical function to describe our surface profiles. To do this one could build a “genome” based on a spline method wherein a set of control points in 2D space can be used to define a surface profile. This spline method would then be introduced the genetic algorithm such that the computer could theoretically create entirely new and previously unknown surface profiles to reduce or inhibit the adsorption of a given particle or set of particles. We believe this would be a major

contribution to further this work and could lead to optimized and unique surface topographies.

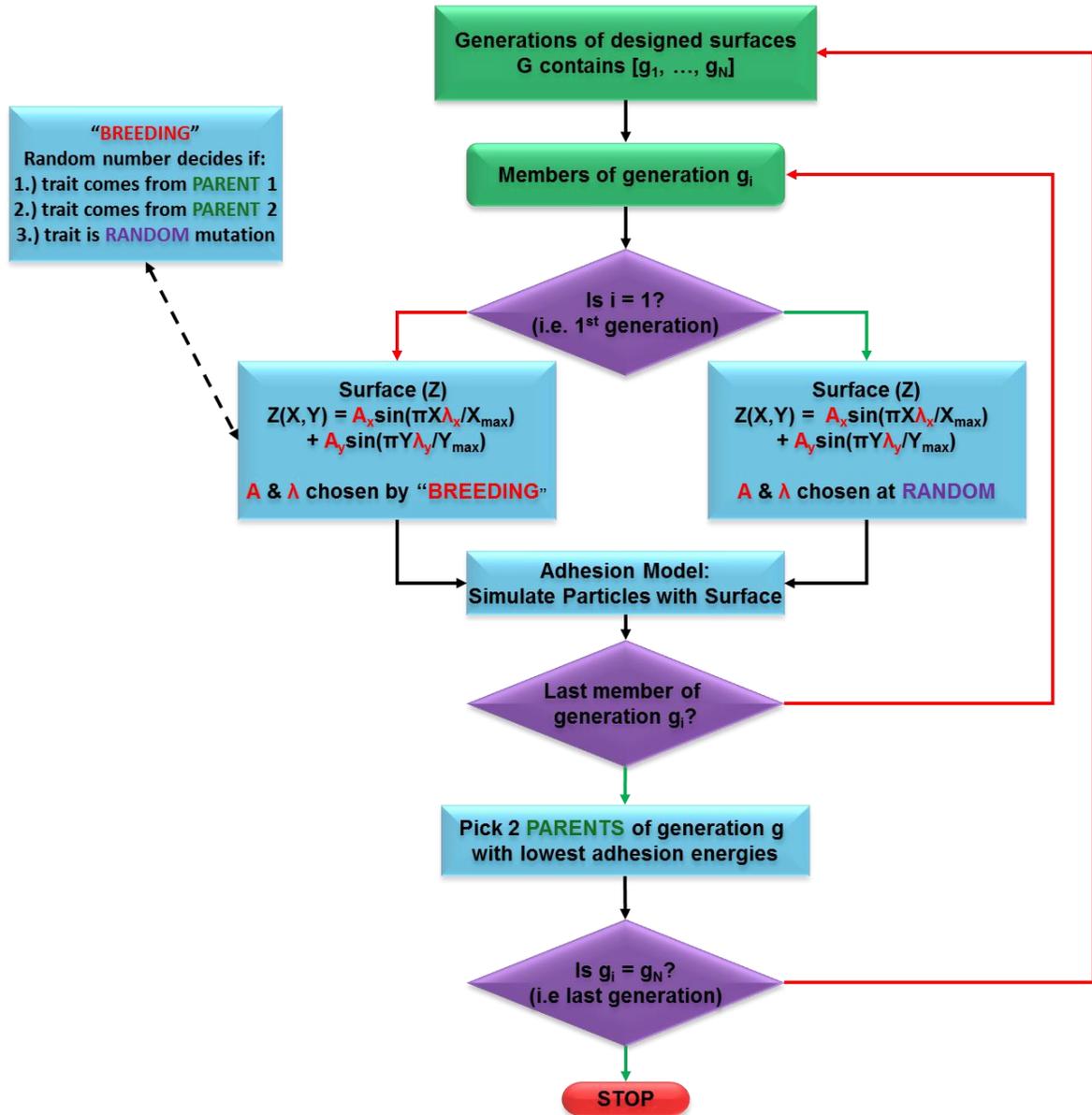


Figure 6.2. Schematic of genetic algorithm steps in optimizing a sinusoidal surface for minimal adhesion with a spherical particle of diameter ($D=20$). This algorithm undergoes several generations to reach convergence upon local or global minima.

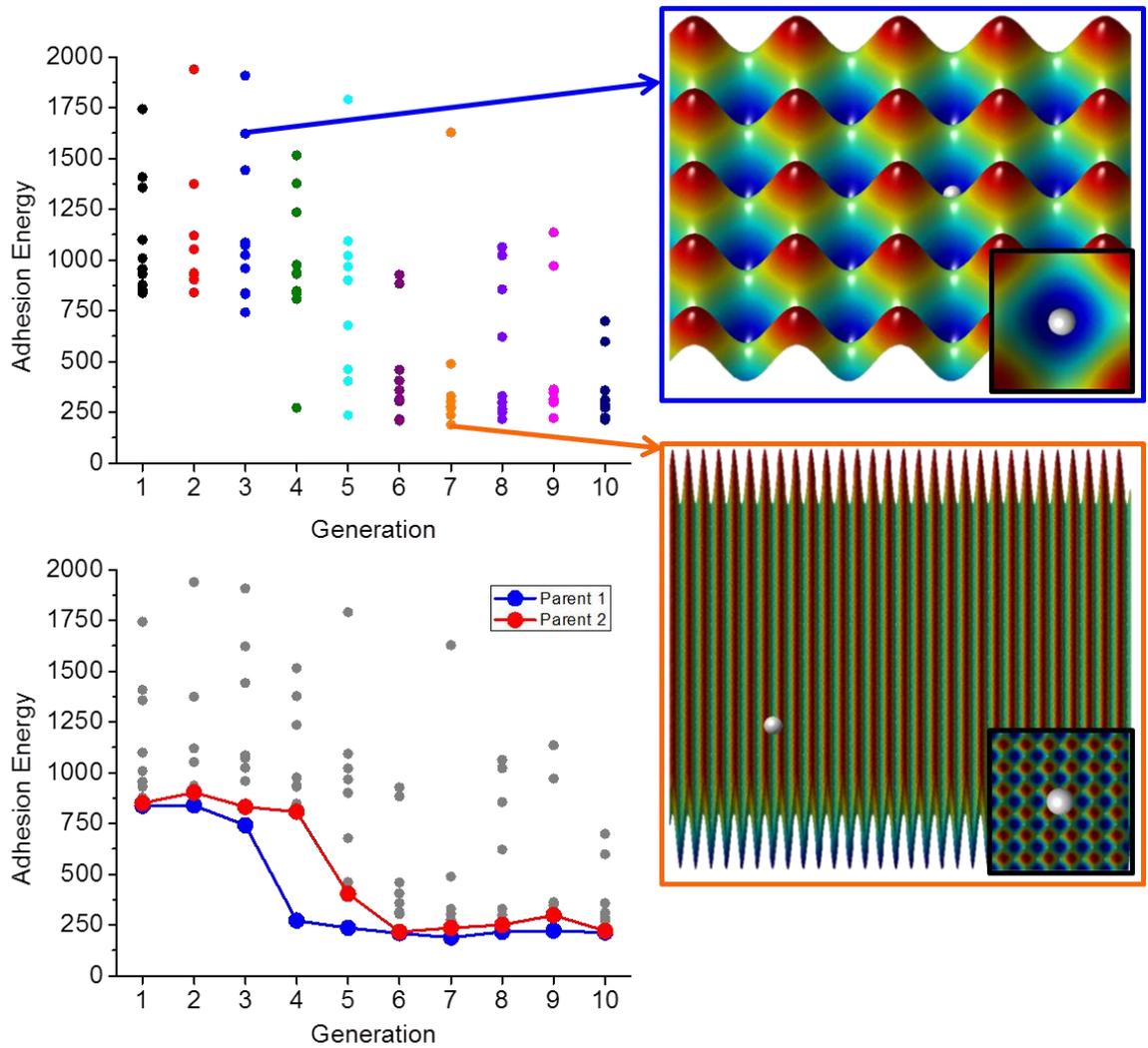


Figure 6.3. Genetic algorithm results from minimizing the adhesion energy of a diameter, $D=20$, particle on a bi-directional sinusoidal surface. (Top left) Shown is the distribution of adhesion energies for each generation of candidate surfaces. (Bottom left) Displays the highlighted minima of each generation of surfaces, showing how quickly the algorithm converges towards a set of desirable candidates. (Right) Angled (large) and overhead (small) views of the $D=20$ particle at its maximum energy location of high (blue) and low (orange) energy surfaces.

6.1.3 Optimization of Spraycoating Technology and On-Demand Surface Chemistries

Chapter 5 introduced novel modes of controlling the chemical make-up of our microstructures via a spraycoating method. This method is very useful due to its ability to conformally coat complex surface topographies. Another great benefit associated with this deposition method is that the ship-painting industry already utilizes a similar process in coating ship hulls. Our process creates a bilayer of polymer network gels. By first spraying a layer of polystyrene and cross-linking it, we establish a stable undercoat, which serves as a primer for attaching low-fouling/foul-release cross-linked functional layers. In our work, a betainized polymer (betainized poly(4-vinyl pyridine)) worked well to reduce settlement of barnacle cyprids and release a large percentage of cyprids that manage to adsorb. Polystyrene and polyvinyl pyridine were chosen specifically for their backbone cross-linking under UV light as well as the possibility to modify their chemistry into polyelectrolytes. Parameters such as spraycoat thickness, spraycoat solvent and cross-link density of the final network are left as open areas of future research.

6.2 References

1. Efimenko, K.; Rackaitis, M.; Manias, E.; Vaziri, A.; Mahadevan, L.; Genzer, J. Nested self-similar wrinkling patterns in skins. *Nature Materials* **2005**, *4*, 293-297.
2. Efimenko, K.; Finlay, J.; Callow, M.E.; Callow, J.A.; Genzer, J. Development and testing of hierarchically wrinkled coatings for marine antifouling. *ACS Applied Materials & Interfaces* **2009**, *1*, 1031-1040.